UNIVERSIDADE DE SÃO PAULO

INSTITUTO DE QUÍMICA

Programa de Pós-Graduação em Química

JORGE DA SILVA SHINOHARA

Hyperspectral Dark Field and Confocal Raman Microscopy Studies in Chemistry and Nanotechnology

Tese apresentada ao Instituto de Química

da Universidade de São Paulo para obtenção do

Título de Doutor em Química

VERSÃO CORRIGIDA

DATA DE DEPÓSITO : 15 DE FEVEREIRO DE 2023

Orientador: Prof. Dr. Henrique Eisi Toma

São Paulo

2023

"Estudos de hipermicroscopia de campo escuro e raman confocal em química e nanotecnologia"

JORGE DA SILVA SHINOHARA

Tese de Doutorado submetida ao Instituto de Química da Universidade de São Paulo como parte dos requisitos necessários à obtenção do grau de Doutor em Ciências - no Programa de Química.

_____
Prof. Dr. Henrique Eisi Toma
(Orientador e Presidente)

APROVADO(A) POR:

_____
Prof. Dr. Antonio Domingues dos Santos
IF - USP

_____
Prof. Dr. Vitor de Moraes Zamarion
Escola Beit Yaacov

_____
Dr. Kalil Cristhian Figueiredo Toledo
IQ - USP

SÃO PAULO
14 de abril de 2023

UNIVERSIDADE DE SÃO PAULO

INSTITUTO DE QUÍMICA

Programa de Pós-Graduação em Química

JORGE DA SILVA SHINOHARA

Hyperspectral Dark Field and Confocal Raman Microscopy Studies in Chemistry and Nanotechnology

Tese apresentada ao Instituto de Química

da Universidade de São Paulo para obtenção do

Título de Doutor em Química

Orientador: Prof. Dr. Henrique Eisi Toma

São Paulo

2023

AGRADECIMENTOS

A gratidão é a memória do coração (Antístenes, 365aC). Agradecer sempre é necessário, pois nada na vida se faz sozinho. Poucos serão os agradecimentos nominais, mas sejam todos agradecidos por mim em nome dos que eu citarei. Guardo todos vocês em meu coração.

Nessa caminhada pelo mundo acadêmico tenho muito a agradecer ao professor Henrique Toma pois sempre acreditou em mim, me passava suas ideias sempre de forma entusiástica e sempre esperou que eu conseguisse elucidar a situação. Me deu sua pesquisa de Livre Docência para repaginar com as técnicas modernas e uma linha de pesquisa que foi proeminente no grupo, a plasmônica de AuNP. Por toda confiança nas mais diversas tarefas e para a conclusão dessa etapa de doutorado sou imensamente grato.

Àqueles que me introduziram ao laboratório de pesquisa e foram meus primeiros tutores Dr. Vitor Zamarion e Dr. Daniel Grasseschi, por me mostrarem o caminho da pesquisa e do ensino. Ao super técnico Dr. Alceu Totti Silveira Jr., gente boa que sabe de tudo e sempre ajuda a todos.

Aos colegas do LQSN que convivi por um grande tempo, por todo conhecimento compartilhado no laboratório e na sala de café. Em especial os microscopistas Dr. Manoel Huila e Dr. Marcelo Nakamura. Também praqueles que pude trabalhar diretamente e de todos meus contemporâneos pelas infinitas trocas de conhecimento. Abraço especial para os doutores Julio, Fernando, Roberta, Ana Paula, Maria Luiza e Maria Rosana.

Meu aluno de IC Luis Gustavo e a todos os alunos aos quais fui monitor, de Química de Coordenação e da Geologia, pela experiência de ensino.

Ao Instituto de Química da USP que me acolheu em 2007 como aluno de graduação, teve toda compreensão com meu desenvolvimento acadêmico na graduação e na pós graduação. Meu abraço a todos os professores que tive nessa jornada, além dos meus colegas de várias gerações que convivi.

Às agências de fomento, CNPQ, CAPES e USP com o programa PAE pelas bolsas concedidas.

Meus pais e família que sempre souberam que sou um curioso. Minha esposa Elizia e minha filha Helena, por estarem ao meu lado nessa última parte da trajetória.

Enfim, a todos que passaram pelo meu caminho até agora, nas mais diversas atividades que tive, e ajudaram a me construir como pessoa.

Dedico essa tese ao meu pai, Masaki Shinohara.

A sprit with a vision
Is a dream with a mission
(Mission, Rush 1987)

ÍNDICE

ABSTRACT

Hyperspectral Dark Field and Confocal Raman Microscopy Studies in Chemistry and Nanotechnology

Jorge da Silva Shinohara

Hyperspectral imaging can provide accurate information on the distribution of the chemical species in materials and biological samples, based on the analysis of their electronic and vibrational profiles. In special, confocal Raman microscopy is one of the best ways to access the chemical distribution of molecules, especially under resonance Raman or SERS conditions. On the other hand, enhanced dark field optical microscopy can be employed for hyperspectral imaging in the visible and near-IR region, while extending the optical resolution up to the nanoscale dimension. It allows the detection of gold or silver single nanoparticles, as well as spectral monitoring from the characteristic surface plasmon bands. The two hyperspectral microscopies can be conveniently combined to provide nanoscale electronic and vibrational information of the species present in a wide variety of chemical and biological systems. Case studies, including the classical spot-test analysis of nickel(II) ions with dithizone are here reported. A great enhancement of sensitivity in the detection of nickel(II) ions, by at least 4 orders of magnitude, has been observed in this work. Hyperspectral measurements allowed the mapping of the gold nanoparticles (AuNP) distribution on cellulose fibers and on glass, and the evaluation of their extinction and SERS spectra for analytical purposes. Spot tests analysis metal ions with pentacyanidoferrate(II) complexes have also been examined from the point of view of electronic and Raman spectral images. Differentiation of the chemical and electromagnetic mechanisms in the SERS spectra of substituted terpyridine iron(II) complexes with gold nanoparticles has been reported. Characterization of Turkevich nanodisks, and ranelate induced gold nanoparticles formation have also been conducted in this thesis. Finally, hyperspectral techniques have been successfully employed to probe the interaction of gold nanoparticles with microtubules associated with molecular machines.

Keywords: Darkfield Microscopy, Confocal Raman, SERS, Plasmonic Nanoparticles, Raman spectroscopy, Spot Tests, Pentacyanidoferrates

RESUMO

Estudos de hipermicroscopia de campo escuro e Raman confocal em Química e Nanotecnologia.

Jorge da Silva Shinohara

A imagem hiperespectral pode fornecer informações precisas sobre a distribuição das espécies químicas em materiais e amostras biológicas, mediante a análise de seus perfis eletrônicos e vibracionais. Em particular, a microscopia confocal Raman é uma das melhores formas de acessar a distribuição químicos das moléculas, especialmente sob condições de ressonância Raman ou SERS. Por outro lado, a microscopia óptica de campo escuro pode ser empregada para obter imagens hiperespectrais na região do visível e infravermelho próximo, estendendo a resolução óptica até a nanoescala. Ele tem permitido a detecção de nanopartículas unitárias de ouro ou prata, bem como o monitoramento espectral das bandas dos plásmon de superfície. As duas microscopias hiperespectrais podem ser convenientemente combinadas para fornecer informações eletrônicas e vibracionais em nanoescala das espécies presentes em uma ampla variedade de sistemas químicos e biológicos. Estudos de casos, incluindo a clássica análise via spot-test de íons de níquel (II) com ditizona são relatados nesta tese. Um grande aumento da sensibilidade na detecção de íons níquel(II), em pelo menos 4 ordens de grandeza, foi observado. Medidas hiperespectrais permitiram o mapeamento da distribuição de nanopartículas de ouro (AuNP) em fibras de celulose e em vidro, e a avaliação de seus espectros de extinção e SERS para fins analíticos. Testes pontuais de análise de íons metálicos com complexos de pentacianidoferrato(II) também foram examinados do ponto de vista de imagens eletrônicas e espectrais Raman. Foi relatada a diferenciação dos mecanismos químicos e eletromagnéticos, nos espectros SERS de complexos de terpiridina ferro(II) substituídos com nanopartículas de ouro. A caracterização de nanodiscos de Turkevich e a formação de nanopartículas de ouro, induzidas por ranelato, também foram conduzidas nesta tese. Finalmente, técnicas hiperespectrais foram empregadas com sucesso para sondar a interação de nanopartículas de ouro com microtúbulos associados a máquinas moleculares.

Palavras Chave: Microscopia Hyperspectral, Raman Confocal, SERS, Nanopartículas Plasmônicas, Espectroscopia Raman, Spot Tests, Pentacianidoferratos.

1. INTRODUCTION

Hyperspectral microscopy is a modern way of exploring the imaging of materials and biological samples, conveying relevant spectral information from the molecules and nanoparticle constituents. By accessing the electronic or vibrational features embedded in every pixel of the image, important analytical data can be obtained at the micro and nanoscale.

While human eyes perceive the image colors by processing the visible light according to the three bands encompassing red, green and blue regions, in hyperspectral imaging, every pixel comprises the molecular spectrum, allowing to achieve a fine resolution while covering a wide range of wavelengths. Thanks to the computational facilities, the images can be reproduced from the spectra stored in every pixel, allowing to explore any particular spectroscopic feature (e.g. electronic or vibrational signals).

This thesis is focused on two types of hyperspectral microscopies, namely dark field microscopy (Cytoviva), and confocal Raman microscopy (WITec), illustrated by my contribution in scientific articles

Dark-field microscopy employs a peculiar optical arrangement which extends the limit of resolution beyond the classical Abbes' law (~$\lambda/2$), up to $\lambda/5$, thanks to the higher resolution power from the oblique illumination coupled with a cardoid annular condenser [1,2]. This technique is particularly rewarding in the case of plasmonic nanoparticles, such as gold and silver, because in addition to a higher resolution, the enhanced light scattering induced by the plasmon resonance, propagates in the space as a cone of radiation. This leads to a greater image magnification, allowing to discriminate individual nanoparticles [3–5] which are inaccessible to the conventional optical microcopes (Abbes´s law). In addition, by using a coupled spectral detector, one can record the single nanoparticles scattering spectra, allowing to generating the corresponding hyperspectral images from the collected data.

Confocal Raman microscopy associates a high-resolution setup with the Raman technique, to collect the spectroscopic information from every single spot. In this way, one can probe the molecular characteristics of the samples, by extracting the information from the vibrational data composing every pixel of the image. In addition, the Raman signals of plasmonic nanoparticles such as gold, are dramatically enhanced, exceeding 12 orders of magnitude, due to the so-called SERS effect (surface enhanced Raman scattering). In this way, the presence of plasmonic nanoparticles can be

explored for analytical purposes, in association with their strong Raman scattering, providing a great increase in sensitivity, for investigating chemical and biological samples.

Combination of dark-field and confocal Raman microscopy enables the investigation of plasmonic excitation and SERS effect in a variety of systems, particularly those containing nanoparticles as optical and spectral probes. Typical examples encompass the elucidation of the spectral characteristics of isolated and aggregated gold nanoparticles [3], the microscopy analysis of classical "spot-tests" in chemistry and forensics [6], the chemical imaging of shells [7] and the phagocytosis of gold nanoparticles by neutrophyl cells [8].

2.   OBJECTIVES

In this thesis, the hyperspectral strategy has been focused as an approach for improving the investigation of coordination compounds and nanoparticles, comprising six selected systems described as published papers, in the second part of this thesis. In addition, a brief introduction of the hyperspectral techniques, including plasmonics and Raman spectroscopy, is here supplied.

The first study, which inspired this thesis, was entitled "Confocal Raman microscopy and hyperspectral dark field microscopy imaging in chemical and biological systems". It was presented in the 2015-Meeting of the International Society for Optics and Photonics (SPIE) in San Francisco, and published as invited paper in the SPIE Journal [9]. The studied system involved the spot test analysis with the dithizone reagent for metal ions, and was carried out on a filter paper and on a silanized glass, exploring the SERS effect of dithizone in the presence of gold nanoparticles.

It should me mentioned that the classical spot test consists in impregnating a filter paper with the organic reagent, and observing the color changes after applying a drop of the metal ion solution. In this case, the detection is limited by the eyes sensitivity. The propose spot test analyses was greatly improved using Raman spectroscopy, exploring the enhanced signals from the chromophores in resonance with the exciting radiation. In addition, a further improvement was achieved by exploring the SERS effect associated with the gold nanoparticles [10–12].

The second work, published in 2019, focused on the title "Exploring the metallochromic behavior of pentacyanidoferrates in visual, electronic, and Raman spot tests" [13]. It was completely performed by this author, and the aim was to elucidate the electronic and vibrational spectra of pentacyanidoferrates involved in a series of spot test analysis for transition metal ions. The chemistry of pentacyanidoferrates has been a tradition in our Institute, since the foundation of the Laboratory by Professor Henry Taube in 1970. Therefore, improving the understanding of their chemistry is a relevant contribution pursued in this Thesis. Although the pentacyanidoferrates research encompasses many fundamental aspects, [14,15,24–27,16–23], here we are focusing on the spot tests analysis, as a new contribution to this theme. Such tests have been extensively employed for didactic purposes in the Coordination Chemistry course since 1984, but based on direct visual detection only. They were more accurately investigated in this thesis, using confocal Raman spectroscopy, aiming the elucidation of the dramatic color changes observed for the several metal ions.

In the next sequence of publications, our major contribution was concentrated on the acquisition and interpretation of the hyperspectral dark field and confocal Raman spectroscopy, as important aspects for understanding the reported systems.

The third work deals with the "Raman studies of bis(phenylterpyrazine)iron(II) and supramolecular species with pentacyanidoferrate(II) ions. It was published in the special number of Quimica Nova, dedicated to Professor Hans Stammreich, in 2019 [28]. The major goal was the elucidation of the resonance Raman effect involving several similar chromophore units, of very difficult discrimination using conventional vibrational spectroscopy.

The fourth work was concentrated in the Raman characterization of the gold nanodiscs as part of the investigation on the "Facile synthesis of labile nanodiscs by the Turkevich method" published in 2018 in the Journal of Nanoparticles Research [29] .

The fifth work was dedicated to the theme "Gold nanoparticle conjugation with microtubules for nanobiostructure formation" published in 2018 in Journal of Bionanoscience [30]. It represented a relevant contribution to the characterization of microtubules modified with gold nanoparticles, as part of the investigation of nanomolecular machines by the post-doctoral fellow Daniel de Oliveira, in our research group.

The sixth work encompasses the elucidation of the SERS spectra of the ranelate modified gold nanoparticles. It was reported in the paper "Room temperature synthesis and Raman spectral evidence of carbon bond ranelate-gold nanoparticles" published in 2020, in Journal of Raman Spectroscopy [31]. This contribution is part of a recent research line focusing on the chemistry of the ranelate ions in our laboratory.

3) DARK-FIELD HYPERSPECTRAL MICROSCOPY

Dark-Field Microscopy (DFM) is based on the collection of the scattered and diffracted light by the sample. To accomplish this, the light source, or the zeroth order diffraction, should not reach the objective, so that the sample appears as bright spots on a dark background. The simplest way to achieve this is by using an oblique illumination with an aperture angle higher than the objective aperture angle. Different setups of light source, condensers, and objective lens have been constructed to improve the signal-to-noise ratio, contrast and resolution, being reported by several authors in recent reviews [32–37]. The images are acquired by a CCD camera to produces RGB dark-field images or by a spectrometer to produces a hyperspectral images(HIS), where each pixel has a full spectral information.

Zsigmond, in 1926, was the first to employ a dark-field microscopy setup to study the properties of a colloid [38]. Since then, different dark-field microscope configurations have been reported using different light sources, condenser lens or objective lens. As the source it is commonly used a broadband light, but monochromatic sources, lasers or filtered light, are used in the fluorescence mode. There are several ways to do the light incidence in a dark-field mode, the simplest way is using an annular stopper between the light source and the condenser lens or using a conventional bright-field condenser with the iris almost closed [39]. With these condenser lens, the microscope is used in a transmittance mode and the light incidence is made under the sample. Efforts to improve the optical capacity of view reports down to 100 nm [40,41].

Another configuration for DFM is with the illumination above the specimen, in a scattering mode, this setup is considered a total internal reflection mode. There are two principal types, with high [42] and small [32] incidence angles. The advantage of this setup is the possibility to control the incident light polarization and to collect the intensity of scattered light in different polarization angles, enabling the analyses of anisotropic

nanoparticles, nanoparticles dynamics [43,44] and growth mechanism [45]. Also it has been reported three dimension DFM images, where non-polarized and polarized beam are split in perpendicular polarizations. The reconstructed images reproduces accurately the particles or microorganisms path through the substrate [46,47].

Recently a CytoViva ultra-resolution imaging system, composed by a dark-field hyperspectral arrangement mounted on a conventional microscope, have been used for recording the single particles Rayleigh scattering spectra. The CytoViva system uses an annular cardoid condenser [2] with high annular aperture that enables the collection of higher order diffracted light by the objective, increasing the resolution power up to the diffraction limit, reaching $\lambda/5$. Figure 1 shows an illustration of the experimental arrangement. Allied to the intensified light scattering by the plasmonic nanoparticles, this ultra-resolution optical system enables the study of a variety of nanoparticles, even in wet media.

With this configuration is possible to record a dark-field optical image composed by a three channel RGB spectra with a spatial resolution of 64 nm, and a Hyperspectral image where each pixel has 64 nm and carries a full visible spectra information. For a better spectral signal-to-noise ratio a binning process can be made, where every four pixel is summed and a new pixel of 128 nm with an average spectra is generated. However, due the enhanced light scattering of the plasmonic nanoparticles, the full resolution hyperspectral image can be achieved (Figure 2).
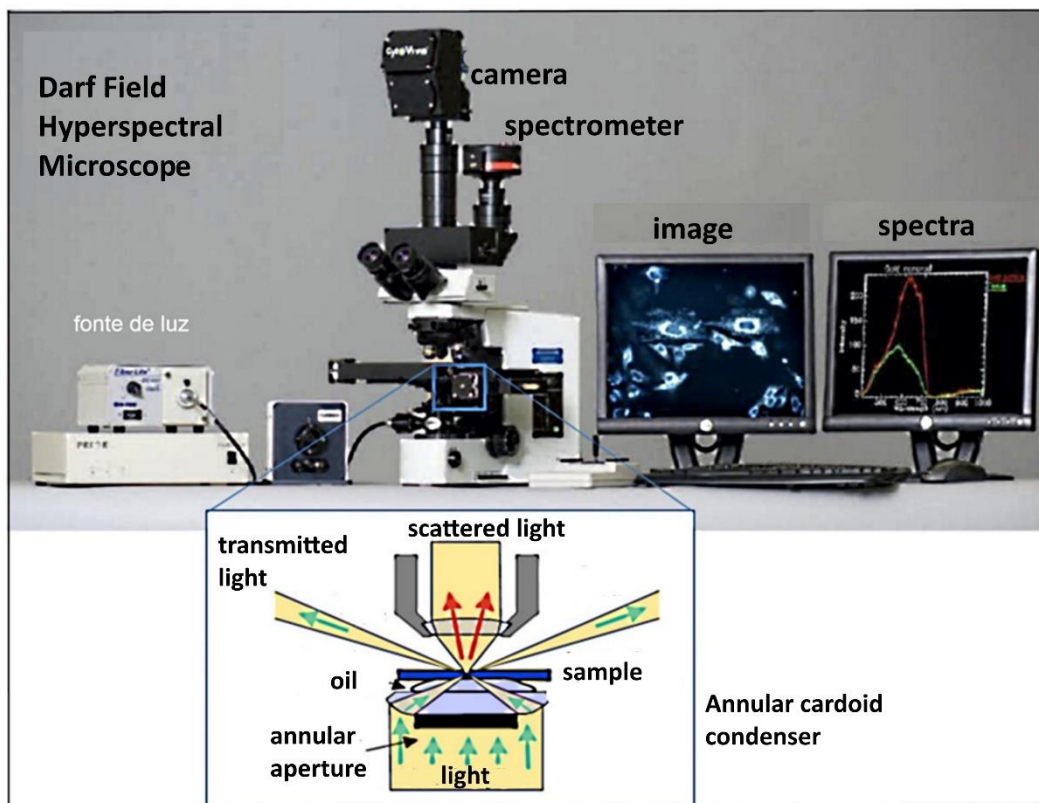
Figure 1. The Cytoviva dark field hypermicroscope and the annular cardoid condenser associated with the optical objectives.
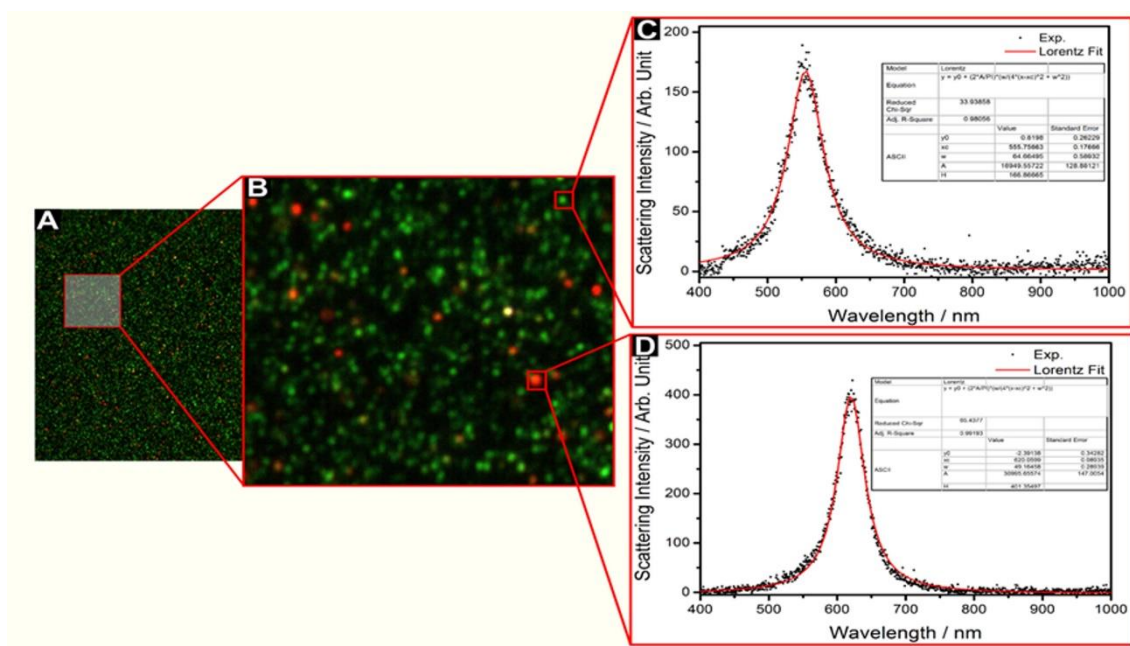

Figure 2. Cytoviva dark field microscopy images of gold nanoparticles and their scattering spectra at the individual level.

4) RAMAN SPECTROSCOPY AND CONFOCAL RAMAN MICROSCOPY

The interaction of electromagnetic radiation with matter is the essence of all optical phenomena, including refraction, diffraction, absorption, emission, scattering and also plasmonics.

When light strikes a molecule, the oscilatting electric field, $E(\omega)$, induces an electron displacement, generating an induced dipole moment µ (Figure 3)
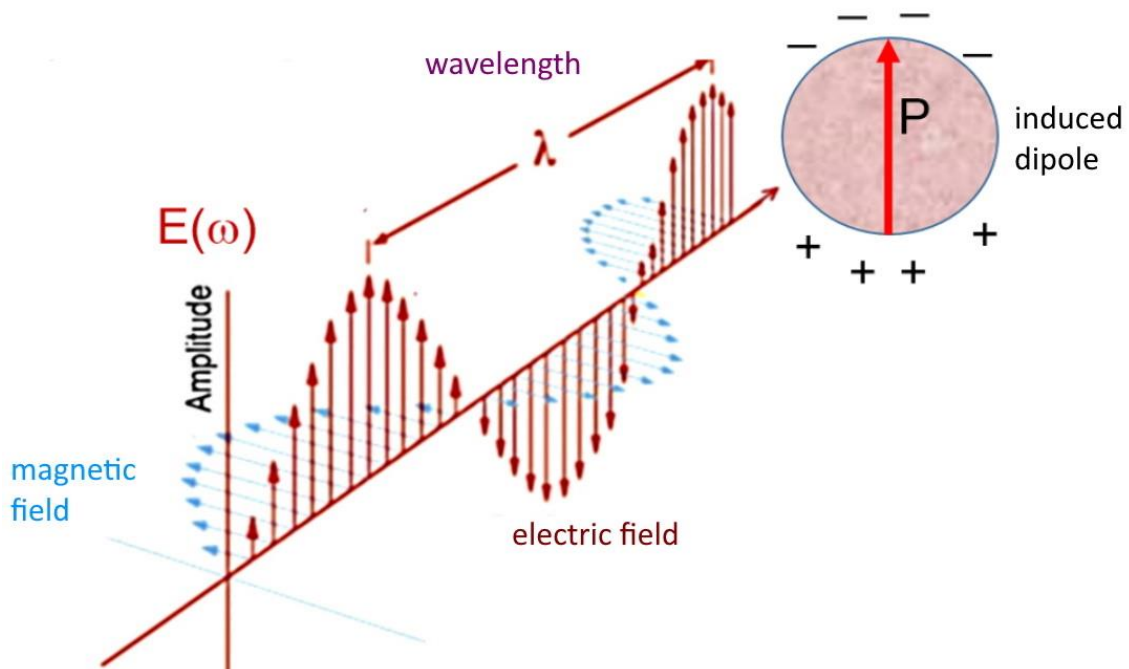

Figure 3. Interaction of the electromagnetic wave with matter.

In a didactic way, we can formalize it as:

For a local electron density, the dipole moment, µ, is given by

$\mu = \alpha.E(\omega)$ where α is the polarizability constant.

In the case of a molecule or particle, the description involves a global dipole moment P, where:

$P = \chi(\omega).E(\omega)$

and $\chi(\omega) = \Sigma\alpha$, represents the electric susceptibility of the species.

Inside the body, the total electric field (D) is given by the external $E(\omega)$, plus the field associated with the induced dipole moment, $4\pi P$.

Therefore, $D = E(\omega) + 4\pi.P$

or

$$D = (1 + 4\pi.\chi).E(\omega)$$

This means that the internal electric field encompasses the induced term, P, which reflects the electric susceptibility χ, which expresses how the internal electrons respond to $E(\omega)$. This leads to the dielectric constant κ (individual particle) or ε (global),

$$\varepsilon = \frac{D}{E(\omega)} = (1 + 4\pi\chi)$$

In this way, the dielectric constant is associated with the interaction of the electrons with light, and is also related with the refraction index η, which is the ratio of the speed of light in vacuum (c) and in the matter (v).

$$\eta = \frac{c}{v}$$

On the other hand, for optical applications, Maxwell has shown that

$$\varepsilon = \kappa = \eta^2$$

The refraction index reflects the differences in the speed of light through two different media, and is perceived by the deviation of the light beam crossing the interface.

When light is absorbed by the medium, it is necessary to consider the total refraction index, N, given by

$$N = \eta + i.k$$

where i is the imaginary part and k is the absorption coefficient, normally expressed by Beer´s Law, as

$$k = \frac{\lambda}{4\pi} \varepsilon_a c$$

where ε_a = absortivity, c = concentration.

Raman spectra

Light scattering involves the collision of fotons with the molecules, and depends on the intensity of the radiation (I_o), the fourth power of the frequency ν, and the square of the polarizabilty factors (α_{ij}) involved in all chemical bonds, as expressed by

$$I = (\frac{16\pi^2}{9c^4})I_o \nu^4 \Sigma_i \Sigma_j |(\alpha_{ij})|^2$$

The interaction of light with the electrons induces oscillating dipoles, which start irradiating the photons, promoting the scattering phenomenon. Therefore, scattering depends on the polarizability terms, which also express the distortion of the electron

clouds under the influence of the electromagnetic radiation. Most of the photons that hit a molecule suffer elastic collisions, being scattered in all directions, with the same energy. This type of scattering is known as Rayleigh scattering. However, a small portion undergoes inelastic scattering, incorporating or subtracting vibrational energies during the collision process. The photon collision is extremely fast, leading to a virtual state which can decays to the vibrational levels which are higher than the fundamental vibrational level, as illustrated in Figure 4. The scattered photon has its energy subtracted equal to the vibrational energy involved, and its analysis allows obtaining the vibrational spectrum of the molecule, known as the Raman spectrum , in honor of its discoverer, who received the Nobel Prize in 1930. This scattering mode is called Stokes. When the photon encounters the molecule already in the excited vibrational state, the scattering may incorporate this additional energy, leading to the Anti-Stokes scattering.
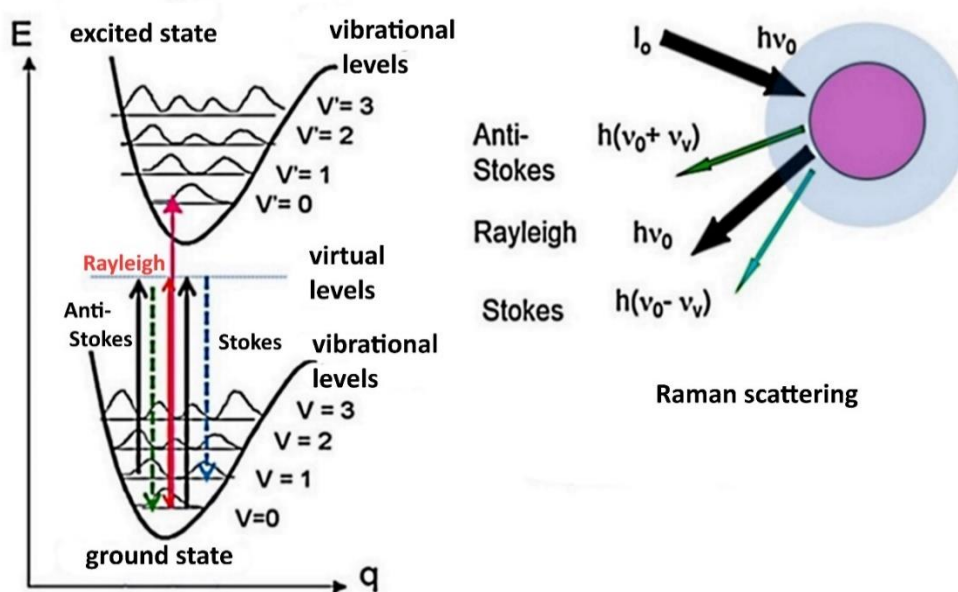

Figure 4. Potential curves and vibrational levels associated with the Raman scattering phenomenon, showing the Rayleigh, Stokes and Anti-Stokes modes.

The efficiency of Raman scattering is very small, and in the past, spectral recording required several days of collecting photons on a photographic paper. With the introduction of lasers in Raman spectroscopy, specially by Sergio Porto in Brazil, this modality became very practical, overcoming the limitations of the low signal intensity. It should be noted that the Raman spectral information is similar to that of vibrational spectroscopy (infrared), however it incorporates new selection rules that turn the spectra

distinct [48]. Therefore, the two spectroscopies are complementary. However, Raman spectroscopy allows monitoring samples in water, which is impractical in infrared spectroscopy.

In Figure 5 it is shown the energy diagrams composed by vibrational and electronic levels, and the excitation mechanisms associated with infrared, Raman, resonant Raman and fluorescence spectroscopy.
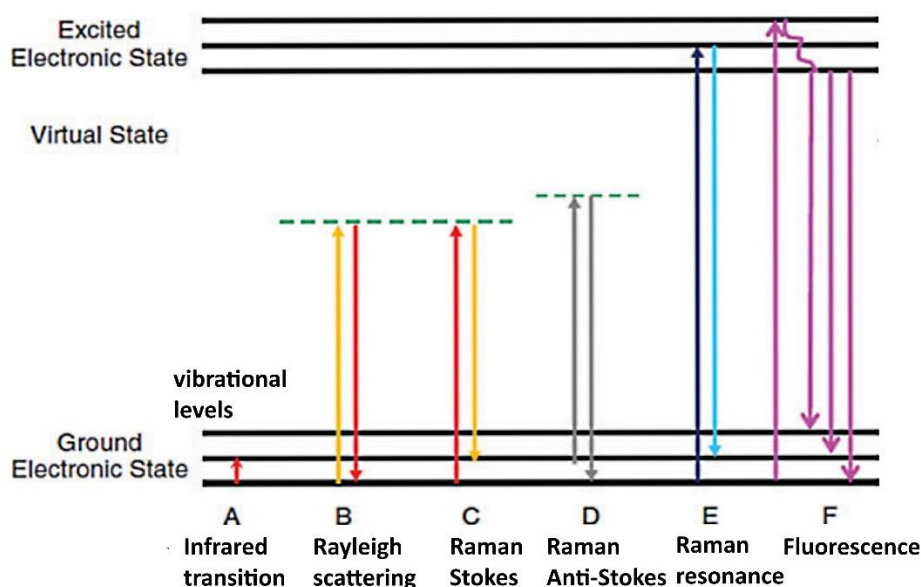

Figure 5. Energy diagrams for a (A) vibrational excitation, (B) Rayleigh scattering, (C) Raman Stokes scattering, (D) Raman anti-Stokes scattering, (E) Raman resonance and (F) fluorescence.

When the energy of the exciting light coincides with the electronic levels of the molecule (Figure 4E), the collisional cross section becomes larger, generating an enhancement of up to 5 orders of magnitude in the Raman signals. This effect is known as resonance Raman [49]. The great advantage of this effect is the possibility of selectively monitoring the characteristics of the chromophores, an important point in the study of biological systems. For example, in proteins that have the heme group (iron-porphyrin), the resonant Raman spectra selectively enhances the vibrations of the porphyrin ring, as this is the main chromophore group in the structure. It should be noted that the corresponding vibrational spectrum in the infrared is quite different from the Raman spectrum, as it does not selectively expose the porphyrin chromophore, and

becomes quite complex by encompassing vibrational contributions from all the groups present in the protein species.

In our laboratory, the normal Raman measurements has performed using portable equipments such as the Inphotote (from InPhotonics) spectrometer, operating at 785 nm (Figure 6). Its technical characteristics are summarized in Table 1. Nowadays, this instrument has been replaced by a similar, portable Wasatch equipment.
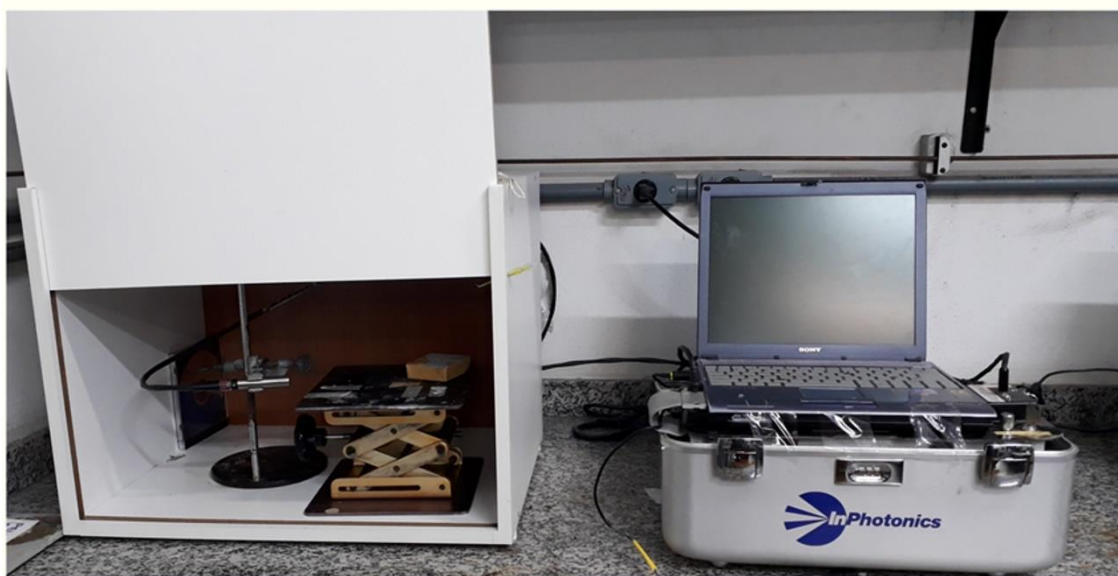

Figure 6. In Photote Raman spectrometer and fiber optics probe assembly.

Table 1. Technical characteristics of the In Photote portable Raman spectrometer.

Excitation source	diode laser, 300 mW, 785 nm.
Detector	CCD array, 1024 x 128 pixels, Peltier refrigeration at -25 ºC.
Fiber optics	excitation with 105 μm single fiber, collection with 200 μm single fiber, aligned and supplied with a filter and guide waves, N.A. 0.22.
Spectral range	$250 – 1800$ cm^{-1}
Spectral resolution	$4 – 5$ cm^{-1}
Rayleigh scattering filter	atennuation level of 10^8
Working distance	5 mm

The confocal Raman equipment employed was a WITec alpha 300 R, as illustrated in Figure 7. Its technical characteristics are summarized in Table 2.
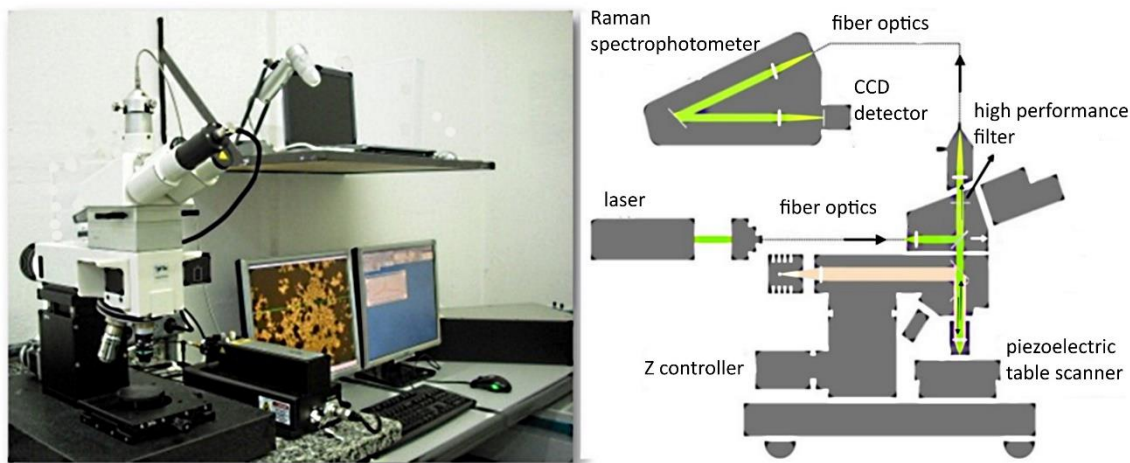
Figure 7. Confocal Raman spectrometer, and internal scheme, of the WITec model alpha 300 R model.

Table 2. Technical characteristics of the WITec confocal Alpha 300R spectrometer

Spectrometer UHTS 300: grating	500 nm, 600 lines/mm, and 1800 lines/mm
Detector	Newton EMCCD DU970 BV(Andor) 1600 x 200 pixels of 16 x 16 μm, working temperature -60 ℃, gain 1000 x
Lens	Nikon, 10X NA 0.25; 20X NA 0.40; 100X NA 0.80
White illumination	LED Köhler
Piezoelectric table	(z) ± 20 μm, (x,y) $\pm$ 180 μm
Lasers	488 nm [Ar] (Lasos77) ; 532 nm [solid state Nd:YAG] (WITec), 633 nm [He-Ne] (Research Electro-optics), TruePower polarized filter.
Software	Witec Suite 5

5) PLASMONICS AND NANOPARTICLES

Nanoparticles, well known from colloidal chemistry, have gained new perspectives with nanotechnology through advances that allowed reaching the individual level, i. e. of a single molecule. Besides the large surface area provided by the nanometric systems, their small size favors Brownian motion, imparting mobility to particles in the fluid environment. In addition, their performance can be dramatically improved by combining the nanometric properties with those of the chemical systems linked to the

surface, such as the complexing ligands. These composed species behave as functionalized nanoparticles, bearing molecular ligands anchored on the solid core, leading to a coating or shell which concentrates many accessible functional groups on the surface. Such groups can act in association with the nanoparticles core, providing a large surface distribution of reactive spots, which can act more effectively, as supramolecular structures, in comparison with the randomic distribution of the free ligands in solution.

In this way, the binding of suitable ligands to nanoparticles can be explored for metal ion complexation, allowing a variety of applications, such as:

a) analytical detection of elements;

b) removal of hazardous metals;

c) recovery and recycling precious or strategic elements;

d) drug transport and delivery;

e) affinity process of separation of chemical/biological species;

f) assembling associated nanoparticle structures.

Their particular use will depend on the nature of the nanoparticles, including the core and the ligand species, as well as their particular characteristics [50], such as magnetization and hard-soft acid-base (HSAB) properties, including sizes, zeta potentials and mobility.

However, in addition to their functionalities, it is necessary to work on the forces at the nanoparticles surface to prevent them from agglomerating and precipitating. This can be performed chemically by introducing suitable modifications for imparting electrostatic and steric effects, as expressed by the DLVO theory [51].

The stability of colloidal systems requires a balance of attractive van der Waals forces and repulsive Coulombic forces between the nanoparticles. A typical case are the particles coated with citrate ligands, where the negatively charged species repel each other and prevent the formation of aggregates (Figure 8).
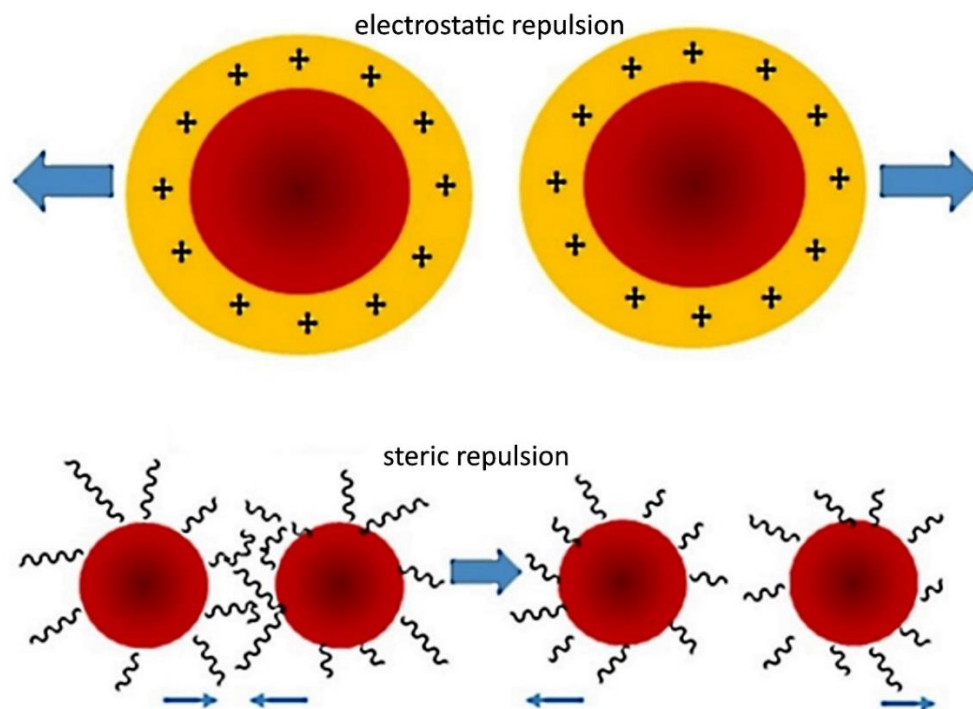
Figure 8. Electrostatic and steric repulsion promoting the stability of nanoparticles in solution (DLVO Theory). Adapted from reference [52].

In the case of nanoparticles coated with surfactants and polymers, the chains exposed to the solvent exert a kind of steric block around the metallic nuclei, filling the necessary space for the approximation and interaction between them. Thus, through steric effects, they exert repulsive forces that prevent a stronger interaction between nanoparticles, precluding the formation of aggregates.

The stability of the nanoparticles is of fundamental importance when considering their applications, such as in pharmaceutical formulations. The colloidal solutions must remain stable during their shelf life, which can be of several years. One way to probe the stability is measuring the zeta potential of the suspensions. In simple terms, an electrically charged particle has a certain surface potential, as illustrated in Figure 9 [52]. In solution, this charge is immediately counterbalanced by the adsorption of oppositely charged ions, forming an ionic layer strongly bound to the particle (Stern layer), which moves along with the particle. This movement is accompanied by the sliding of another weakly bound ionic layer, with which it is in contact, generating a kind of shear plane. The charge in this layer, known as the Zeta potential, can be measured by an electrophoretic effect that makes the particle move towards the pole of the electrode with

opposite charge. In principle, the greater the Zeta potential, the greater the electrostatic repulsion between the particles, and therefore the more stable the emulsion [52].
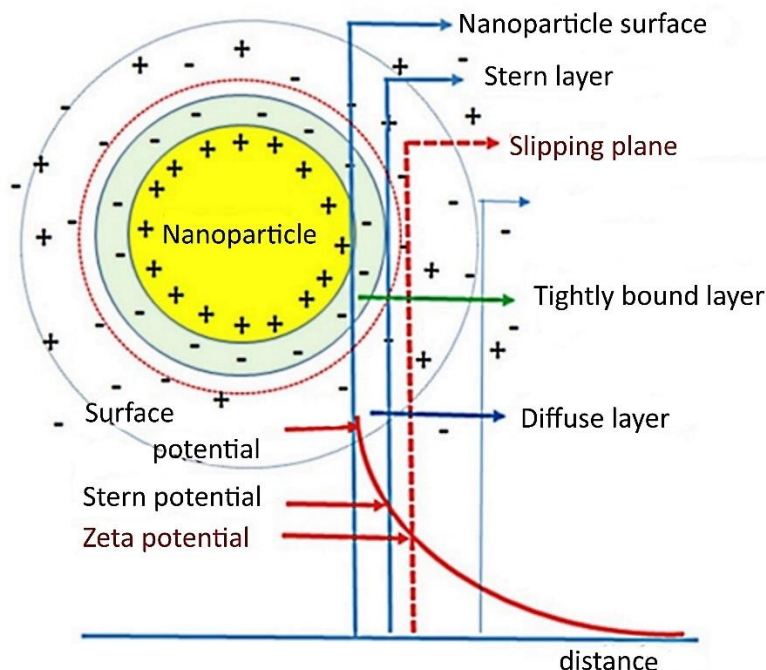

Figure 9. Charge distribution around a nanoparticle in solution, showing the central core and surface potential, followed by the ionic Stern layer encompassing a tightly bound shell, and by the slipping plane with the Zeta potential, in contact with the diffuse layer (Adapted from reference [52]).

To control the stability, it is common to explore the effects of pH, the coordination of metallic complexes, or using cationic or anionic surfactants that, in addition to acting through steric effects, also help to maintain the repulsive electric charge of the particles, avoiding the crowd.

Plasmonic nanoparticles

The nanometric dimension offers a new perspective regarding the interaction of nanoparticles with light. When light strikes the nanoparticles, the typical phenomenon observed is diffuse scattering, which gives rise to the Tyndall effect. This effect is very useful for visualizing the propagation of a light beam through a colloidal solution. However, for some nanoparticles, light scattering occurs anomalously, stimulated by the electromagnetic interactions at the surface level. Metallic elements, such as gold (Au), silver (Ag) and copper (Cu), exhibit only one electron in the outer shell configuration,

being very accessible energetically. In this way, the visible light excitation imparts a typical color and shine to the metals. But, when the metallic particles are much smaller than the wavelength of the incident light, the electrons couple with the oscillating electromagnetic field, generating a kind of wave, called plasmon. This coupling is responsible for the appearance of new colors in the nanoparticles, quite different from the colors of the metals. For example, gold nanoparticles in solution have a typical reddish hue, without the characteristic golden luster of metallic gold. When they aggregate, they change color, tending towards blue. These plasmonic manifestations are very important, allowing many applications in nanotechnology.

The most common plasmonic nanoparticles are gold, silver and copper. Although copper also exhibits plasmonic behavior, its greater chemical reactivity, specially the ease of oxidation, and has a narrow range of working frequencies, makes it more problematic for a general use. Even silver nanoparticles, despite being widely used, also suffer from this limitation. Thus, most applications are centered on gold nanoparticles, as they offer greater stability and allow working in ambient conditions, both in aqueous and hydrophobic environments. In contrast with copper, silver and gold, in the case of platinum, the plasmon resonance is strongly damped by the localized d-electrons near the Fermi level [53].

The synthesis of gold nanoparticles was first performed by Michael Faraday [54] in 1847 and reinvented by BRUST et al. [55], being more suitable for working in organic or hydrophobic environments. According to this method, the $H[AuCl_4]$ compound is dissolved in water and transferred to an organic phase, such as toluene, with the aid of tetraoctylammonium bromide. The addition of an aqueous solution of sodium borohydride, $Na[BH_4]$ followed by the introduction of an organothiol, such as dodecanethiol, and subsequent stirring of the biphasic system, leads to the formation of gold nanoparticles, which is perceptible by the reddish hue of the organic phase. Particle size can be controlled by the amount of the organothiol agent, which binds to the surface of gold nanoparticles and promotes their stabilization in solution. Thus, the amount of organothiol used influences the size of the nanoparticles, and can be used as a form of control, in addition to the temperature. The nanoparticles obtained by the Brust method can be isolated in solid state, and easily redispersed in organic solvents.

Another widely used method, mainly for working in aqueous media, is the one developed by Turkevich et al. [56,57]. The method is based on the reduction of gold salts

or H[AuCl₄] with citric acid, in aqueous medium, forming nanoparticles stabilized with citrate, or cit-AuNP. This procedure yields nanoparticles in the range of 15 to 50 nm, whereas in the Brust method [55], particles with smaller size variation are obtained, in addition of being very small (< 10 nm). For many applications larger particles can be more interesting, as they allow the exploration of plasmonic effects through Raman spectroscopy.

Despite being older than the Brust method, the mechanisms involved in the Turkevich method are still being investigated. The process, which is easier to perform, spans a variety of colors, from blue to red, during the reaction. Its reproducibility depends on many factors, such as stirring speed, reagent addition mode, citric acid concentration and temperature.

The reaction involved can be expressed as

$$[AuCl_4]^- + C(OH)(CH_2)_2(CO_2H)_3 \rightarrow Au^0 + O{=}C(CH_2)_2(CO_2H)_2 + CO_2 + 2H^+ + 4Cl^-$$
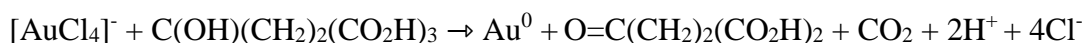
The primary product of citric acid oxidation by Au(III) ions is a dicarboxyketone which is unstable at the high temperatures employed in the process. That's why it decomposes before it can be observed [58]. However, in the absence of excess citric acid, dicarboxyketone was found to remain bound to the gold nanoparticles, presumably at the central C atom of the molecule [58]. This observation agrees with the soft base character of the carbon ligand and the gold atoms. Depending on the procedure used, this species can even remain in solution, altering the growth process of the gold nanoparticles, to generate variable sizes and geometries. In the presence of excess citric acid, at high temperatures, the dicarboxyketone ligand is displaced, leading to its decomposition. Under these conditions, citrate becomes the dominant species in the surface of gold nanoparticles, coordinated by the carboxylate groups. Because of the hard base character the citric acid and the soft nature of the gold atoms, this unmatched combination imparts a labile character to the weakly bound citrate ligands.

Plasmonic resonance and electromagnetic interactions

In the case of nanoparticles and nanosurfaces, the electromagnetic radiation and induce oscillations in the loosely bond electrons, starts to behave as localized or non

localized plasmons waves. In this way, the electron oscillation generates an induced plamonic dipole, p, given by

$$p = \varepsilon \, \alpha \, E_o$$

where

$$\alpha = 4\pi\varepsilon_o R^3 \, \frac{(\varepsilon - \varepsilon_m)}{(\varepsilon + 2\varepsilon_m)}$$

where R is the radius of the particle, ε_o is the dielectric constant of the vacuum, ε_m is the dielectric constant of the medium, and ε, the dielectric constant of the metal. In the case of light, the oscillating electric field can excite plasmons as a function of the radiation frequency (ω), (Figure 10).
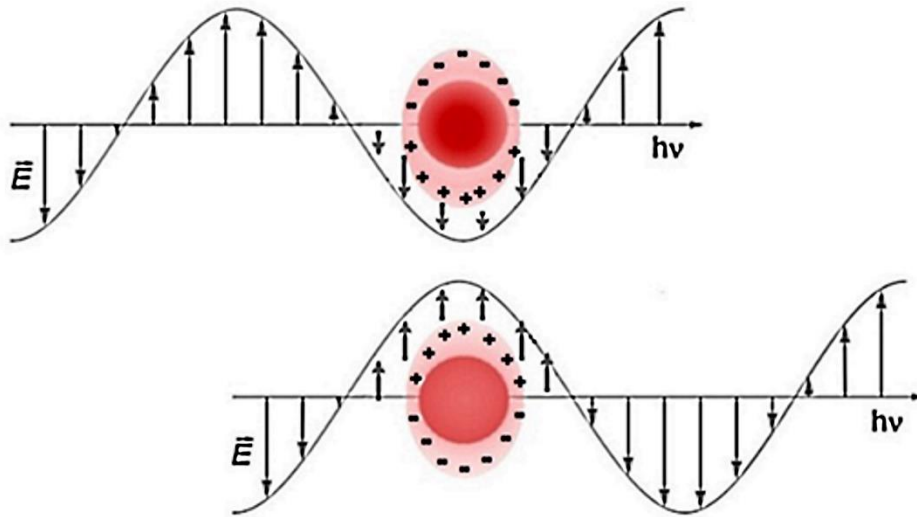

Figure 10. Oscillating dipoles propagating as plasmons in resonance with the electromagnetic radiation.

The dielectric constant of the metal is also a function of the frequency ω, and is composed of a real part, ε_1, and an imaginary part, $i.\varepsilon_2$

$$\varepsilon = \varepsilon_1 \, (\omega) + i\varepsilon_2(\omega)$$

Excitation of plasmons by light can be followed by dissipation of energy by radiative decay (scattering) or non-radiative decay (absorption). This can be measured by

the absorbance of the solution, A, as a function of the optical path (d), the concentration (N), and the extinction coefficient (σ_{ext}) which incorporates both scattering and absorption of light.

$$A = \frac{N\,\sigma_{ext}\,d}{2.303}$$

The extinction coefficient expresses the efficiency with which nanoparticles scatter or absorb incident light, and this is related to the response of electrons or plasmons in relation to the oscillating electric field, or their dielectric constants, ε. Accordingly, light scattering in plasmonic nanoparticles was first equated by Mie [59], in 1908, as

$$\sigma_{ext} = 9\left(\frac{\omega}{c}\right)\varepsilon_m^{3/2}\,V\left(\frac{\varepsilon_2(\omega)}{[\varepsilon_1(\omega) + 2\varepsilon_m]^2 + [\varepsilon_2(\omega)]^2}\right)$$

where V = corresponds to the average volume of the nanoparticle, given by $(4/3)\pi r^3$.

The intensity of interaction of radiation with plasmons is related to the oscillating dipole (p), which in turn depends on the polarizability constant α. The denominator of this equation, $(\varepsilon_1 + 2\varepsilon_m)$, tends to zero when $\varepsilon_1 = -2\varepsilon_m$, leading to a maximum value of α, and also of the intensity of interaction with light. This equality establishes the resonance condition, initially predicted by Mie.

Therefore, in the same way as observed in the refraction and absorption phenomena, light scattering is also governed by the dielectric functions of the material (ε) and medium (ε_m). It can be seen that light absorption and scattering are given by the cross section (σ) equations:

$$\sigma_{abs} = \frac{8\pi^2}{\lambda}r^3\mathrm{Im}\left[\frac{\varepsilon-\varepsilon_m}{\varepsilon+2\varepsilon_m}\right]$$

$$\sigma_{sca} = \frac{64\pi^5}{3\lambda^4}r^6\left|\frac{\varepsilon-\varepsilon_m}{\varepsilon+2\varepsilon_m}\right|^2$$

Thus, both light scattering and absorption present a maximum when at a given frequency ω, ε equals $-2\varepsilon_m$, as can be seen in the extinction spectrum of Figure 11.
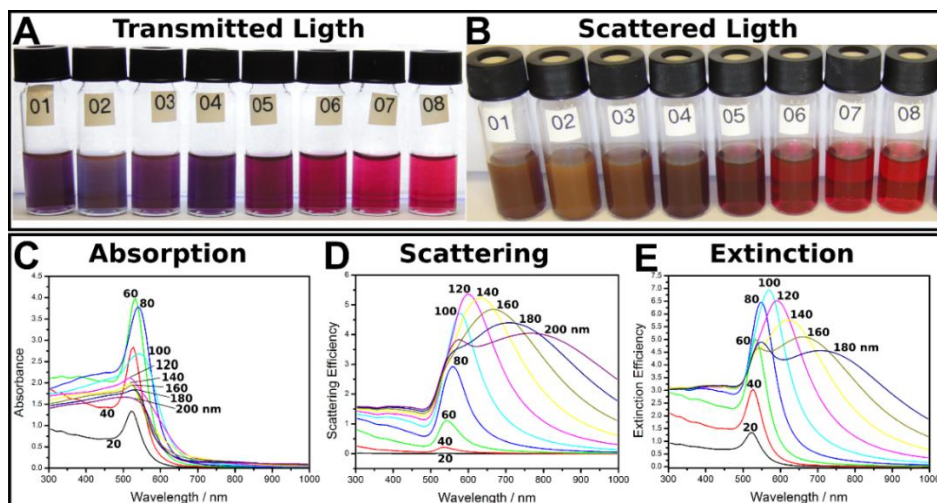
Figure 11. Transmitted (A) and scattered (B) light view of gold nanoparticles (20-200 nm), showing the corresponding absorption (C), scattering (D) and extinction (E) spectra.

The oscillation of surface plasmons depends on the shape and size of the nanoparticles. Spherical particles up to 100 nm have dipolar resonances, with a single band, which typically shifts from 500 to 600 nm with increasing size, acquiring a color that varies from red-orange to red-violet. Larger particles may have quadrupoles that give rise to another extinction band at higher wavelengths (Figure 12).
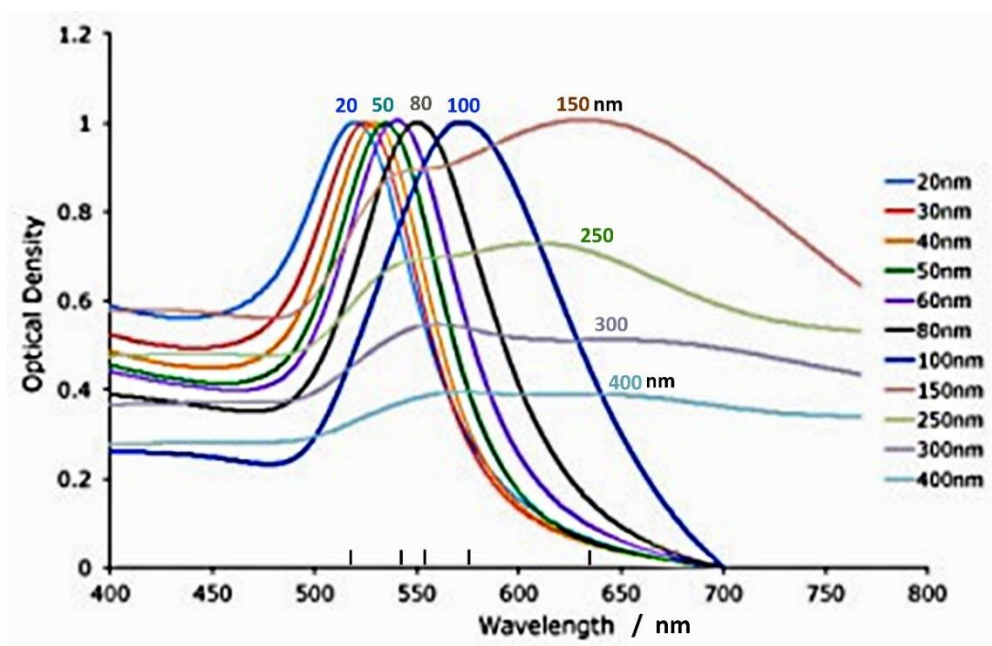

Figure 12. Theorical extinction spectra of 20-400 nm gold nanoparticles in aqueous solution.

Anisotropic particles (Figure 13), such as rods and prisms, have two bands, one associated with the resonance of plasmons in the transverse direction, at shorter wavelengths (for example, 520 nm), and the other in the longitudinal direction, at longer wavelengths (for example, 700 nm).
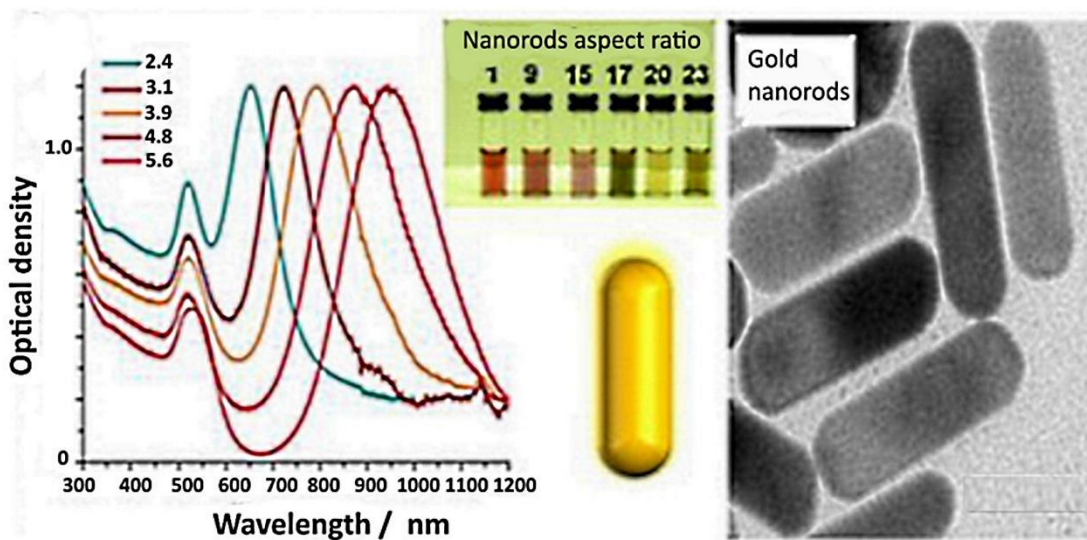

Figure 13. Extinction spectra of gold nanorods of several aspect ratios in aqueous solution.

When two plasmonic nanoparticles approach at a distance at least 5 times smaller than their respective radii, the electromagnetic radiation, by exciting the surface plasmons, can cause their coupling in the longitudinal direction, generating a new resonant band of greater wavelength (> 700 nm), while the original band is preserved, as illustrated in Figures 14. The emergence of this plasmonic coupling band is noticeable by the color change, from red to blue, thus signaling the aggregation phenomenon.
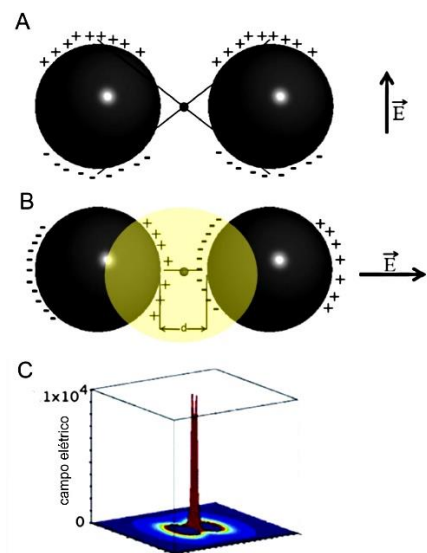
Figure 14. Transversal (A) and longitudinal (B) charge distribution at two nanoparticles interface, illustrating the "hot spot" region (B,C) with the corresponding electric field amplification (adapted from reference [52].

The coupling of two nanoparticles can be induced chemically, replacing the electrically charged complexing layer, by another neutral one, anchored more strongly on the gold surface by -SH groups (thiols), -S- (thiolates) or other coordinating sulfur bases . An example of this is provided by the reaction of cit-AuNPs with 4-mercaptopyrazine (pzSH) (Figure 15). This reaction is accompanied by a rapid color change from red to blue, indicating the exchange of citrate ions for 4-pzSH, and is driven by the strong affinity of the SH groups for gold atoms [60].
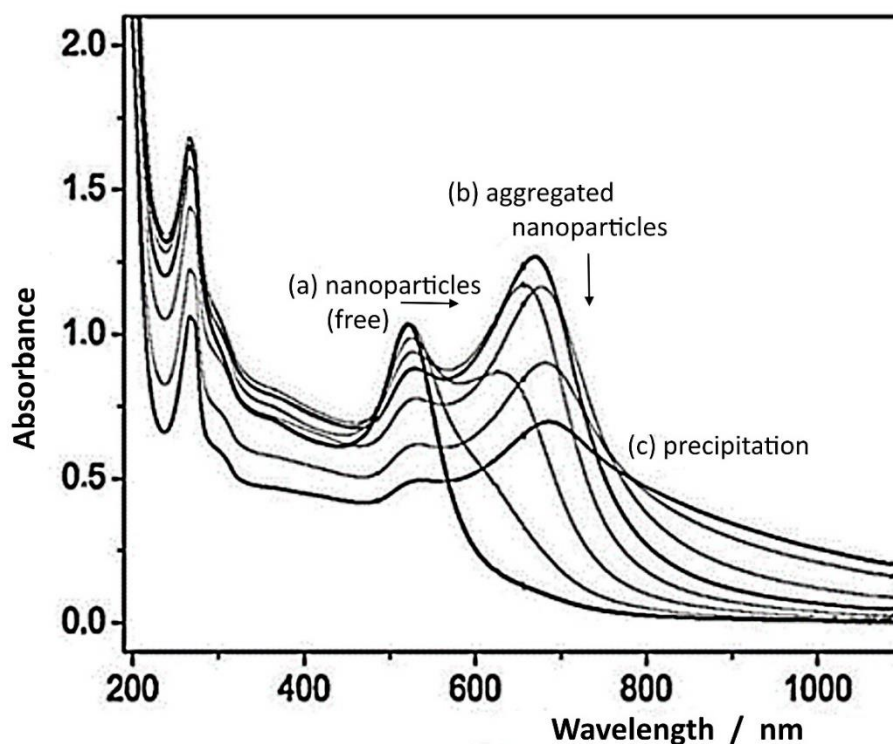
Figure 15. Typical spectral changes of cit-gold nanoparticles (a) after inducing aggregation with 4-mercaptopyrazine (b) followed by precipitation (c) (adapted from reference [52]).

6) SERS EFFECT

When nanoparticles agglomerate, the longitudinal plasmonic coupling, at their confluence, gives rise to a strong field, known as a "hot spot". Molecules located in this interparticle region exhibit greatly Raman scattering. Thus, all factors that influence the intensity of the plasmonic electric field and the extinction spectrum of nanoparticles become important to understand the SERS behavior of adsorbed molecules.

The enhancement by the electromagnetic effect reaches its maximum value when the radiation frequency coincides with the peak observed in the nanoparticle extinction spectrum. A molecule adsorbed on the surface will have its polarizability affected by the exciting radiation field, behaving like an oscillating dipole, whose different frequency in relation to the exciting radiation leads to the inelastic scattering that characterizes the Raman effect. The intensity of scattering grows with the generated electric field, and the mechanism involved is known as electromagnetic, EM.

In the case of non-spherical or anisotropic nanoparticles, the electric field associated with plasmons is concentrated mainly at their tips or extremities. Likewise, edge effects on corrugated surfaces, nanostructures and nanocavities also lead to heightened electric fields. Nanoparticles with different geometries have been developed for applications in SERS, including rods, triangles, bipyramids, disks, cubes, icosahedrons and stars, in addition to hollow spheres. The influence of geometry may be related to the anisotropy of nanoparticles, generating electric dipoles and quadrupoles in the transverse and longitudinal direction, with the appearance of more than one plasmonic scattering band. In addition, plasmonic electric fields are concentrated mainly at the tips, creating "hot spots" that greatly intensify SERS signals. There is already a wide variety of SERS probes on the market, usually coupled to a small instrumentation, dedicated to this type of analysis, at a low cost

In addition to the electromagnetic (EM) effect, exciting radiation can also interact with the electronic levels of adsorbed molecules, as well as with those arising from the molecular interaction with the metallic interface. When the resonant Raman (RR) effect occurs with molecules exposed to the plasmonic electromagnetic field, the synergism of the RR and EM effects leads to a very large increase in intensity, and the mechanism becomes known as SERRS, or resonant SERS. This effect reaches its maximum value when the frequency of the exciting radiation coincides with the absorption band of the molecule, and is very similar to the resonant Raman effect, but the scattering is more intense because it occurs under the influence of the surface electromagnetic field [61][12]

When molecules chemically interact with nanoparticles, the electron density transfer that accompanies the chemical bond is a function of the energy difference between the donor or occupied molecular orbitals (HOMO) and the Fermi level, or between this level and the empty molecular orbitals. or receptors, of the molecule. This process is called charge transfer, TC. Like the RR mechanism, the charge transfer excitation can also be resonant with the plasmonic field, causing a large enhancement of the SERS effect. These three effects, which are simultaneously enhanced by the electric field, are illustrated in Figure 16.
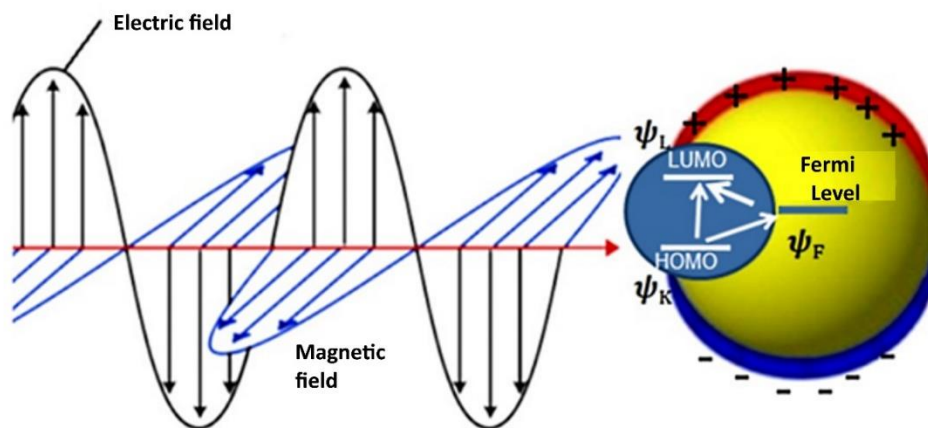
Figure 16. Interaction of the electromagnetic radiation with the surface plasmons and SERS effect involving resonance Raman (RR) and charge-transfer (CT) excitation of a molecule (HOMO/LUMO) to(from) the nanoparticle Fermi level.

When all factors act simultaneously, the enhancement provided by the SERS effect can reach 14 orders of magnitude, making it possible to detect a single molecule, anchored on the surface. An unified approach for SERS has been proposed by Lombardi and Birke [12,61] according to the equation

$$R_{IFK}(\omega) = \frac{\mu_{KI}\mu_{FK}h_{IF}\langle i|Q_k|f\rangle}{[(\varepsilon_1(\omega) + 2\varepsilon_m)^2 + \varepsilon_2^2](\omega_{FK}^2 - \omega^2 + \gamma_{FK}^2)(\omega_{IK}^2 - \omega^2 + \gamma_{IK}^2)}$$

This formalism is better appreciated in the scheme shown in Figure 17, where the first term in the denominator corresponds to the electromagnetic mechanism (A), the middle term represents the charge-transfer mechanism (B), and the third term reflects the resonance Raman excitation, in the presence of the electromagnetic radiation. The terms in the numerator corresponds to the classical transition dipole moments and polarizability tensors involved in the Raman effect.
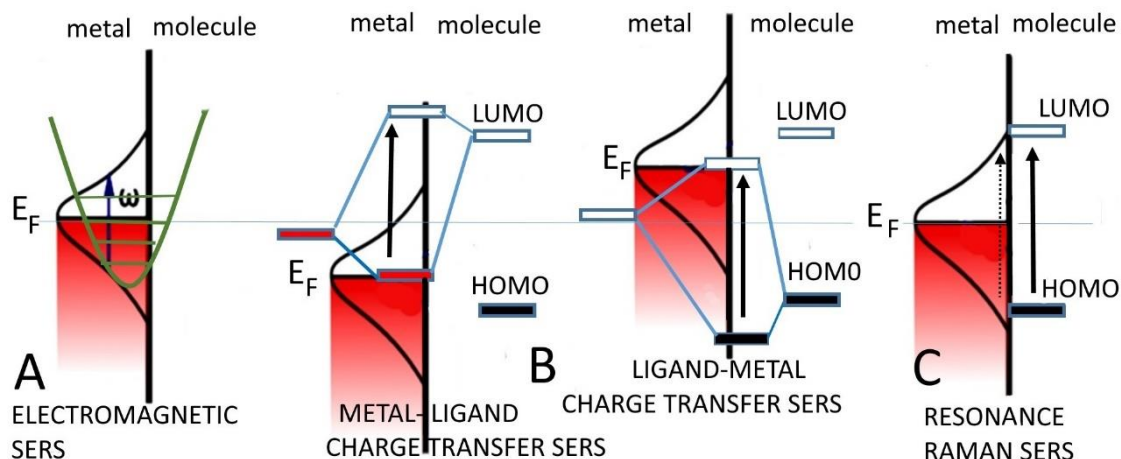
Figure 17. Representation of Lombardi and Birke unified model for SERS, involving (A) electromagnetic, (B) charge-transfer and C(resonance Raman) contributions. Adapted from reference [62].

Species anchored on gold nanoparticles can be used as SERS probes, by exploring the changes in Raman spectra induced by substrates or analytes. SERS probes generally consist of small aromatic molecules with thiol groups, such as benzenetiophenol derivatives, $R-C_6H_4-SH$, mercaptopyridine, NC_5H_5SH, and trimercaptotriazine, TMT or $C_3N_3(SH)_3$. These molecules show very intense and defined SERS signals, serving as spectroscopic markers in chemical and biological systems.

Ligands which exhibits SERS response when combined with plasmonic nanoparticles, allow probing metal ions by forming surface complexes and changing their Raman profiles. In this way, thanks to the great sensitivity of the SERS effect, their analytical detection is greatly improved. A classical example are the trimercaptotriazine (TMT) functionalized gold nanoparticles [63] (Figure 18) In this case, because of the multiple coordination sites of TMT, the binding of the molecule to the gold surface leaves heterocyclic nitrogen and thiol groups free for interacting with metal ions in solution. Thus, it has allowed the analysis of toxic metal ions, such as Hg^{2+} and Cd^{2+} with high sensitivity [63], and in a very practical way, as illustrated in Figure 18.
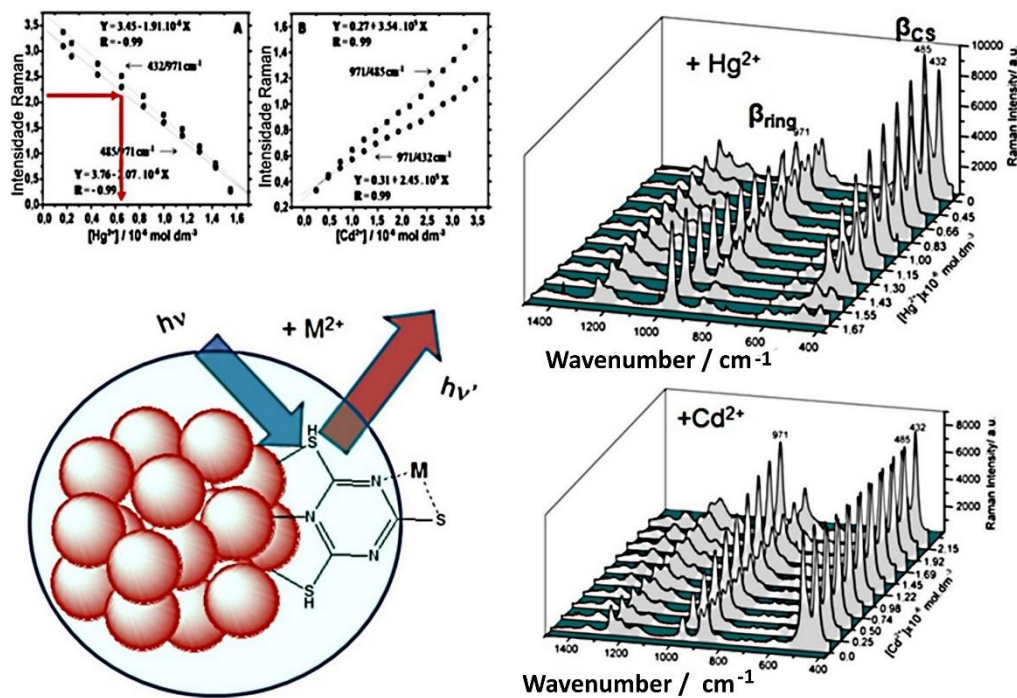
Figure 18- Composition of images showing variations in the Raman spectrum of trimercaptotriazine anchored in gold nanoparticles, in the presence of Hg^{2+} or Cd^{2+} ions, and the linear correlation of the intensity ratio of two typical bands, with the concentration of the heavy metal [63].

This particular example is particularly interesting, since the observed SERS pattern varies specifically with the concentration of metal ions, reflecting the involvement of different binding modes of the probe around the particle. Thus, based on the distinct Raman responses with concentration, one can use the intensity ratios of two selected peaks to perform the analysis, as illustrated in Figure 18. The method is quite simple, and requires just one drop of the solution.

7) PERSPECTIVES

Nowadays, nanoparticles are creating an important bridge between chemistry, nanotechnology and medicine [64–68]. In particular, hyperspectral microscopy is contributing to the progress in this area, allowing to expand the knowledge of the chemistry of the functionalized nanoparticles and their applications.

Unfortunately, the scope of this thesis was seriously affected by the COVID-19 pandemics after 2019. For this reason, many dreams have to be postponed and are being just mentioned in this perspective section. They actually conveyed a numerous work and experiments, still deserving investiments in the future. Our major dream was the development of **hyperspectral electrochemical analysis using screen printed electrodes**. This is yet a rather new subject, aiming to explore the electrode surfaces and their electrochemical response in association with the hyperspectral analysis, using for instance plasmonic nanoparticles. The basic idea was to combine the extreme sensitivity provided by the SERS response, with the electrochemical behavior of analytes, but in the nanometric domain, involving nanoparticles. Our preference for screen printed electrodes was associated with their portability and possibility of performing direct imaging in the hyperspectral microscope.

To perform hyperspectral electrochemical analysis, it is necessary (1) to investigate the nature of the screen printed electrodes, (2) to develop new procedures for anchoring nanoparticles on their surfaces, without poisoning their electrochemistry, (3) to learn how to work and combine the optical and electrochemical detection responses, aiming a new, advanced sensor with nanotechnological performance.

We believe that this approach can have a dramatic importance in chemistry, medicine and nanotechnology, combining spectral, electrochemical and microscopic features simultaneously. This is indeed rather challenging.

A first attempt showing how confocal hypermicroscopy can impact Analytical Chemistry, can be seen in an old publication of the group, elucidating the Feigl´s spot tests for palladium, using nickel and dimethylglyoxime [69]. This work elucidated the nature of the paladium complex and the formation of structures protecting the nickel complex, by directly observing them in the hyperspectral images. This message supports the consideration of how beautiful Analytical Chemistry could be, if one could directly see the reagents and products in real time, in the nanoscale hyperspectral image!

Pursuing our dream, we started investigating the surface morphology of screen printed gold and carbon electrodes, using electron microscopy, as exemplified in Figures 19,20.
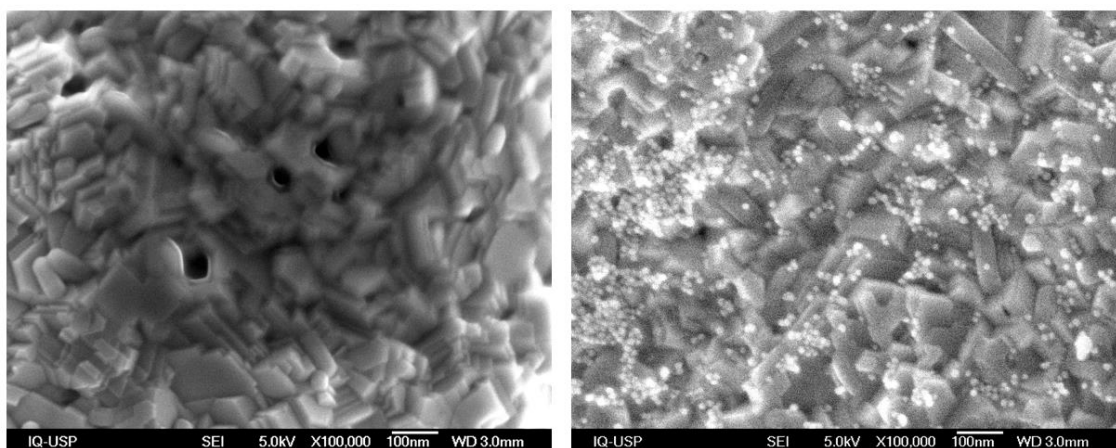
Figure 19. SEM images of screen printed gold electrode (left) and after application of cysteamine functionalized gold nanoparticles (right).
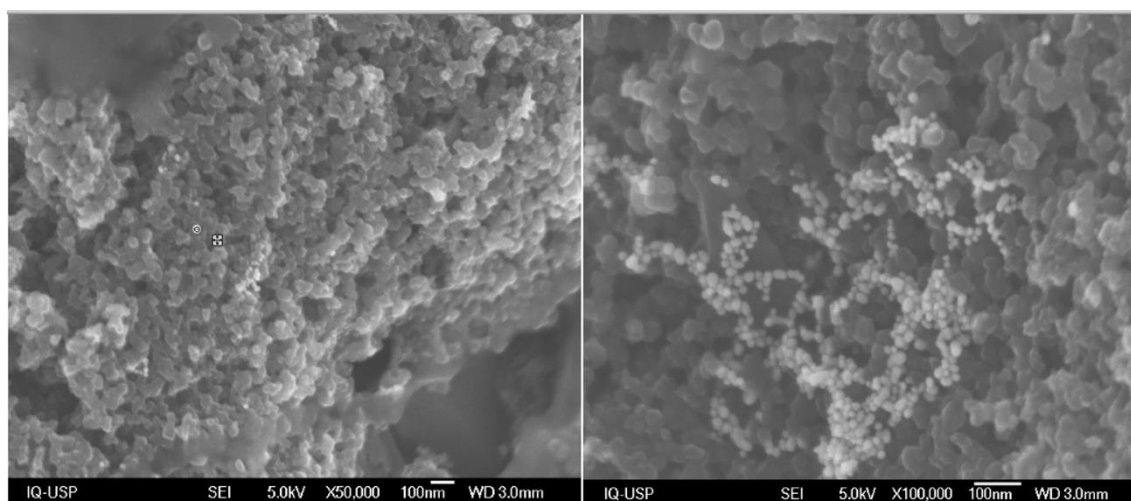

Figure 19. SEM images of screen printed carbon electrodes (left) and after the deposition of Turkevich gold nanoparticles (right).

These electrodes exhibited a good conductivity and electrochemical response. We learned that, in the case of the gold electrode, the rugosity is not enough to yield direct SERS response. Many attempts have been performed to improve this, with little success, even, by performing successive electrochemical cycling. Surprisingly, this strategy, which has proved effective to create rugosities in flat gold, silver and copper electrodes, was not successful in the case of screen printed electrodes. For this reason, our efforts were concentrated on chemically binding of gold nanoparticles to the screen printed electrodes, to explore their electrochemical and SERS behavior.

For this purpose, the electrodes were functionalized with bridging ligands such as shown in Figure 21, including cysteamine, exploring the natural affinity between gold and sulfur atoms.
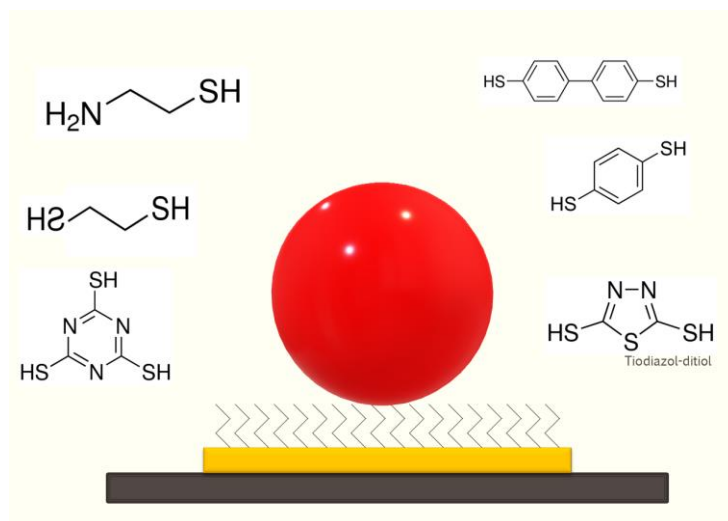
Figure 21. Typical bridging ligands for anchoring gold nanoparticles on screen printed gold electrodes and performing self assembled gold nanolayers.

In the case of cysteamine, a positively charged interface can be generated, being capable of anchoring negatively charged Turkevich gold nanoparticles. Self assembled gold monolayers can also be deposited using the bridging ligands. The initial results were quite exciting, as shown in Figure 22.

Figure 22. Self assembled monolayer of gold TMT nanoparticles onto a gold screen printed electrode, probed by cyclic voltammetry.

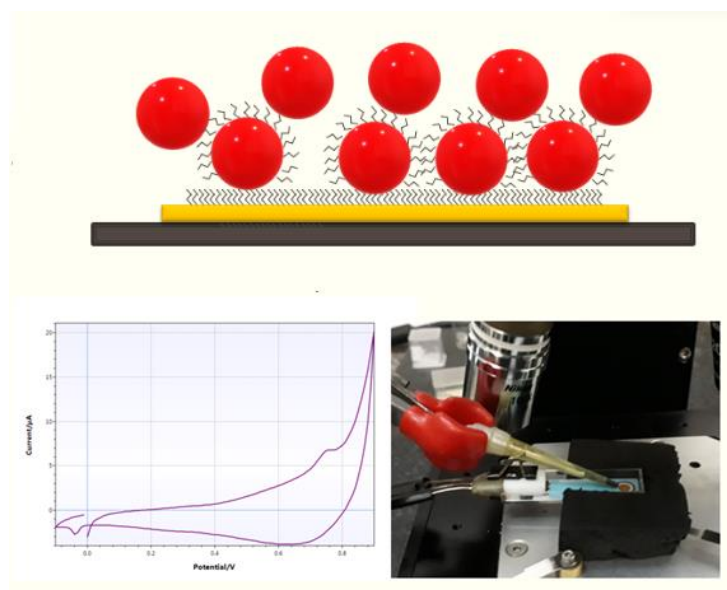The SERS signals from the screen printed electrodes were recorded as a function of the applied potentials, allowing to detect the signals and electrochemical response of the adsorbed species, as illustrated in Figure 23.
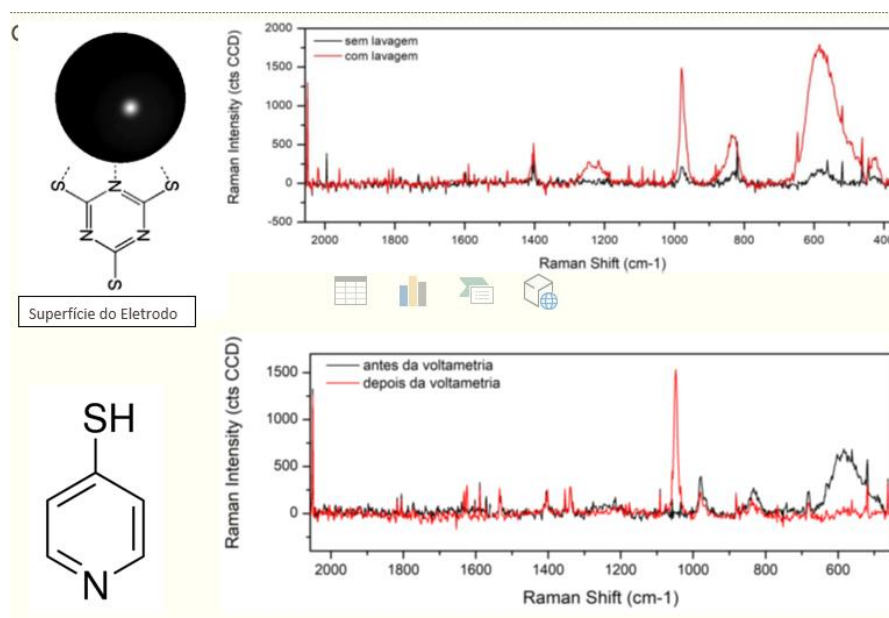
Figure 23. Typical SERS spectroelectrochemical of a TMT modified screen printed electrode, and after adding a drop of diluted 4-mercaptopyridine solution, followed by a cyclic voltammetry scan.

Unfortunately, the research was dramatically interrupted by the COVID-19 pandemics. Life has changed our the plans, directing to a new life in Japan, far from the Academic World. But the ideas remain quite alive, and will be pursued by the next generations of chemists in our group. The global results reported in this thesis reflect more than 7 years of intensive research in the laboratory. They still support our hope, as a dream come true, to be accomplished some day…

REFERENCES

[1]   V. Vodyanoy, O. Pustovyy, A. Vainrub, High resolution light microscopy of nanoforms, in: R.B. Hoover, G. V. Levin, A.Y. Rozanov, P.C.W. Davies (Eds.), Proceedings SPIE6694, San Diego, CA, 2007: pp. 669413-669413–12. https://doi.org/10.1117/12.731462.

[2]   A. Vainrub, O. Pustovyy, V. Vodyanoy, Resolution of 90 nm (λ/5) in an optical transmission microscope with an annular condenser, Opt Lett. 31 (2006) 2855. https://doi.org/10.1364/OL.31.002855.

[3]   D. Grasseschi, A.L.A. Parussulo, V.M. Zamarion, R.R. Guimaraes, K. Araki, H.E. Toma, How relevant can the SERS effect in isolated nanoparticles be?, RSC Adv. 3 (2013) 24465–24472. https://doi.org/10.1039/c3ra41818a.

[4]   D. Grasseschi, A.L.A. Parussulo, V.M. Zamarion, R.R. Guimaraes, K. Araki, H.E. Toma, SERS studies of isolated and agglomerated gold nanoparticles functionalized with a dicarboxybipyridine-trimercaptotriazine-ruthenium dye, J Raman Spectrosc. 45 (2014) 758–763. https://doi.org/10.1002/jrs.4562.

[5]   D. Grasseschi, F.S. Lima, M. Nakamura, H.E. Toma, Hyperspectral dark-field microscopy of gold nanodisks, Micron. 69 (2015) 15–20. https://doi.org/10.1016/j.micron.2014.10.007.

[6]   M.F.G. Huila, N. Lukin, A.L.A. Parussulo, P.V. Oliveira, P.K. Kyohara, K. Araki, H.E. Toma, Unraveling the mysterious role of palladium in feigl bis (dimethylglyoximate)nickel(II) spot tests by means of confocal raman microscopy, Anal Chem. 84 (2012). https://doi.org/10.1021/ac3003352.

[7]   S.M. Paula, M.F.G. Huila, K. Araki, H.E. Toma, Confocal Raman and electronic microscopy studies on the topotactic conversion of calcium carbonate from Pomacea lineate shells into hydroxyapatite bioceramic materials in phosphate media, Micron. 41 (2010) 983–989. https://doi.org/10.1016/j.micron.2010.06.014.

[8]   M.K. Uchiyama, D.K. Deda, S.F. De Paula Rodrigues, C.C. Drewes, S.M. Bolonheis, P.K. Kiyohara, S.P. De Toledo, W. Colli, K. Araki, S.H.P. Farsky, In vivo and In vitro toxicity and anti-inflammatory properties of gold nanoparticle bioconjugates to the vascular system, Toxicol Sci. 142 (2014). https://doi.org/10.1093/toxsci/kfu202.

[9]   H.E. Toma, J. Da Silva Shinohara, D. Grasseschi, J.D. Shinohara, D. Grasseschi,

Confocal Raman microscopy and hyperspectral dark field microscopy imaging of chemical and biological systems, Proc SPIE Nanoscale Imaging, Sensing, Actuation Biomed Appl XII,. 9337 (2015) 933702. https://doi.org/10.1117/12.2087618.

[10] R.F. Aroca, Plasmon enhanced spectroscopy., Phys Chem Chem Phys. 15 (2013) 5355–63. https://doi.org/10.1039/c3cp44103b.

[11] S. Eustis, M.A. El-Sayed, Why gold nanoparticles are more precious than pretty gold: noble metal surface plasmon resonance and its enhancement of the radiative and nonradiative properties of nanocrystals of different shapes., Chem Soc Rev. 35 (2006) 209–17. https://doi.org/10.1039/b514191e.

[12] J.R. Lombardi, R.L. Birke, The theory of surface-enhanced Raman scattering., J Chem Phys. 136 (2012) 144704. https://doi.org/10.1063/1.3698292.

[13] J.S. Shinohara, D. Grasseshi, S.N. Almeida, H.E. Toma, Exploring the metallochromic behavior of pentacyanidoferrates in visual, electronic and Raman spot tests, An Acad Bras Cienc. 90 (2018) e20180315.

[14] H.E. Toma, J.M. Malin, Properties and reactivity of some pentacyanoferrate(II) complexoes of aromatic N-heterocycles, Inorg Chem. 12 (1973) 1039–1045.

[15] H.E. Toma, J.M. Malin, Kinetics of Formation and Stability Constants of Some Pentacyanoferrate(II) Complexes of Aromatic Nitrogen Heterocycles, Inorg Chem. 12 (1973) 2080–2083. https://doi.org/10.1021/ic50127a026.

[16] H.E. Toma, E. Giesbrecht, R.L. Espinoza Rojas, Spectroscopic and electrochemical studies on linkage isomerism in iron(II) complexes of benzotriazole, a corrosion inhibitor, Can J Chem. 61 (1983) 2520–2525. https://doi.org/10.1139/v83-434.

[17] H.E. Toma, C. Creutz, Pentacyanoferrate(II) complexes - evaluation of their formal potentials and mechanism of quenching of (2,2'-bipyridine)Ruthenium(II) luminescence, Inorg Chem. 16 (1977) 545–550.

[18] H.E.H.E. Toma, E. Stadler, Basicity Constants of Iron(II) and Ruthenium(II) Complexes of 2,6-Dimethylpyrazine, Inorg Chem. 24 (1985) 3085–3088. https://doi.org/10.1021/ic00213a045.

[19] H.E.H.E. Toma, D. Oliveira, A.T.A.T. Meenochite, Analytical determination of dimethyl sulphoxide by complex formation with the pentacyanoferrate(II) ion, Talanta. 35 (1988) 323–325. https://doi.org/10.1016/0039-9140(88)80096-1.

[20] H.E.H.E. Toma, J.M.J.M. Malin, E. Giesbrecht, Ion pentacyano

(dimethylsulfoxide)ferrate(II) - Synthesis, characterization and substitution kinetics in aqueous solution, Inorg Chem. 12 (1973) 2084–2089. https://doi.org/10.1021/ic50127a027.

[21] H.E.H.E. Toma, J.M.J.M. Malin, Dissociation Kinetics of Pentacyanoiron(II) Complexes of Ammonia and Methylamine, Inorg Chem. 13 (1974) 1772–1774. https://doi.org/10.1021/ic50137a050.

[22] H.E. Toma, Iintervalence transfer in outer sphere hexamine ruthenium(III) pentacyanoferrate(II) complexes., J Chem Soc Dalt Trans. (1980) 471–474.

[23] E. Toma, L. Espinoza, Spectroscopic and electrochemical studies on linkage isomerism in iron(I1) complexes of benzotriazole, a corrosion inhibitor, (1983).

[24] H.E. Toma, E. Giesbrecht, J.M. Malin, E. Fluck, Correlations of Mossbauer and visible-UV spectra with aqueous substitution kinetics in several substituted pentacyanoferrate(II) complexes, Iinorganic Chim Acta. 14 (1975) 11–15.

[25] H.E. Toma, A.B.P. Lever, Spectroscopic and kinetic studies on a sereis of dinuclear to heptanuclear tris(bipyrzine)ruthenium(II)-pentacyanoferrate(II) complexes in aqueous solution, Inorg Chem. 25 (1986) 176–181. https://doi.org/10.1021/ic00222a017.

[26] H.E. Toma, J.M. Martins, E. Giesbrecht, Kinetics of reaction of imidazole, glycine and L-hystidine with aquapentacyanoferrate(II) ion, J Chem Soc - Dalt Trans. (1978) 1610–1617. https://doi.org/10.1039/dt9780001610.

[27] H.E. Toma, A.A. Batista, H.B. Gray, Pentacyanoferrate(II) Complexes of Amino Acids, J Am Chem Soc. 104 (1982). https://doi.org/10.1021/ja00390a020.

[28] A.P. Mangoni, B.B.N.S. Brandão, J.S. Shinohara, A.T. Silveira, M. Nakamura, H.E. Toma, Raman studies of bis(phenylterpyrazine)iron(II) and supramolecular species with pentacyanidoferrate(II) ions, Quim Nova. 42 (2019). https://doi.org/10.21577/0100-4042.20170415.

[29] D. Grasseschi, M.L. de O. Pereira, J.S. Shinohara, H.E. Toma, Facile synthesis of labile gold nanodiscs by the Turkevich method, J Nanoparticles Res. 20 (2018) 35. https://doi.org/10.1007/s11051-018-4149-y.

[30] D. Oliveira, J.D. Shinohara, H.E. Toma, Gold nanoparticle conjugation with microtubules for nanobiostructure formation, J Bionanoscience. 12 (2018) 271–277. https://doi.org/10.1166/jbns.2018.1521.

[31] J.C. da Rocha, J. V. Mattioni, L.M. Sihn, J.S. Shinohara, F.M. Melo, M.P. Franco, A.A.C. Braga, H.E. Toma, Room temperature synthesis and Raman

spectral evidence of carbon bond ranelate–gold nanoparticles, J Raman Spectrosc. 51 (2020) 1083–1091. https://doi.org/10.1002/jrs.5872.

[32]   J.A. Fan, K. Bao, J.B. Lassiter, J. Bao, N.J. Halas, P. Nordlander, F. Capasso, Near-Normal Incidence Dark-Field Microscopy: Applications to Nanoplasmonic Spectroscopy, Nano Lett. 12 (2012) 2817–2821. https://doi.org/10.1021/nl300160y.

[33]   W. Wang, N. Tao, Detection, counting, and imaging of single nanoparticles, Anal Chem. 86 (2014) 2–14. https://doi.org/10.1021/ac403890n.

[34]   M. Liu, J. Chao, S. Deng, K. Wang, K. Li, C. Fan, Dark-field microscopy in imaging of plasmon resonant nanoparticles, Colloids Surfaces B Biointerfaces. (2014) 1–7. https://doi.org/10.1016/j.colsurfb.2014.06.001.

[35]   Y. Peng, B. Xiong, L. Peng, H. Li, Y. He, E.S. Yeung, Recent Advances in Optical Imaging with Anisotropic Plasmonic Nanoparticles, Anal Chem. 87 (2015) 200–215. https://doi.org/10.1021/ac504061p.

[36]   G.A. Roth, S. Tahiliani, N.M. Neu-Baker, S. a. Brenner, Hyperspectral microscopy as an analytical tool for nanomaterials, Wiley Interdiscip Rev Nanomedicine Nanobiotechnology. (2015) n/a-n/a. https://doi.org/10.1002/wnan.1330.

[37]   C. Sönnichsen, Plasmons in metal nanostructures, Dissertation. 27 (2001) 134. http://edoc.ub.uni-muenchen.de/2367/1/Soennichsen_Carsten.pdf.

[38]   R.A. Zsigmondy, Properties of colloids (Nobel lecture), Prop Colloids (Nobel Lect. 1 (1926).

[39]   A.W. Hartman, Dark-field microscopy of transparent objects with a bright-field objective, Rev Sci Instrum. 59 (1988) 502–503. https://doi.org/10.1063/1.1139873.

[40]   H.-H. Lu, T.-C. Hsiao, S.-M. Hsu, C.-W. Lin, Optical Characterization of a 1-D Nanostructure by Dark-Field Microscopy and Surface Plasmon Resonance to Determine Biomolecular Interactions, IEEE Sens J. 10 (2010) 712–719. https://doi.org/10.1109/JSEN.2009.2038628.

[41]   G. Ehret, B. Bodermann, W. Mirandé, Quantitative linewidth measurement down to 100 nm by means of optical dark-field microscopy and rigorous model-based evaluation, Meas Sci Technol. 18 (2007) 430–438. https://doi.org/10.1088/0957-0233/18/2/S15.

[42]   G. Ehret, B. Bodermann, W. Mirande, Improved optical linewidth measurement

by means of alternating dark field illumination and model-based evaluation, in: W. Osten, C. Gorecki, E.L. Novak (Eds.), Measurement, 2005: pp. 367–376. https://doi.org/10.1117/12.612460.

[43] L.B. Sagle, L.K. Ruvuna, J.M. Bingham, C. Liu, P.S. Cremer, R.P. Van Duyne, Single plasmonic nanoparticle tracking studies of solid supported bilayers with ganglioside lipids, J Am Chem Soc. 134 (2012) 15832–15839. https://doi.org/10.1021/ja3054095.

[44] Y. Gu, X. Di, W. Sun, G. Wang, N. Fang, Three-dimensional super-localization and tracking of single gold nanoparticles in cells, Anal Chem. 84 (2012) 4111–4117. https://doi.org/10.1021/ac300249d.

[45] S. Sheikholeslami, Y.W. Jun, P.K. Jain, a. P. Alivisatos, Coupling of optical resonances in a compositionally asymmetric plasmonic nanoparticle dimer, Nano Lett. 10 (2010) 2655–2660. https://doi.org/10.1021/nl101380f.

[46] R. Thar, N. Blackburn, M. Kühl, A new system for three-dimensional tracking of motile microorganisms, Appl Environ Microbiol. 66 (2000) 2238–2242. https://doi.org/10.1128/AEM.66.5.2238-2242.2000.

[47] L. Xiao, Y. Qiao, Y. He, E.S. Yeung, Imaging translational and rotational diffusion of single anisotropic nanoparticles with planar illumination microscopy, J Am Chem Soc. 133 (2011) 10638–10645. https://doi.org/10.1021/ja203289m.

[48] P. Larkin, Infrared and Raman Spectroscopy, Elsevier, 2011.

[49] A.C. Albrecht, Theory of Raman Intensities, J Chem Phys. 34 (1961) 1476.

[50] S.P. Gubin, N.A. Kataeva, Coordination chemistry of nanoparticles, Russ J Coord Chem Khimiya. 32 (2006) 849–857. https://doi.org/10.1134/S1070328406120013.

[51] E.J. Verwey, J.T.G. Overbeek, Theory of stability of lyophobic colloids, Dover, New York, 2000.

[52] H. Toma, Nanotecnologia molecular - materiais e dispositivos, Edgard Blucher, Sao Paulo, 2016.

[53] R. Kamimura, T. Kondo, K. Motobayashi, K. Ikeda, Surface-Enhanced Electronic Raman Scattering at Various Metal Surfaces, Phys Status Solidi Basic Res. 259 (2022) 1–10. https://doi.org/10.1002/pssb.202100589.

[54] M. Faraday, The Bakerian Lecture: Experimental Relations of Gold (and Other Metals) to Light, Philos Trans R Soc London. 147 (1857) 145–181.

[55] M. Brust, M. Walker, D. Bethell, D.J. Schiffrin, R. Whyman, Synthesis of thiol-

derivatised gold nanoparticles in a two-phase Liquid?Liquid system, J Chem Soc Chem Commun. (1994) 801–802. https://doi.org/10.1039/c39940000801.

[56] J. Turkevich, P.C. Stevenson, J. Hillier, A study of the nucleation and growth processes in the synthesis of colloidal gold, Discuss Faraday Soc. 11 (1951) 55–75.

[57] J. Turkevich, P. Stevenson, J. Hillier, The formation of colloidal gold, J Phys Chem. 57 (1953) 670.

[58] D. Grasseschi, R.A. Ando, H.E. Toma, V.M. Zamarion, Unraveling the nature of Turkevich gold nanoparticles: the unexpected role of the dicarboxyketone species, RSC Adv. 5 (2015) 5716–5724. https://doi.org/10.1039/C4RA12161A.

[59] G. Mie, Colloidal solutions, Anallen Der Phys. 25 (1908) 377–445.

[60] S.H. Toma, J.A. Bonacin, K. Araki, H.E. Toma, Controlled Stabilization and Flocculation of Gold Nanoparticles by Means of 2-Pyrazin-2-ylethanethiol and Pentacyanidoferrate (II) Complexes, Eur J Inorg Chem. 21 (2007) 3356–3364. https://doi.org/10.1002/ejic.200700151.

[61] J.R. Lombardi, R.L. Birke, A Unified View of Surface-Enhanced Raman Scattering, Acc Chem Res. 42 (2009) 734–742.

[62] D. Grasseschi, H.E. Toma, The SERS effect in coordination chemistry, Coord Chem Rev. 333 (2017) 108–131. https://doi.org/10.1016/j.ccr.2016.11.019.

[63] V.M. Zamarion, R.A. Timm, K. Araki, H.E.H.E. Toma, Ultrasensitive SERS Nanoprobes for Hazardous Metal Ions Based on Trimercaptotriazine-Modified Gold Nanoparticles, Inorg Chem. 47 (2008) 2934–2936. https://doi.org/10.1021/ic800122v.

[64] A.S. Shah, B. Surnar, N. Kolishetti, S. Dhar, Intersection of Inorganic Chemistry and Nanotechnology for the Creation of New Cancer Therapies, Accounts Mater Res. 3 (2022) 283–296. https://doi.org/10.1021/accountsmr.1c00178.

[65] D. Wu, B. Zhou, J. Li, X. Wang, B. Li, H. Liang, Coordination-Driven Metal-Polyphenolic Nanoparticles toward Effective Anticancer Therapy, Adv Healthc Mater. 11 (2022) 1–11. https://doi.org/10.1002/adhm.202200559.

[66] Q. Sun, X. Xie, Y. Song, L. Sun, A review on silver-mediated DNA base pairs: methodology and application, Biomater Res. 26 (2022) 1–17. https://doi.org/10.1186/s40824-022-00254-w.

[67] B. Liu, J. Zhang, L. Li, Metal–DNA Coordination-Driven Self-Assembly: A Conceptual Methodology to Expand the Repertoire of DNA Nanobiotechnology,

Chem - A Eur J. 25 (2019) 13452–13457.
https://doi.org/10.1002/chem.201902501.

[68]   A. Kumar, J.M. Gonçalves, J.S.G. Selva, K. Araki, M. Bertotti, Correlating selective electrocatalysis of dopamine and ascorbic acid electrooxidation at nanoporous gold surfaces with structural-defects, J Electrochem Soc. 166 (2019). https://doi.org/10.1149/2.0821914jes.

[69]   M.F.G. Huila, N. Lukin, A.L.A. Parussulo, P. V Oliveira, P.K. Kyohara, K. Araki, H.E. Toma, Unraveling the mysterious role of palladium in Feigl bis(dimethylglyoximate)nickel(II) spot tests by means of confocal Raman microscopy., Anal Chem. 84 (2012) 3067–9. https://doi.org/10.1021/ac3003352.

Confocal Raman microscopy and hyperspectral dark field microscopy imaging of chemical and biological systems

Henrique E. Toma,[*] Jorge da Silva Shinohara, Daniel Grasseschi

Instituto de Química, Universidade de São Paulo, Av. Prof. Lineu Prestes 748, C.Postal 26077, CEP 05513-970, São Paulo, SP, Brazil.

ABSTRACT

Hyperspectral imaging can provide accurate information on the distribution of the chemical species in materials and biological samples, based on the analysis of their electronic and vibrational profiles. In special, confocal Raman microscopy is one of the best ways to access the chemical distribution of molecules, especially under resonance Raman or SERS conditions. On the other hand, enhanced dark field optical microscopy can be employed for hyperspectral imaging in the visible and near-IR region, while extending the optical resolution up to the nanoscale dimension. It allows the detection of gold or silver single nanoparticles, as well as spectral monitoring from the characteristic surface plasmon bands. These two hyperspectral microscopies can be conveniently combined to provide nanoscale electronic and vibrational information of the species present in a wide variety of chemical and biological systems. A case study focusing on the improvement of the classical spot-test analysis of nickel(II) ions with dithizone is here detailed. A great enhancement of sensitivity in the detection of nickel(II) ions, by at least 4 orders of magnitude, has been observed in this work. Hyperspectral measurements allowed the mapping of the gold nanoparticles (AuNP) distribution on cellulose fibers and on glass, and the evaluation of their extinction and SERS spectra for analytical purposes.

Keywords: Hyperspectral imaging, Confocal Raman, SERS, Gold Nanoparticles, Surface Plasmons.

1. INTRODUCTION

Hyperspectral microscopy is a modern way of exploring the imaging of materials and biological samples, conveying relevant spectral information of the molecules and nanoparticle constituents. By accessing the electronic or vibrational features embedded in every pixel, important analytical data can be obtained at the micro and nanoscale.

Recent progress in dark-field microscopy has extended the classical optical resolution limit ($\sim\lambda/2$) to $\lambda/5$, by exploring the higher resolution power from an oblique illumination, coupled with a cardoid annular condenser.[1,2] In particular, this technique is particularly rewarding in the case of plasmonic nanoparticles, such as gold and silver, because, in addition to a higher resolution, the enhanced light scattering induced by the plasmon resonance, propagates as a cone, generating a magnification response capable of discriminating individual nanoparticles.[3,4,5] In addition, by means of a coupled spectral detector, it is possible to record single nanoparticles scattering spectra, and generate the corresponding hyperspectral images from the collected data.

Another important tool is confocal Raman microscopy.[6] Conventional Raman signals are extremely weak, however the scattering intensities increase with the forth power of the exciting radiation. For this reason, Raman scattering became an outstanding spectroscopic and analytical strategy only after the introduction of lasers in the excitation process. Confocal Raman microscopy associates a high-resolution setup with the Raman signals, allowing to probe the molecular characteristics of the samples, from the vibrational data composing every pixel of the image. In the presence of plasmonic nanoparticles such as gold, the Raman signals can be dramatically enhanced, exceeding 12 orders of magnitude, by means of the so-called SERS effect (surface enhanced Raman scattering). In this way, the presence of plasmonic nanoparticles can be explored for analytical purposes, in association with their strong Raman scattering, allowing a great increase of sensitivity in the investigation of chemical and biological samples.

*henetoma@iq.usp.br; phone 55 11 30913887, jorge.shinohara@usp.br , daniel.grasseschi@gmail.com

Combination of dark-field and confocal Raman microscopy enables the investigation of plasmonic excitation and SERS effect in a variety of systems, particularly those containing nanoparticles as optical and spectral probes. Typical examples encompass the elucidation of the spectral characteristics of isolated and aggregated gold nanoparticles [3], the microscopy analysis of classical "spot-tests" in chemistry and forensics,[7] the chemical imaging of shells[8] and the phagocytosis of gold nanoparticles by neutrophyl cells.[9] In this article, the combined hyperspectral strategy is being explored as a new approach for improving the classical spot test analysis with the dithizone reagent for metal ions. The investigation was carried out on a filter paper and on a silanized glass, exploring the SERS effect of dithizone in the presence of gold nanoparticles.

The classical spot test experiment consists in impregnating a filter paper with the organic reagent dissolved in methanol, and observing the color changes after applying a drop of the metal ion solution. The detection is limited by the eyes sensitivity. Spot test analyses can be greatly improved using Raman spectroscopy, especially by exploring the strong signals from the chromophores in resonance with the exciting radiation. In addition, a further improvement can be achieved by means of the SERS effect associated with the gold nanoparticles.[10,11,12] Such strategy has allowed to reach a single molecule detection limit, thus exceeding, in performance, most of the existing analytical tools. Therefore, probing the interaction of plasmonic nanoparticles and molecules by means of combined hyperspectral microscopies, introduces an important strategy which can open many exciting perspectives in chemistry and biology.

2. METHODOLOGY

A CytoViva ultra-resolution imaging system, composed by a dark-field hyperspectral arrangement mounted on an Olympus BX51 microscope, was used for recording the single particles Rayleigh scattering spectra. The dark-field configuration generates a hollow light cone focused on the specimen. Only the light scattered and diffracted inside the cone reaches the objective, which has a numerical aperture smaller than the numerical aperture of the dark-field condenser. The zero order diffracted light is not collected, and the particles appears as bright spots on a dark background. It is possible to record a dark-field optical image composed by a three channel RGB spectra with a spatial resolution of 64 nm, and a hyperspectral image where each pixel has 64 nm and carries a full visible spectral information. Due to the enhanced light scattering of the plasmonic nanoparticles, which propagates like a cone, even smaller nanoparticles, e. g. 15 nm, can be easily visualized in the microscope. For achieving a better spectral signal to noise ratio, a binning process can be performed by summing four pixels in order to yield a new 128 nm pixel. In this way, a more well defined spectrum can be generated.

Confocal Raman microscopy measurements were performed with a WITec alpha-300R equipment using frequency-doubled Nd:YAG (λ = 532 nm), argon (λ = 488 nm) and He-Ne (λ = 633 nm) lasers, and a single mode optical fiber. Raman spectra images were obtained by scanning the sample surface in the *xy* direction with a piezo-driven *xyz* feedback controlled scan stage, while collecting a spectrum at every pixel, using a high sensitivity Andor Technology, Newton model EMCCD detector. All experiments were conducted using a Nikon objective (100×, NA=0.8), and a laser power output lower than 2 mW/cm^2 to avoid thermal decomposition of the sample.

Citrate-stabilized gold nanoparticles (cit-AuNP) were prepared according to the Turkevich[13] method modified by Frens.[14] For the dark-field and Raman hyperspectral measurements, the samples were prepared by drop casting 1 µl of Au nanoparticles suspension, after diluting by half with deionized water, on a NEXTERION® ultra-clean glass B (Schott). An ultra-clean NEXTERION® glass cover slip (Schott) was put over the drop, and sealed with adhesive tape to avoid oil penetration in the sample. The dark-field optical images and the Rayleigh scattering spectra were recorded with the sample wet, in order to keep the same refraction index.

3. RESULTS AND DISCUSSION

3.1. Light scattering by plasmonic nanoparticles

Metals such as gold, silver and copper exhibit loosely bound electrons in the external shell which can interact with the oscillating electromagnetic radiation, behaving as localized plasmons (Figure 1) Such interactions generate oscillating dipoles in the particles, influencing the light scattering and absorption phenomena, as a function of the dielectric constants of the metal, $\varepsilon = \varepsilon_1(\omega) + i\varepsilon_2(\omega)$, where ω is the oscillating frequency, and of dielectric constant of the external media, ε_m.
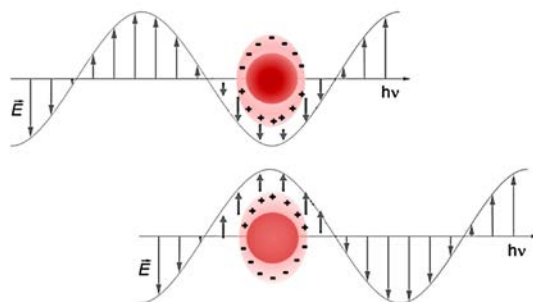
Figure 1. Oscillating dipoles accompanying the plasmon waves in gold nanoparticles.

The scattering and absorption processes contribute to the measured optical absorbance,

$$A = \frac{N \sigma_{ext} d}{2.303}$$

where N and σ_{ext} are the concentration and extinction cross-section of the nanoparticles, and d is the optical pathway. The first theoretical treatment of the light extinction process by nanoparticles was proposed by G. Mie in 1908.[15] It can be expressed by equation 1, where V is the nanoparticle volume.

$$\sigma_{ext} = 9 \left(\frac{\omega}{c}\right) \varepsilon_m^{3/2} V \left(\frac{\varepsilon_2(\omega)}{[\varepsilon_1(\omega) + 2\varepsilon_m]^2 + [\varepsilon_2(\omega)]^2} \right)$$

(1)

The resonance condition, where σ_{ext} is maximum, is achieved when $\varepsilon_1(\omega) = -2\varepsilon_m$. In aqueous solution, the extinction spectra of typical spherical gold nanoparticles exhibit a maximum in the 520-570 nm range. When the nanoparticles are deposited on glass, the extinction spectra are shifted to the red, because of the changes in the dielectric constant.

Isolated, spherical gold nanoparticles monitored in the dark-field microscope can be seen in Figure 2, in comparison with the corresponding scanning electron microscopy image. The light scattering spectra can also be seen in Figure 2.d.
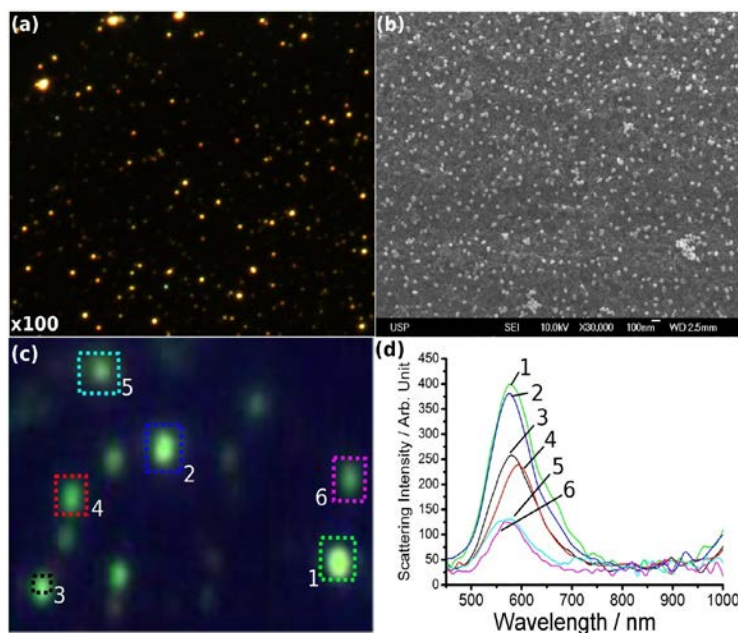

Figure 2. a) Dark-field, b) scanning electron microscopy, c) hyperspectral and d) scattering spectra of isolated gold nanoparticles (collected at spots 1-6) on glass. Figure reproduced with permission from ref. [3] COPYRIGHT 2013 Royal Society of Chemistry.

Aggregated nanoparticles can be seen in Figure 3. The scattering spectra of the aggregated nanoparticles are quite distinct from those of the isolated nanoparticles, and are dominated by the broad plasmon-coupling band in the 750-950 nm region.
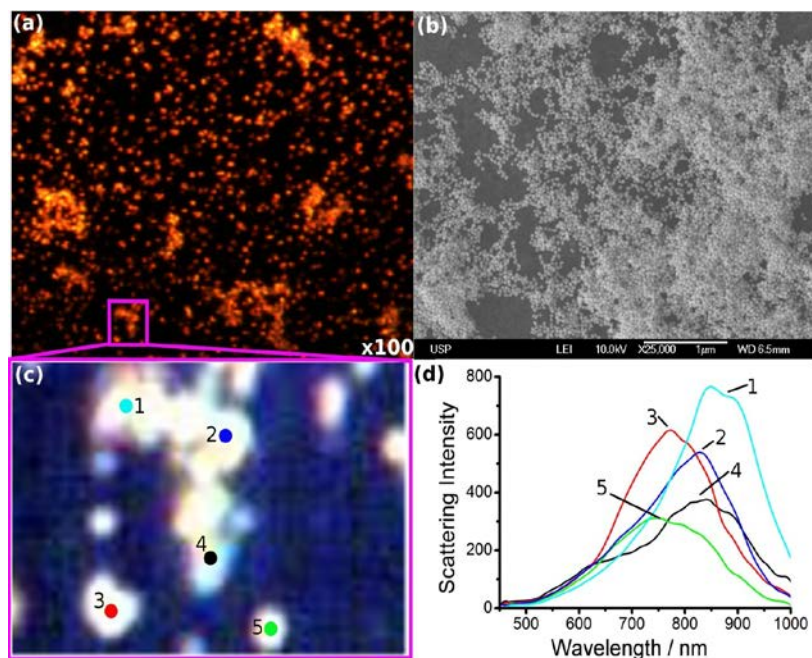

Figure 3. a) Dark-field, b) scanning electron microscopy, c) hyperspectral and d) scattering spectra of aggregated gold nanoparticles (collected at spots 1-6) on glass. Figure reproduced with permission from ref. [3] COPYRIGHT 2013 Royal Society of Chemistry.

## 3.2 Hyperspectral studies in spot test analysis

Dithizone, Dz (1) is a classical complexing agent, and its reaction with Ni(II) ions was chosen to illustrate the application of combined hyperspectral dark field and confocal Raman microscopy in spot test analysis.
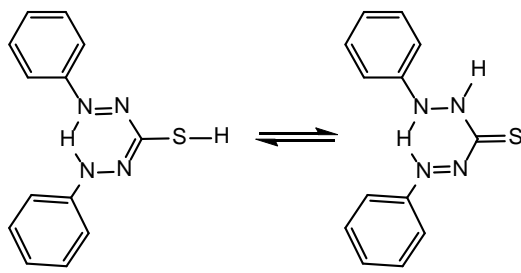
(1)

The Dz molecule exhibits a tautomeric thiol/thione equilibrium in aqueous and organic solutions, and the presence of the sulfur atom allows its interaction with gold nanoparticles,[16] by forming strong Au-S covalent bond, presumably in a bidentate coordination mode, as indicated in scheme (2).
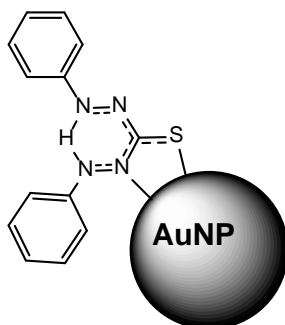
(2)

It should be noticed that most of the Raman and SERS studies are usually carried out with the samples dissolved or suspended in solution, or anchored on solid substrates. Aqueous solutions are particularly suitable for Raman studies, because of the lack of relevant signals from the solvent, in contrast with the infrared spectroscopy measurements. Cellulose, or paper, is also an excellent substrate in Raman spectroscopy, however, surprisingly, its use is relatively rare. In this regard, we have already shown that the Raman signals associated with most typical chromophores, such as those containing aromatic groups, are indeed much stronger than those arising from the paper substrate.[16]

In pure form, and under highly diluted conditions (e.g. 10^{-5} M) the Raman signals of Dz adsorbed on cellulose are too weak to be distinguished from the random noisy signals. However, in the presence of gold nanoparticles, the Dz Raman signals become very strong, as shown in Figure 4. The most strongly enhanced peaks of dithizone are observed at 1581 (νC=N + νC-N), 1336 (νN=N), 1162 (νN-Ph + δC-H), 998 (ring breathing), and 511 cm^{-1} (νC=S). According to the tentative assignments (shown in parenthesis) based on the literature,[17] the enhanced Raman peaks are mainly composed by C=S, N=N and C-N vibrations, thus supporting the binding of dithizone to the gold nanoparticles *via* the S and/or N atoms.
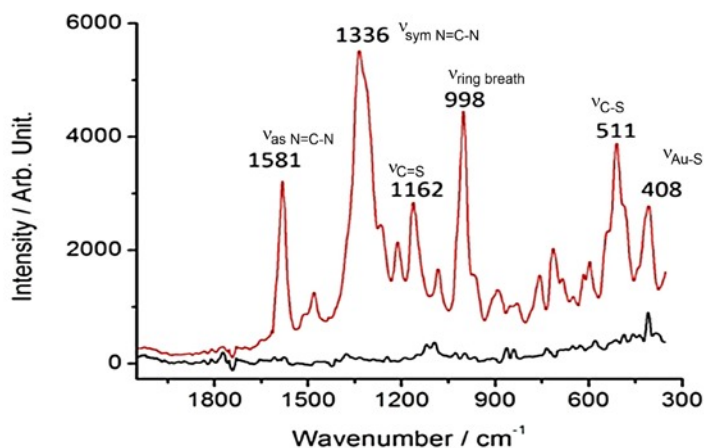

Figure 4. Raman spectra of paper impregnated with Dz (10^{-5} mol L^{-1}), bottom line and with Dz (10^{-5} mol L^{-1}) containing AuNP, top line.

At the micro and nanoscale, filter paper is not a flat or homogeneous surface material, but rather a collection of cellulose fibers, exposing hydroxyl groups for interacting with metal ions, organic reagents and nanoparticles. Although the Raman signals can be accurately recorded on this supporting material, because of the confocal optical resolution ($\sim$ 400 nm), the isolated gold nanoparticles cannot be individually probed as in the case of the dark-field microscopy, except when large aggregates are present. However, from the collected Raman signals, the hyperspectral image of the cellulose fibers containing gold nanoparticles can be obtained, as shown in Figure 5.
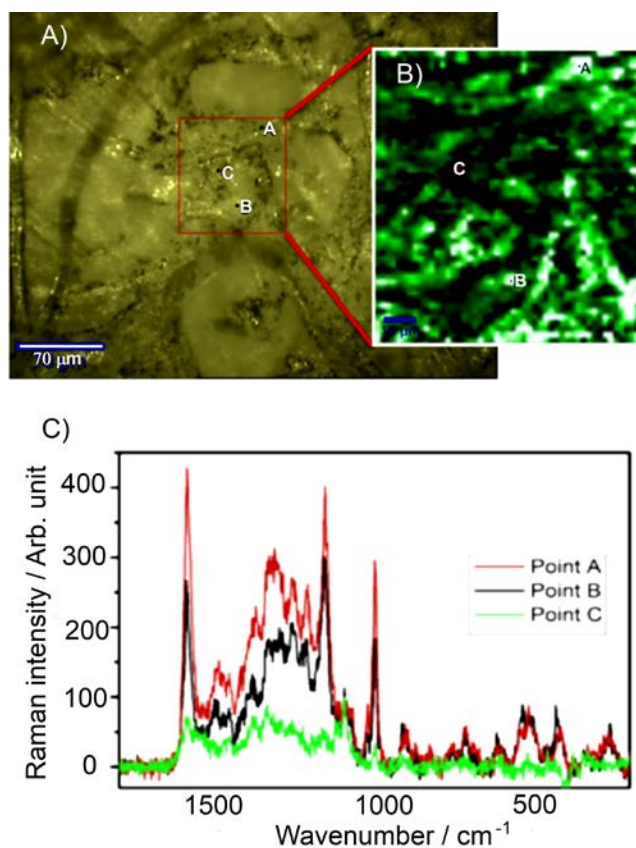
Figure 5. (A) Optical image of cellulose fibers impregnated with Dz-AuNP, (B) Image reconstructed using the peak area between 980 and 1020 cm^{-1}, (C) Raman spectra of tree different spots (point A = top, point C = bottom).

The Dz molecule anchored on the gold nanoparticles is able to bind metal ions, such as Ni^{2+}, by displacing the internal H atom (scheme 3). The SERS spectra recorded before and after the addition of Ni^{2+} ions are shown in Figure 6. The spectral changes are quite evident in this Figure, even at 10^{-6} M, particularly at 1341 cm^{-1} and 542 cm^{-1}, associated with the ν_{sym}N=C-N and νC-S vibrational modes, respectively. After incorporating nickel(II) ions, the rise of the new νC-S band at 520 cm^{-1} suggests a gradual conversion of the chelate binding mode in Au-Dz to a more symmetric monodentate binding of the sulfur group (scheme 3). The use of the SERS effect in spot test analysis improved the detection of nickel(II) ions by at least four orders of magnitude in relation to the conventional colorimetric test.
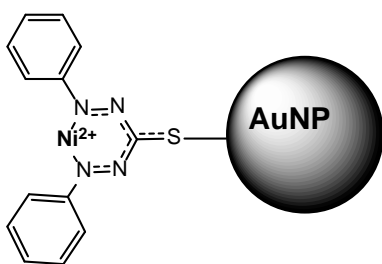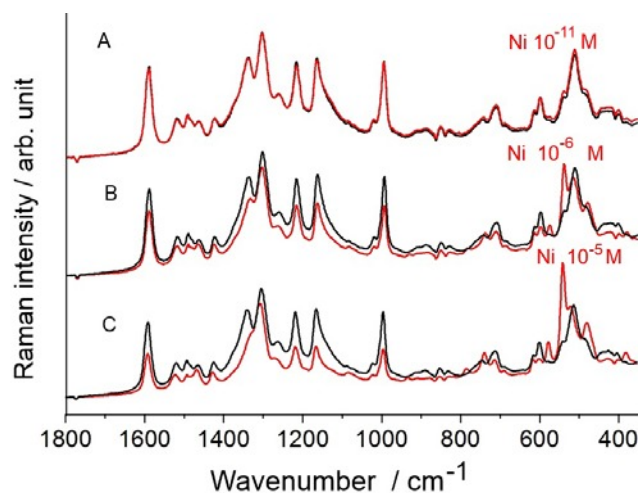

(3)

Figure 6. SERS response of paper impregnated with Dz-AuNP, before (black) and after (red) applying 10 μL of Ni^{+2} solution (λ_{exc} = 785 nm)

In order to observe the gold nanoparticules distribution on the cellulose, some fibers were removed from the filter paper and examined in the dark field microscope, as shown in Figure 7. In the hyperspectral image, the gold nanoparticles can be readily seen on the cellulose fibers, and their scattering spectra exhibit a broad band in the 800-850 nm range, corresponding to aggregated forms.
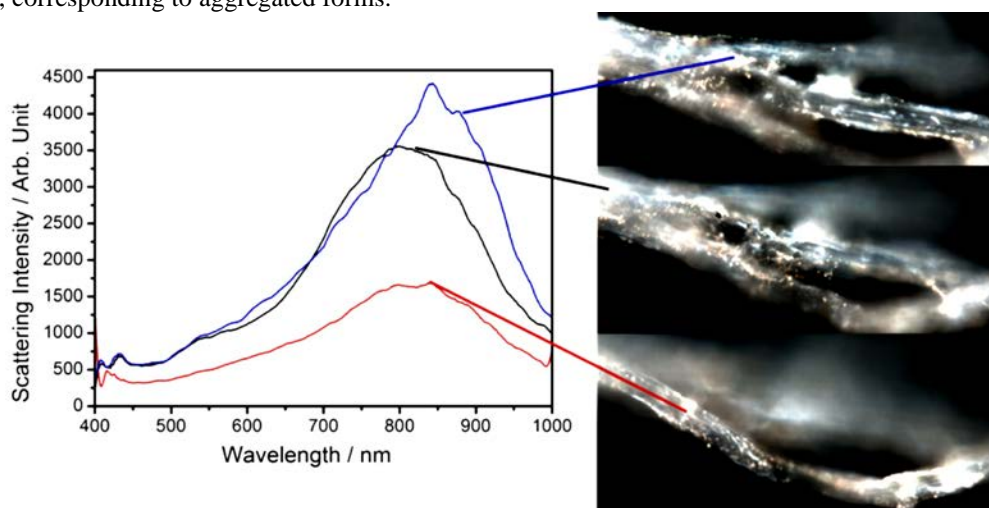

Figure 7. Dark field hyperspectral image of cellulose fibers wit Dz-AuNP and their respective scattering spectra.

Alternatively, the classical spot test analysis on filter paper was also performed by anchoring the gold nanoparticles on glass, after the appropriate surface functionalization with triethoxyaminopropylsilane (APTS). The surface concentration of the gold nanoparticles was carefully monitored as a function of time and concentrations. In the absence of Dz molecules, by increasing the deposition time or nanoparticles concentration, the film density and the aggregated formation is greatly increased, as shown in Figure 8.
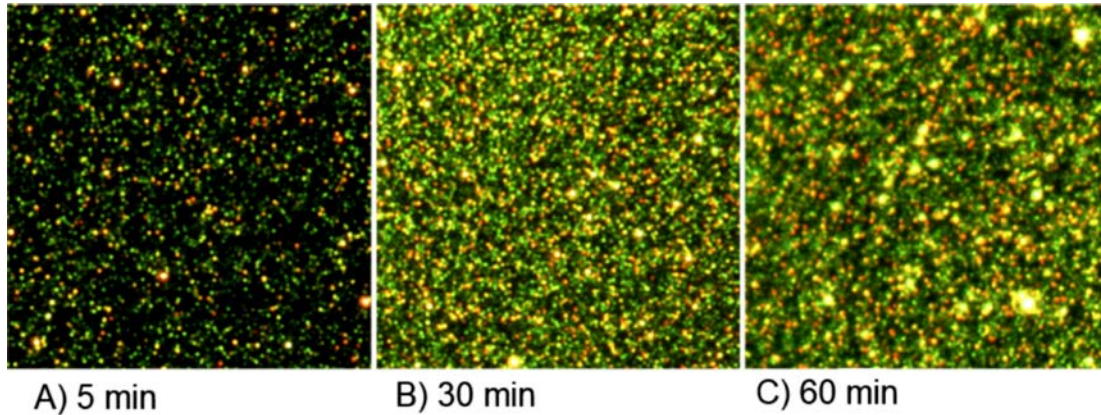
Figure 8. Dark field hyperspectral images of a AuNP film formed with different deposition time of a suspension diluted 25 times: (A) 5 min, (B) 30 min and (C) 60 min.

On the order hand, in the presence of Dz the AuNP colloidal stability is lost, due to the changes at the electric double layer, and the film prepared in APTS glass, at any AuNP concentration and deposition time, is always formed by aggregates. The dark-field hyperspectral exhibit extinction bands around 825 nm, typical of the plasmon coupling excitation in aggregated nanoparticles (see Figure 3). For analytical purposes, the formation of such aggregates is more interesting because of the enhancement of the SERS response due to the occurrence of the so called "hot spots" at the nanoparticles junctions.[18] A typical result is shown in Figure 9. The corresponding SERS spectra were also sensitive to the presence of nickel(II) ions, however the results were rather noisy in comparison with the measurements carried out on filter paper.
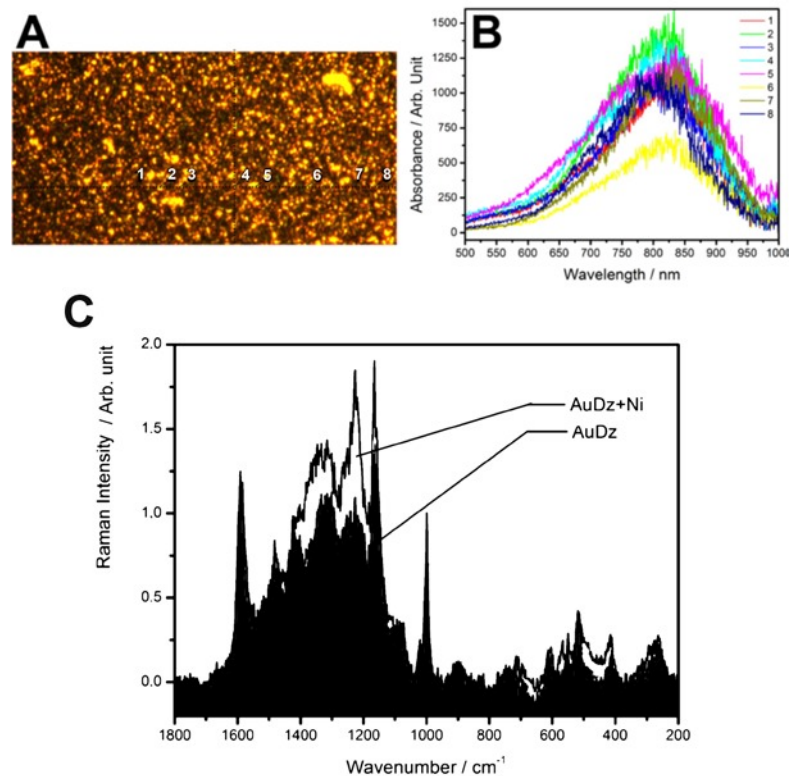

Figure 9. (A) Dark field hyperspectral Image of a Dz-AuNP film and the scattering (B) spectra collected at spots 1-8, and (C) the SERS spectra.

4. CONCLUSION

Hyperspectral dark-field and confocal Raman microscopy can be conveniently employed in the speciation of chemical species, with a very high sensibility, by exploring the SERS effect promoted by the gold nanoparticless. The successfull application to the spot test analysis illustrates de possibility of performing chemical analysis on filter papers, providing an accurate distribution of the chemical species based on the hyperspectral images. Such usefulness can be extended to the analysis and imaging of biological systems, combining the information from the optical and spectral microscopy, and the resonance plasmon effects associated with the gold nanoparticles.

Acknowledgments

REFERENCES

[1]   Vodyanoy, V., Pustovyy, O., Vainrub, A., "High resolution light microscopy of nanoforms," Proc. SPIE 6694, 669413, San Diego, CA (2007).

[2]   Vainrub, A., Pustovyy, O., Vodyanoy, V., "Resolution of 90 nm (λ/5) in an optical transmission microscope with an annular condenser," Opt. Lett. **31**(19), 2855-57 (2006).

[3]   Grasseschi, D., Parussulo, A. L. A., Zamarion, V. M., Guimarães, R. R., Araki, K.., Toma, H. E., "How relevant can the SERS effect in isolated nanoparticles be?," RSC Adv. **3**(46), 24465–72 (2013).

[4]   Grasseschi, D., Parussulo, A. L. A., Zamarion, V. M., Guimarães, R. R., Araki, K.., Toma, H. E., "SERS studies of isolated and agglomerated gold nanoparticles functionalized with a dicarboxybipyridine-trimercaptotriazine-ruthenium dye," J. Raman Spectrosc. **45**(9), 758–63 (2014).

[5]   Grasseschi, D., Lima, F. S., Nakamura, M.., Toma, H. E., "Hyperspectral Dark-Field Microscopy of Gold Nanodisks," Micron **69**, 15–20 (2015).

[6]   Dieing, T., Toporski, J., Hollricher, O., eds., Confocal Raman Microscopy, 1st ed., 279, Springer, Ulm (2010).

[7]   Huila, M. F. G., Lukin, N., Parussulo, A. L. A., Oliveira, P. V., Kyohara, P. K., Araki, K., Toma, H. E., "Unraveling the mysterious role of palladium in Feigl bis(dimethylglyoximate)nickel(II) spot tests by means of confocal Raman microscopy.," Anal. Chem. **84**(7), 3067–69 (2012).

[8]   Paula, S. M., Huila, M. F. G., Araki, K. and Toma, H. E., "Confocal Raman and electronic microscopy studies on the topotactic conversion of calcium carbonate from Pomacea lineate shells into hydroxyapatite bioceramic materials in phosphate media," Micron **41**(8), 983–9, Elsevier Ltd (2010).

[9]   Uchiyama, M. K., Deda, D. K., Rodrigues, S. F. D. P., Drewes, C. C., Bolonheis, S. M., Kiyohara, P. K., Toledo, S. P. De., Colli, W., Araki, K., et al., "In vivo and In vitro Toxicity and Anti-Inflammatory Properties of Gold Nanoparticle Bioconjugates to the Vascular System.," Toxicol. Sci. **142**(2), 497–507 (2014).

[10]   Aroca, R. F., "Plasmon enhanced spectroscopy," Phys. Chem. Chem. Phys. **15**(15), 5355–5363 (2013).

[11]   Eustis, S.., El-Sayed, M. A., "Why gold nanoparticles are more precious than pretty gold: noble metal surface plasmon resonance and its enhancement of the radiative and nonradiative properties of nanocrystals of different shapes.," Chem. Soc. Rev. **35**(3), 209–217 (2006).

[12]   Lombardi, J. R., Birke, R. L., "The theory of surface-enhanced Raman scattering.," J. Chem. Phys. **136**(14), 144704 (2012).

[13]   Turkevich, J., Stevenson, P.., Hillier, J., "A study of the nucleation and growth processes in the synthesis of colloidal gold," Discuss. Faraday **11**, 55–75 (1951).

[14]   Frens, G., "Controlled Nucleation for Regulation of Particle-Size in Monodisperse Gold Suspensions," Nature-Physical Sci. **241**(105), 20–22 (1973).

[15]   Mie, G., "Colloidal solutions," Anallen der Phys. **25**, 377–445 (1908).

[16]   Grasseschi, D., Zamarion, V. M., Araki, K.., Toma, H. E., "Surface Enhanced Raman Scattering Spot Tests: A New Insight on Feigl's Analysis Using Gold Nanoparticles," Anal. Chem. **82**(22), 9146–49, (2010).

[17]   Pemberton, J. E.., Buck, R. P., "Dithizone adsorption at metal electrodes. 4. Voltammetric and surface Raman spectroelectrochemical investigation at a copper electrode," J. Am. Chem. Soc. **104**(15), 4076–84 (1982).

[18]   Ghosh, S. K.., Pal, T., "Interparticle coupling effect on the surface plasmon resonance of gold nanoparticles: from theory to applications.," Chem. Rev. **107**(11), 4797–4862 (2007).

Exploring the metallochromic behavior of pentacyanidoferrates in visual, electronic and Raman spot tests

JORGE S. SHINOHARA, DANIEL GRASSESCHI, SABRINA N. ALMEIDA and HENRIQUE E. TOMA

Instituto de Química, Universidade de São Paulo, Av. Prof. Lineu Prestes, 748, 05508-000 São Paulo, SP, Brazil

How to cite: SHINOHARA JS, GRASSESCHI D, ALMEIDA SN AND TOMA HE. 2019. Exploring the metallochromic behavior of pentacyanidoferrates in visual, electronic and Raman spot tests. An Acad Bras Cienc 91: e20180315. DOI 10.1590/0001-3765201920180315.

Abstract: Pentacyanidoferrate(II) complexes of aromatic N-heterocycles, such as 4-cyanopyridine, exhibit characteristic colors and strong metallochromism associated with the donor-acceptor interactions of the metal ions with the cyanide ligands. In the presence of transition metal ions insoluble polymeric complexes are formed, displaying bright yellow, red, brown and green colors with zinc(II), nickel(II), copper(II) and iron(III) ions, respectively. Such metallochromic response is better observed on filter paper, allowing applications in analytical spot tests. The effects can be explored visually and probed by means of modern instrumental facilities, including spectrophotometric and resonance Raman techniques. In this way, by using the cyanopyridinepentacyanidoferrates, the Prussian Blue test for ferric ions can be extended to the entire row of transition metal elements, providing a new and modern insight of such classical Feigl's spot tests.

Key words: pentacyanidoferrates, Feigl spot tests, Prussian blue, resonance Raman, ring oven.

INTRODUCTION

Colorimetric reagents have been extensively explored in analytical chemistry since the beginning of the last century, after the outstanding work of Fritz Feigl on spot tests (Feigl and Anger 972). Because of their simple use, spot tests became a common practice in Chemistry and Forensics, allowing rapid and practical detection of analytes, including representative, lanthanide and transition metal ions. They are usually performed using spot test plates or filter paper, allowing many interesting variations, for instance, by combining solvent elution and rapid evaporation procedures as in the

so called "ring oven" technique (Riyazuddin 1994, Cortez and Pasquini 2013). Such strategy allows to concentrate the analytes on a paper spot, increasing the sensitivity of the analysis.

On the other hand, the limits of the visual detection of the spot tests can also be extended with the aid of modern instrumental facilities, encompassing for instance, fiber optics spectrophotometry and Raman techniques. Such instrumental detection can be directly applied on spot test plates and filter paper, providing more than just a positive or negative response, allowing to access the chemical nature of the analytes by means of their electronic and vibrational features.

A good example has already been reported in a confocal Raman study of the Feigl spot test

Correspondence to: Henrique Eisi Toma
E-mail: henetoma@iq.usp.br
ORCid: orcid.org/0000-0002-4044-391X

for palladium(II) in the presence of nickel(II) ions, using the dimethylglyoxime (dmgH) reagent (Huila et al. 2012). This spot test was based on the sensitivity of the nickel complex to acids due to the protonation of the dmgH ligand, breaking the macrocyclic structure and leading to the loss of the characteristic red color associated with the square planar configuration of the $[Ni(dmgH)_2]$ complex. On the other hand, palladium(II) ions also react with dimethylglyoxime, yielding a very stable, planar, yellow $[Pd(dmgH)_2]$ complex, which is resistant to acids. Feigl (Feigl 1943) proposed that the presence of palladium(II) ions preserves the red color of the nickel(II) complex from the attack of acids, by forming a protective coating. However, we have shown that the bis(dimethylglyoximate) nickel(II) complex is actually formed by stacking interactions, generating deep red microscopic needles which can be readily observed on the cellulose fibers. This observation indicated that the most accessible sites for protonation are located at the needles end, where the complex is completely exposed. When palladium ions are present in the mixture, they can block the acid attack on the nickel(II) complex by protecting the needle extremities, thus preserving the red color. All these aspects have been clearly demonstrated by confocal Raman spectroscopy, providing a completely new insight on such classical Feigl spot test.

Another interesting case is the classical Prussian blue test, which has been routinely performed for Fe(III) ions, since its discovery in 1704. The Prussian blue complex is composed by Fe(II) and Fe(III) ions bridged by cyanide ligands and has been denoted a "mixed-valence" complex, after Robin (Robin 1961) and Day (Robin and Day 1967). Prussian blue is prototype of a class of compounds exhibiting metal-to-metal, or "intervalence" (IT) transitions. Intervalence transfer bands were extensively investigated in the 1970 - 1980 decades, especially by Taube and coworkers (Ford et al. 1968, Creutz and Taube

1973), establishing important parallelisms between optical and thermal electron transfer. In this area, the related chemistry of pentacyanidoferrate(II)/(III) complexes also exhibited a great boom in the 1970-1990 decades (Toma et al. 1973, 1982, Toma and Creutz 1977, Toma and Malin 1973), because of their rich electronic and intervalence properties.

In this paper we are expanding the spot tests inspired on Prussian Blue chemistry, replacing a cyanide ligand by the 4-cyanopyridine (pyCN) molecule. It has been shown (Toma et al. 1987) that the pyCN ligand forms a strong bond with the $(CN)_5Fe(II)$ moiety by coordinating at the N-pyridine atom, yielding a deep red-orange complex displaying a strong Fe(II)-to-pyCN ($d_\pi \rightarrow p_\pi^*$) charge-transfer transition. In this way, the pyCN ligand is important for introducing a new chromophore group in the complex, allowing to sense the chemical interactions with transition metal ions. In contrast to the $[Fe^{II}(CN)_6]^{4-}$ complex, the $[Fe^{II}(CN)_5(pyCN)]^{3-}$ species form strongly colored complexes with all the transition metal ions in aqueous solution; however, their application on spot tests has never been published before. As an improvement, the use of the ring oven technique was also explored in this work, in order to enhance the colors and improve the detection limit, in association with electronic and resonance Raman spectroscopy.

MATERIALS AND METHODS

$Na_3[Fe(CN)_5NH_3].3H_2O$ was synthesized by reacting $Na_2[Fe(CN)_5NO].2H_2O$ with ammonia, as described in the literature (Toma and Malin 1973, Toma et al.1982). 4-cyanopyridine (pyCN), $FeSO_4.7H_2O$, $CuSO_4.5H_2O$, $CoSO_4.7H_2O$, $MnSO_4.7H_2O$, $ZnSO_4.7H_2O$, $NiSO_4.7H_2O$, are commercially available (Sigma-Aldrich, Merck) as analytical grade reagents and were used as supplied. The $[Fe(CN)_5(pyCN)]^{3-}$ complex was prepared by dissolving $Na_3[Fe(CN)_5NH_3].3H_2O$ in an aqueous solution of pyCN (20 mM) in order

to yield a 10 mM stock solution. An excess of pyCN has been employed to ensure the complete substitution of the NH_3 ligand from the starting aminopentacyanidoferrate(II) complex (Toma and Malin 1973).

Whatman chromatography paper was employed for the spot test analysis, but conventional filter papers can also be used for routine or qualitative purposes. The metal ions (10 mmol L^{-1}) were deposited on the paper using a micrometric syringe. After applying the pentacyanidoferrate reagent, the paper was copiously washed with water and allowed to dry at room temperature. In the case of the Fe^{2+} test, an equivalent amount of ascorbic acid was also added before the reaction with the pentacyanidoferrate complex, in order to postpone the air oxidation of the complex. Nevertheless, the paper was kept under a flow of nitrogen, and for long term experiments it should be stored in the absence of air.

Instead of the classical ring oven technique, the samples were applied by depositing on the filter paper, successive amounts (50 nL) of the metal ion solutions, using a chromatographic syringe. The paper was previously placed on a metal ring over a heating plate, keeping a constant temperature (e. g., 70 ºC) in order to control the evaporation rate and the spot size.

Optical reflectance spectra of the filter paper spots were recorded on a fiber optics Specfield spectrophotometer, in the 350-1600 nm region. The corresponding Raman spectra were obtained using an Alpha 300R WITec confocal Raman microscope, at 488 and 532 excitation wavelengths, by applying a minimum laser power in association with a high sensitive EMS detector, in order to minimize the spot damage.

RESULTS AND DISCUSSION

VISUAL SPOT TESTS

One of the most intriguing aspects observed in this work is the remarkable color changes produced by the $[Fe(CN)_5pyCN]^{3-}$ complex when applied to the spot test analysis of transition metal ions, as shown in Fig. 1.

The reactions carried out on the filter paper proceed according to equation (1), yielding insoluble Prussian blue like complexes of general composition $M_x[FeCN)_5pyCN]_y$, displaying red (Mn^{2+}), brick-red (Co^{2+}), red-violet (Ni^{2+}), dark magenta (Fe^{2+}), brown (Cu^{2+}), green (Fe^{3+}) and bright yellow (Zn^{2+}) colors.

$$xM^{n+} + y[Fe(CN)_5pyCN]^{3-} \rightarrow M_x[FeCN)_5pyCN]_y \,(1)$$
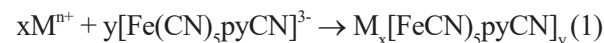
The spot tests can be performed by applying the $[Fe(CN)_5pyCN]^{3-}$ complex on the paper containing the elements, and the final colors revealed after washing copiously with water. Such colors are very stable, and some curious amateur paints have been made to illustrate the spot test design on filter paper, as shown in Fig. 2. Such paints were performed by applying diluted solutions of the several metal
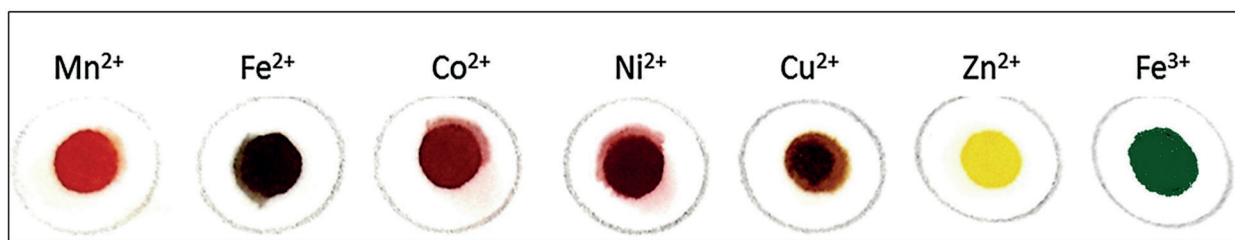
Figure 1 - Metallochromic response of the $[Fe(CN)_5pyCN]^{3-}$ complex applied on filter paper containing the metal ions (bright yellow = Zn^{2+}, red = Mn^{2+}, brick-red = Co^{2+}, red-violet = Ni^{2+}, dark magenta = Fe^{2+}, brown = Cu^{2+}, green = Fe^{3+}), after washing with water.
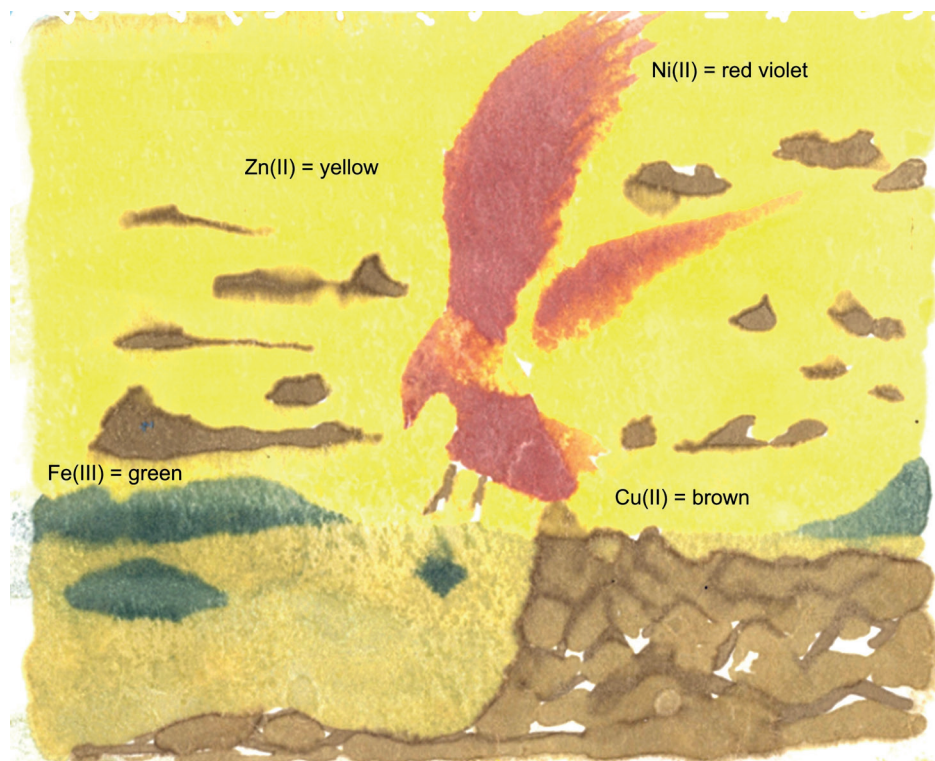
Figure 2 - Decorative spot test paint with $[Fe(CN)_5pyCN]^{3-}$ applied to transition metal ions on filter paper.

ions, with a paintbrush, and allowing to dry. The colors revealed on the white paper, after applying the $[Fe(CN)_5pyCN]^{3-}$ reagent, resemble a typical performance with magic ink, e. g. in classroom demonstrations.

The substitution of a cyanide ligand in the $[Fe(CN)_6]^{4-}$ complex introduces a new Fe^{II}-pyCN chromophore group displaying a strong metal-ligand charge-transfer transition at 480 nm. However, the colors of the pentacyanidoferrates are quite unusual because of the presence of the five cyanide ligands which can interact with the surrounding species, such as the solvent molecules, leading to strong solvatochromic effects (Toma and Takasugi 1983, 1989), or with transition metal ions, producing unusual metallochromic effects.

The binding of the metal ions to the cyanide ligands in the $[Fe(CN)_6]^{4-}$ complex has been well characterized in the Prussian blue complex (Ludi et al.1969), exhibiting the $Fe_4[Fe(CN)_6]_3$ composition

with a (low spin)Fe^{II} – CN - Fe^{III}(high spin) configuration. The cyanide ligands form extended bridged cubic structures, generating internal vacancies for accomodating solvent molecules and eventually, alkaline ions such as Cs^+. For this reason, it was already employed in the treatment of radioactive Cs^+ contamination (Dechojarassri et al. 2017) in the terrible nuclear tragedies occurred in 1987 in Goiania city (Brazil), and in 2011, in Fukushima (Japan)(Parajuli et al. 2016).

In the case of the $[Fe(CN)_5pyCN]^{3-}$ analogue, in addition to the extended bridged structures promoted by the five cyanide ligands, a new chromophore group, Fe-pyCN is introduced, exhibiting a characteristic Fe(II)→pyCN charge-transfer band at 480 nm.

The visual detection limit in the spot test analysis depends upon the sample distribution on the filter paper, and also on the molar absorptivity of the colorimetric reagent employed. Although

the optical absorption is not particularly large for the pentacyanidoferrates ($\varepsilon = 10^3 - 10^4$ mol L^{-1} cm^{-1} (Toma and Malin 1973)), the formation of insoluble complexes on the cellulose fibers improves the contrast and the visual detection, yielding a positive response even at very diluted conditions, e. g. 10^{-5} mol L^{-1} (~1 ppm). The detection limit can be further improved by using the ring oven technique illustrated in Fig. 3. The technique consists in applying the sample on a filter paper and evaporating, sequentially, in order the concentrate the analyte on the spot, proportionally to the number of repetition steps. In this case, the use of chromatography syringes allows to precisely controlling the concentration and spot size. In this way, it is possible to enhance the color and to extend the visual detection below the ppm range.

ELECTRONIC DETECTION OF THE SPOT TESTS AND CHARACTERIZATION OF THE SPECTRAL BANDS

The electronic spectra recorded for the several spot tests shown in Figure 1, can be seen in Fig. 4. A fiber optics spectrophotometer has been employed, allowing *in situ* measurements for discriminating the electronic bands in the spots.

The [Fe(CN)$_5$(pyCN)]$^{3-}$ chromophore is really strategic since it allows to probe the interaction of the complex with metal ions, through the perturbation of the Fe^{II} d$_\pi$ orbitals *via* metalation of the isocyanide and pyCN ligands. A didactic diagram can be seen in Fig. 5, showing how the interaction of the metal ions with the isocyanide and pyCN groups perturbs the electronic levels of the [Fe(CN)$_5$(pyCN)] core.

Accordingly, the hypsochromic shift of the Fe→pyCN MLCT band observed in the case of the Zn^{2+} ions is consistent with the electron withdrawing effects after their N-binding to the cyanide ligands, enhancing the backbonding interactions with the low spin Fe(II) center. The consequent stabilization of the Fe(II) d$_\pi$ orbitals (Fig. 5b) promotes a hypsochromic shift of the MLCT band, explaing the bright yellow color of the Zn^{2+} complex.

In the case of the Ni^{2+} ions, a bathochromic shift of the MLCT band is observed, and such effect is presumably related to their smaller electron withdrawing influence on the cyanide ligands, as compared with the Zn^{2+} ions. In this way, the major changes should be associated with the stabilization of the pyCN ligand orbitals, as illustrated in Fig. 5c.

The remaining metal ions show an intermediate behavior in relation to the Zn^{2+} and Ni^{2+} ions.
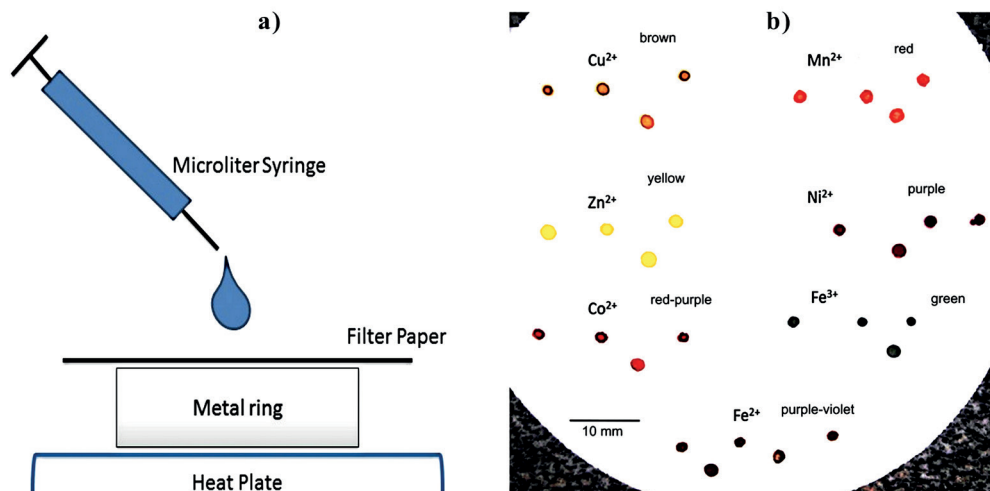
Figure 3 - Improving the detection limit by means of the ring oven technique (**a**), with the sample concentrated on a single spot after repetitive applications (**b**).
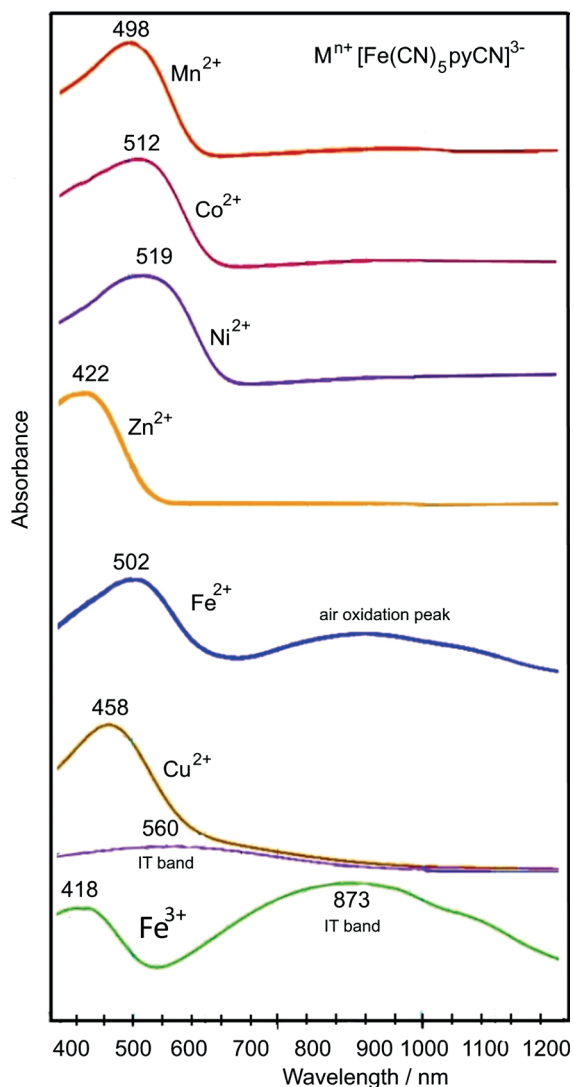
Figure 4 - Fiber-optics reflectance spectra of $M_x[Fe(CN)_5(pyCN)]_y$ generated directly on the filter paper spots

In the case of Cu^{2+} and Fe^{3+} ions, a new band is observed in the electronic spectra, corresponding to intervalence transfer (IT) transitions, also observed in the related Prussian blue complexes. Such IT bands can be explained by the molecular orbital scheme in Fig. 6.

In the case of the Cu^{2+} complex, an IT band can be located at 560 nm, as a shoulder in the corresponding MLCT band in the visible. This band is weak, since it involves a symmetry forbidden $Fe(d_\pi) \rightarrow Cu(d_\sigma)$ transition (Toma 1976). In the

case of the Fe^{3+} complex, a symmetry allowed $Fe^{II}(d_\pi) \rightarrow Fe^{III}(d\pi)$ transition is observed at 873 nm, generating a deep green color, while the expected $Fe^{II}(d_\pi) \rightarrow Fe^{III}(d_\sigma)$ symmetry forbidden transition is masked by the MLCT band around 418 nm.

RESONANCE RAMAN MONITORING OF THE SPOT TESTS

In order to improve the analysis, the resonance Raman technique has also been applied to the spot tests. All the metal ions exhibited strong resonance Raman enhancement on the filter paper, leading to very similar spectra associated with the $Fe^{II}(CN)_5$ and pyCN moieties interacting with the transition metal ions, as shown in Fig. 7.

The resonance Raman spectra exhibited characteristic peaks in the 2235-2245 cm^{-1} interval, associated with the $\nu(CN)$ stretching vibration of the coordinated pyCN ligand. Other typical peaks occur at 2140-2145 cm^{-1} corresponding to the $\nu_{a1}(CN)$ vibrations of the $[Fe^{II}(CN)_5]^{3-}$ group (Griffith and Turner 1970). The major peak is accompanied by a weak shoulder around 2060-2080 cm^{-1} corresponding to a Raman inactive $\nu(CN)$ vibration. The $\nu(CN)$ stretching vibrations of the $[Fe^{II}(CN)_5]^{3-}$ groups exhibit a general increase in the vibrational frequencies from Mn^{2+} to Zn^{2+} ions (Fig. 8), reflecting with the local electron withdrawing effects exerted by the metal ions.

In addition to the $\nu(CN)$ bands, the Raman spectra exhibited sharp peaks around 1600, 1240, 1210, 1020 cm^{-1} corresponding to the $\nu(C-C)$, $\nu(X-sens)$, $\beta(CH)$, and $\nu(ring)$ vibrations of the pyCN ligand, as well as, less intense peaks around 580 and 500 cm^{-1} associated with $\delta(FeCN)$ and $\nu(X-sens)$ vibrations. The (X-sens) notation refers to vibrational peaks of the py-X ligand which are very sensitive to the nature of the X group (Greeen and Harrison 1977).

In this way, within the spectral error interval ($\pm$ 2 cm^{-1}), vibrational peaks at 2248, 2155 and 1025 cm^{-1} would be characteristic of Zn^{2+}, while vibrational peaks at 2242, 2144 and 1018 cm^{-1} would
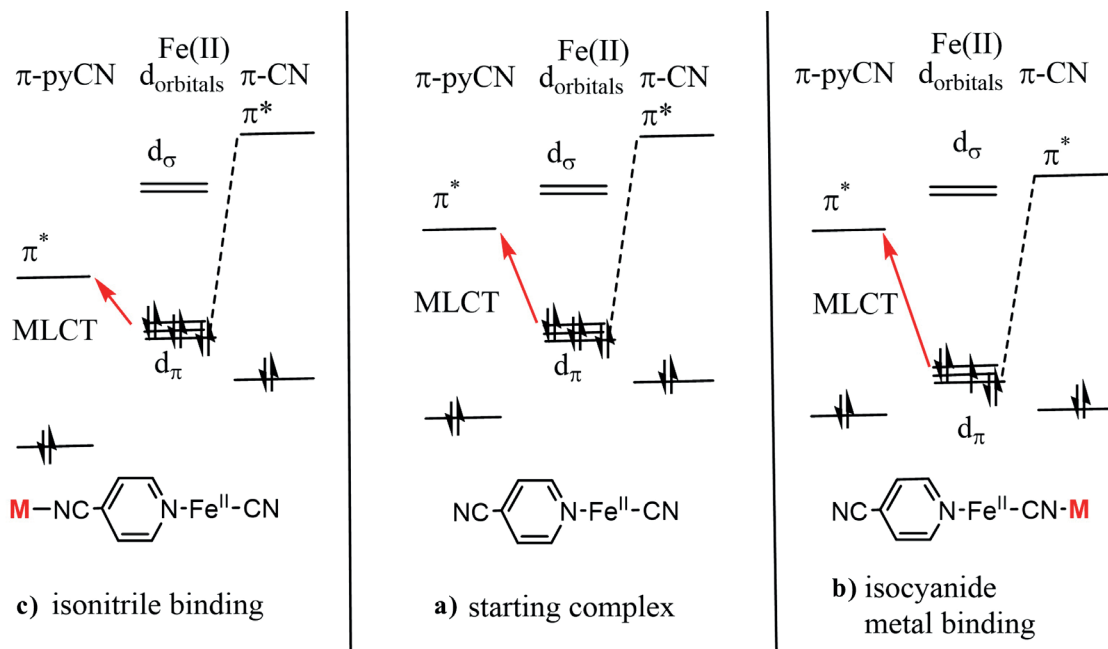
Figure 5 - (**a**) In the center, it is shown the orbital diagram of the $[Fe(CN)_5(pyCN)]^{3-}$ complex; (**b**) the binding of the metal ions to the cyanide ligand enhances the backbonding interaction from the iron(II) core, stabilizing the Fe(II) d_π orbitals and increasing the Fe-to-pyCN charge-transfer energy; (**c**) the binding of the metal ions to the pyCN ligand improves its π-acceptor properties, decreasing the energy of the corresponding MLCT band.
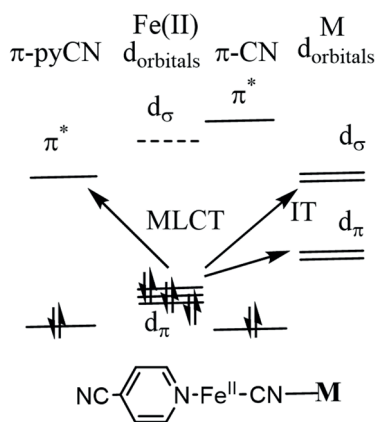

Figure 6 - Molecular orbital diagram illustrating the metal-to-ligand charge-transfer transition (MLCT) and the intervalence transfer transitions (IT).

correspond to Ni^{2+}, and at 2240, 2118 and 1020 cm^{-1} would be indicative of Mn^{2+}. It is also possible to monitor the samples using two different lasers, e.g. at 488 and 532 nm, in order to discriminate the relative resonance Raman enhancement factors associated with each specific chromophore. This procedure, however, is more elaborated and requires a careful design for obtaining comparative results.

Finally, it should be mentioned that the confocal Raman microscopy allows to monitor the spot tests directly on the cellulose fibers, at a microscopic level, generating a visual metal ion distribution by means of their hyperspectral image, as illustrated for the Ni^{2+} ions in Fig. 9. In this case, the image generated from the Raman spectra of the $Ni_3[Fe(CN)_5pyCN]_2$ complex (Fig. 9b) reveals a homogeneous distribution of the complex over the cellulose fibers, practically reproducing the original optical image shown in Fig. 9a. A further gain of sensitivity can also be obtained using confocal Raman techniques, by accessing the microscopic domains of the spot tests.

CONCLUSIONS

By exploring the metallochromic effects, the $[Fe(CN)_5pyCN]^{3-}$ complex can be suitably employed in spot test analysis for transition metal ions, displaying remarkable color changes and resonance Raman signals. In special, the bright yellow color
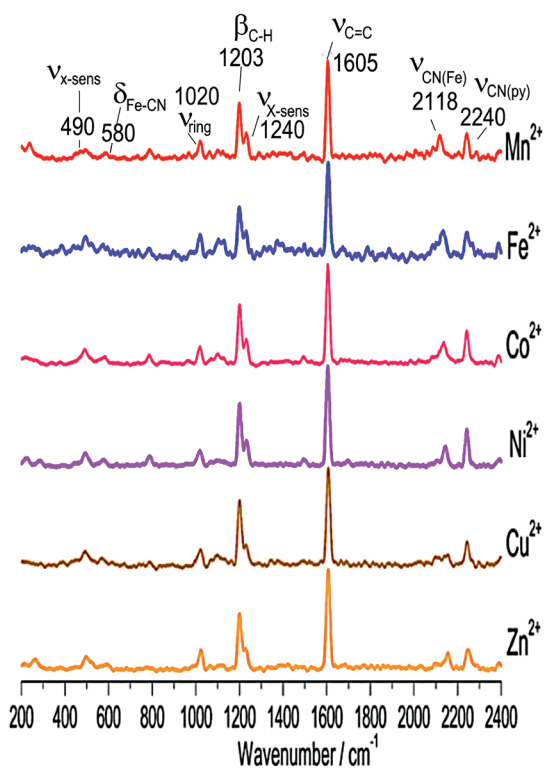
Figure 7 - Resonance Raman spectra of the $M_x[Fe(CN)_5(pyCN)]_y$ complexes on the filter paper spots containing Mn^{2+}, Fe^{2+}, Co^{2+}, Ni^{2+}, Cu^{2+} and Zn^{2+} ions.
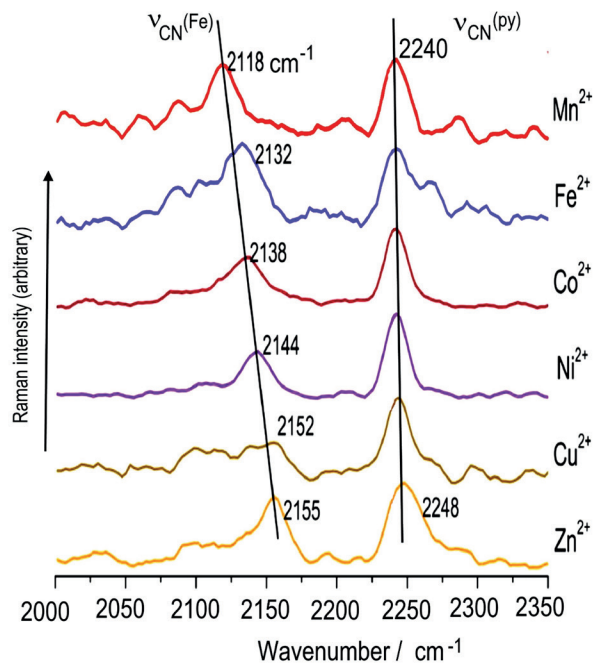
Figure 8 - Variation of the M-N≡C-Fe(II) stretching frequencies as a function of the metal ion.
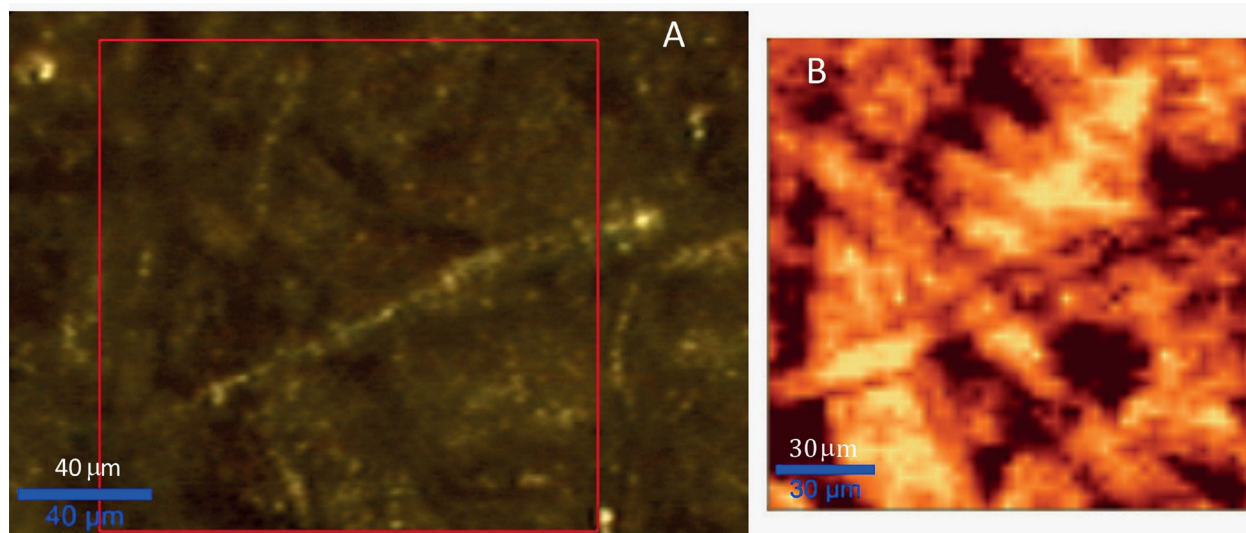
Figure 9 - (**a**) Optical microscopy image of the $Ni_3[Fe(CN)_5(pyCN)]_2$ complex on the cellulose fibers in the spot test analysis, (**b**) hyperspectral image generated by confocal Raman spectroscopy, showing the distribution of the complex on the fibers.

produced by Zn^{2+} was really surprising, providing a very useful test for this element, since most zinc complexes do not display electronic bands in the visible. The use of ring oven techniques in association with fiber optics electronic spectroscopy and confocal Raman techniques allowed to enhance the sensitivity by more than three orders of magnitude. The proposed tests expanded the classical Prussian blue test for iron(III) ions to the whole series of transition metal ions, and represents an important contribution to the Feigl's spot tests in chemistry and forensic analysis .

ACKNOWLEDGMENTS

AUTHOR CONTRIBUTIONS

Jorge S. Shinohara performed the final spot tests, Raman spectra and microscopy, Daniel Grasseschi contributed to the Confocal Raman microscopy, Sabrina N. Almeida started the initial tests and spectrophotometric assays, Henrique E. Toma was involved in all the steps of this work.

REFERENCES

CORTEZ J AND PASQUINI C 2013. Ring-Oven Based Preconcentration Technique for Microanalysis: Simultaneous Determination of Na, Fe, and Cu in Fuel Ethanol by Laser Induced Breakdown Spectroscopy. Anal Chem 85: 1547-1554.

CREUTZ C AND TAUBE H 1973. Binuclear complexes of ruthenium ammines. J Am Chem Soc 95: 1086-1094.

DECHOJARASSRI D, ASAINA S, OMOTE S, NISHIDA K, FURUIKE T AND TAMURA H 2017. Adsorption and desorption behaviors of cesium on rayon fibers coated with chitosan immobilized with Prussian blue. Int J Bio Macromol 104: 1509-1516.

FEIGL F 1943. Spot reaction experiments. Part IV: Protective layer effects / Part V: Solvent effects. J Chem Ed 20: 298.

FEIGL F AND ANGER V 1972. Spot tests in inorganic analysis, 6th ed., Elsevier, Amsterdam.

FORD P, RUDD DFP, GAUNDER R AND TAUBE H 1968. Synthesis and properties of pentaamminepyridineruthenium(II) and related complexes of aromatic N-heterocycles. J Am Chem Soc 90: 1187-1193.

GREEEN JHS AND HARRISON DJ 1977. Vibrational spectra of cyano-pyridines, formyl-pyridines and halogeno-pyridines. Spectrochimica Acta Part A: Mol and Biomol Spectr 33: 75-79.

GRIFFITH WP AND TURNER GT 1970. Raman spectra and vibrational assignments of hexacyano-complexes. J Chem Soc - A - Inorg Phys Theor 858-864.

HUILA MFG, LUKIN N, PARUSSULO ALA, OLIVEIRA PV, KYOHARA PK, ARAKI K AND TOMA HE 2012. Unraveling the mysterious role of palladium in Feigl bis(dimethylglyoximate)nickel(II) spot tests by means of confocal Raman microscopy. Anal Chem 84: 3067-3069

LUDI A, GUDEL HU AND HUGI R 1969. Structure of Prussian Blue. Chimia 23: 194-199.

PARAJULI D ET AL. 2016. Application of Prussian blue nanoparticles for the radioactive Cs decontamination in Fukushima region. J Env Radio 151: 233-237.

RIYAZUDDIN P 1994. A Simple Ring Oven for Microanalysis. J Chem Ed 71: 606-609.

ROBIN MB 1961. The color and electronic configurations of Prussian blue. Spectrochim Acta 17: 1095.

ROBIN MB AND DAY P 1967. Mixed Valence-Chemistry A Survey and Classification. Adv Inorg Chem Radiochem 10: 247-422.

TOMA HE 1976. Intervalence-electron transfer spectra of several iron(III) and copper(II) pentacyanoferrate(II) complexes. J Inorg Nuclear Chem 38: 431-434.

TOMA HE, BATISTA AA AND GRAY HB 1982. Pentacyanoferrate(II) complexes of aminoacids. J Am Chem Soc 104: 7509-7515.

TOMA HE, CARTER JM AND SANTOS PS 1987. Synthesis, electronic spectdra and resonance Raman studies of a new series of cyanoiron pigments. J Chem Res - M: 226-238.

TOMA HE AND CREUTZ C 1977. Pentacyanoferrate(II) complexes - evaluation of their formal potentials and mechanism of quenching of (2,2'-bipyridine) Ruthenium(II) luminescence. Inorg Chem 16: 545-550.

TOMA HE AND MALIN JM 1973. Properties and reactivity of some pentacyanoferrate(II) complexoes of aromatic N-heterocycles. Inorg Chem 12: 1039-1045.

TOMA HE, MALIN JM AND GIESBRECHT E 1973. Ion pentacyano (dimethylsulfoxide)ferrate(II) - Synthesis, characterization and substitution kinetics in aqueous solution. Inorg Chem 12: 2084-2089.

TOMA HE AND TAKASUGI MS. 1989. Preferential solvation effects in the electochemistry and charge-transfer spectra of cyanoiron(II) complexes. J Sol Chem 18: 941-945.

TOMA HE AND TAKASUGI MS 1983. Spectroscopic Studies of Preferential and Asymmetric Solvation in Substituted Cyanoiron(II) Complexes. J Sol Chem 12: 547-561.

Artigo

RAMAN STUDIES OF BIS(PHENYLTERPYRAZINE)IRON(II) AND SUPRAMOLECULAR SPECIES WITH PENTACYANIDOFERRATE(II) IONS

Ana P. Mangoni[a], Bruno B. N. S. Brandão[a], Jorge S. Shinohara[a], Alceu T. Silveira[a], Marcelo Nakamura[a] and Henrique E. Toma[a],*,[ID]

[a]Instituto de Química, Universidade de São Paulo, 05508-000 São Paulo – SP, Brasil

The chemistry and spectroscopy of the iron(II) phenylterpyrazine complex, $[Fe(phtpz)_2]^{2+}$, were investigated in comparison with the analogous phenylterpyridine species, $Fe(phtpy)_2]^{2+}$, and the results indicated a strong electronic delocalization on the Fe(II) terimine chromophore encompassing the lateral pyrazyl groups. The delocalized nature of the molecular orbitals involved in the electronic excitation precluded a direct assignment of the pyridine and pyrazine vibrations in the complex. However, the capability of the terpyrazine complex to bind transition metal ions, such as the $[Fe(CN)_5]^{3-}$ species, allowed to generate pentanuclear complexes displaying characteristic charge-transfer and resonance Raman spectra, revealing the pyrazine vibrations in the complex. The $[Fe(CN)_5]^{3-}$ containing species also yielded polymeric compounds in presence of transition metal ions, exhibiting intervalence transfer bands and chemical similarities with the Prussian Blue complex.

Keywords: Resonance Raman; iron terimines; iron terpyrazines; pentacyanidoferrates; Prussian Blue.

INTRODUCTION

Iron(II) terpyridine complexes are classical examples of coordination compounds exhibiting a typical (terimine)iron(II) chromophore in a low spin configuration.[1-3] The complexes have been extensively employed in analytical chemistry, coordination polymers[4] and devices[5] because of their strong red-violet colors associated with metal-to-ligand charge-transfer transitions in the visible region. However, the analogous iron(II) terpyrazine complexes remain poorly understood, and according to the best of our knowledge, they have never been investigated before from the point of view of their electronic, Raman and supramolecular properties in aqueous solution. As a matter of fact, the terpyrazine ligands exhibit a central pyridine moiety attached to two pyrazine groups, which possess strong π-acceptor characteristics and are also able to bind metal ions by acting as bridging ligands. These aspects depart from the typical behavior of the iron(II) terpyridine complexes. Since their electronic and vibrational spectra are expected to be strongly influenced by the π-acceptor properties of the pyrazine group, a detailed investigation is required for improving the understanding of the chemistry of the iron(II) terimine complexes, and their possible application in photo-induced molecular pathways.[6]

In this paper, the chemistry and spectroscopy of the bis(phenylterpyrazine)iron(II) complex, $[Fe(phtpz)_2]^{2+}$, have been investigated in comparison with the related bis(phenylterpyridine) iron(II), $[Fe(phtpy)_2]^{2+}$, analogue[7] (Figure 1).

The four pyrazine moieties are very accessible to the interaction with π-donor complexes such as the pentacyanidoferrate(II) ions, and can generate pentanuclear complexes displaying a symmetric supramolecular structure. Formation of such species perturbs the pyrazine moieties and this aspect allows to discriminate the aromatic pyrazine vibrations from the pyridine ones, located in the same spectral region of the Raman spectra. This is actually a critical point in the analysis of the vibrational spectra of the metal-terimine complexes from the experimental point of view. On the other hand, the pentanuclear species can react with transition metal ions (M),

generating novel supramolecular structures containing iron(II)-cyanide-M bonds, analogous to the Prussian Blue complex. Such species are quite novel, and their chemistry is reported in this paper.

EXPERIMENTAL SECTION

Materials

The $(NH_4)_2Fe(SO_4)_2.6H_2O$ (Mohr's salt) and the organic reagents benzaldehyde, 2-acetylpyridine and 2-acetylpyrazine were obtained from Sigma/Aldrich. All other reagents were of analytical grade and used as supplied.

Synthesis of the phenylterpyridine and phenylterpyrazine ligands

The 4'-phenyl-2,2':6',2"terpyridine (phtpy) and 4'-phenyl-2,2':6:2'terpyrazine (phtpz) ligands were synthesized according to the procedure reported by Wang and Hanan:[8] 1.0 mL of benzaldehyde (10 mmol) was added to 30 mL of ethanol solution containing 1.5 g KOH. Then 2.3 mL of acetylpyridine (20 mmol) or acetylpyrazine (20 mmol) was added, followed by 24 mL of NH_4OH (18 mol L^{-1}). The mixture was kept under stirring for 6 h at room temperature. The white precipitate was collected on a filter, and washed with water until obtaining a neutral pH. The phtpy ligand was recrystallized from an ethanol/water mixture (1:1) and the phtpz species recrystallized from chloroform/ethanol (1:1). They were kept dried under vacuum in a desiccator. Anal: $C_{21}H_{15}N_3$ (MM 309.36 g mol^{-1}) CHN exp (calc)%: 80.27 (81.53); 4.72 (4.89); 13.21(13.58). ESI-MS (m/z) exp(calc) [phtpy-H]$^+$: 310.1 (310.3); and $C_{19}H_{13}N_5$ (MM = 311.17 g mol^{-1}), CHN exp(cal)% 74.47(73:30); 4.22(4.21); 22.30(22.49). ESI-MS (m/z) exp(calc) [phtpz-H]$^+$: 312.12(312.17).

Synthesis of the $[Fe(phtpy)_2]^{2+}$ and $Fe(phtpz)_2]^{2+}$ complexes

The $[Fe(phtpy)_2](PF_6)_2$ and $[Fe(phtpz)_2](PF_6)_2$ complexes were prepared by dissolving 80 mg of $(NH_4)_2Fe(SO_4)_2.6H_2O$ (0.2 mmol) in 30 mL of water, followed by the addition of 130 mg of the phtpy or phtpz ligands (0.4 mmol) dissolved in 4 mL trifluoroethanol. The

*e-mail: henetoma@iq.usp.br

65

Vol. 42, No. 9   Raman studies of bis(phenylterpyrazine)iron(II) and supramolecular species with pentacyanidoferrate(II) ions   1021

$[Fe(phtpy)_2]^{2+}$
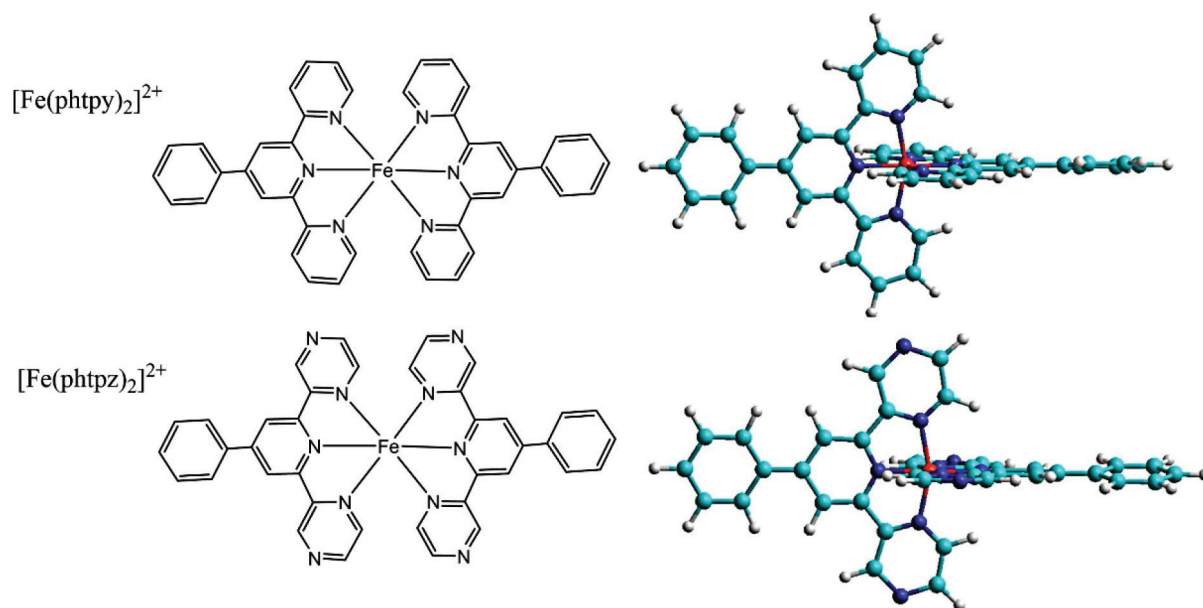
$[Fe(phtpz)_2]^{2+}$

Figure 1. *Structural representation of the [Fe(phtpy)₂]²⁺ and [Fe(phtpz)₂]²⁺ complexes*

mixture was stirred for 3 h under a nitrogen atmosphere. Then, 1 mL of a saturated NH_4PF_6 solution was added to precipitate the complexes, which were collected on a filter, washed with water and kept under vacuum, in a desiccator. $C_{42}H_{30}N_6P_2F_{12}Fe$ (MM 964.12 g mol⁻¹), CHN exp(cal)% 51.47(52.30); 3.22(3.14); 8.56(8.71), $C_{38}H_{26}N_{10}P_2F_{12}Fe$ (MM 968.1 g mol⁻¹), CHN exp(cal)%: 46.49(47.13); 2.96 (2.71); 14.49(14.46).

For the experiments performed in aqueous solution, the $[Fe(phtpy)_2]Cl_2$ and $[Fe(phtpz)_2]Cl_2$ complexes were employed because of the poor solubility of the hexafluorophosphate analogues. They can be obtained from the corresponding PF_6^- compounds by dissolving into a minimum amount of acetonitrile and adding LiCl in excess. Under this condition, the chloride salts which are poorly soluble in the organic medium, precipitate as a fine powder material. The solids were isolated by centrifugation at 5000 rpm, washed with small amounts of acetone and kept in the desiccator.

Generation of polynuclear pentacyanidoferrate(II) complexes with the [Fe(phtpz)₂]²⁺ core

In general, the substituted pentacyanidoferrate(II) complexes which are extremely soluble in water, generate untreatable oils when processed with organic solvents such as ethanol, acetone, or acetonitrile. However their chemistry in solution is quite well behaved and the complexes have been extensively investigated in this way.[9-11] An important aspect to mention is the monodentate binding characteristics of the $[Fe(CN)_5]^{3-}$ moiety, which leads to complexes of general formula $[Fe(CN)_5L]^{3-}$ with aromatic N-heterocyclic ligands. For this reason, in this work the pentacyanidoferrate(II) complexes have been generated and studied in aqueous solution. Isolation of the solid forms, e. g. by drastic evaporation, leads to impure products, since of the precursor oily material can carry many impurities and are susceptible to contamination with coordination polymers formed in the drying process.

Generation of Prussian Blue derivatives of the metallated polynuclear pentacyanidoferrate(II) complexes containing the [Fe(phtpz)₂]²⁺ core

The pentanuclear pentacyanidoferrate(II) complexes precipitate in the presence of transition metals ions, such as Mn^{2+}, Co^{2+}, Ni^{2+},

Cu^{2+}, Zn^{2+} and Fe^{3+}, generating colloidal solutions as observed for the analogous Prussian Blue complexes.[12] The colloidal suspensions can be broken by centrifugation at 5000 rpm, and in this way the solids can be separated and isolated after washing many times with water, in order to remove the contaminant species present in solution.

Electronic spectra

The electronic spectra of the complexes were obtained using a Hewlett-Packard, model HP-8453-A diode array spectrophotometer in the 200 – 1100 nm range. For the solid samples, the spectra were obtained by suspending the particles in polyvinyl alcohol (PVA) gel and allowing to dry, in order to generate thin, transparent films, suitable for optical monitoring.

Resonance Raman spectra

The Raman spectra were recorded on a WITec alpha 300-R confocal Raman microscope equipped with 488, 532 and 633 nm lasers. The samples were prepared in aqueous solution, or as PVA films. The confocal Raman measurements were monitored with a laser spot area of 1 μm², using 20x lens with 0.40 numerical aperture, 600 grating, and CCD detector of 1600 x 200 pixels. The laser wavelength, power and integration time were 488 nm, 0.06 W cm⁻², 60 s; 532 nm, 0.1 mW cm⁻², 20 s; and 633 nm, 0.08 W cm⁻², 60 s, respectively.

Theoretical calculations

DFT calculations of the geometry and vibrational frequencies for the $[Fe(phtpy)_2]^{2+}$ complex were carried out using Gaussian-09, with the functional MH06-HF and cc-pvtz basis. Simple geometry optimization in this case demanded 9 days of computational work using the laboratory workstation, comprising an Octacore Intel Processor i7-3770 CPU @ 3.40GHz, DDR3 2666 MHz, 16 GB and SSD 240 GB. The molecular structure exhibited orthogonal terpyridine rings, with the phenyl rings adopting 40.3° orientation in relation to the central pyridine ring. Due to the molecular complexity of the complexes and their supramolecular species, DFT and TDTFD theoretical calculations were considered exceedingly

time demanding for the purposes of this work. For convenience, the ZINDO-S semiempirical method from the Hyperchem 8.05 computational package was here employed.[13] As demonstrated by Gorelski and Lever[14] and according to our own experience, there is a reasonable convergence between the two methods. However, the last one requires only few seconds and can be carried out simultaneously with the spectroscopic measurements, thus allowing the planning and evaluation of the experiments in real time. In the theoretical calculations, the atomic dipoles were initially used to start the MM+ geometry optimization, and then replaced by the atomic charges obtained from the ZINDO-S method, with a convergence limit of about 10-5 kcal Å^{-1} mol^{-1}. The electronic distribution was generated from single CI excitations in an active space involving 20 frontier molecular orbitals (10 highest occupied and 10 lowest unoccupied MOs). The semiempirical optimized geometry reproduced an orthogonal orientation of the terpyridine or terpyrazine ligands (Figure 1) very similar to that obtained by DFT; but yielding an angle of 9.0° for the phenyl ring with respect to the central pyridine ring, which is much closer to the crystallographic data for the free ligand, e.g. 10.9°.[15] After the MM+/ZINDO-S geometry optimization, the final electronic spectra were obtained, and the molecular orbitals plotted as 2D energy contours. Such plots were expected to indicate the atomic bonds involved in the resonance Raman spectra, thus facilitating the interpretation of the observed peaks.

RESULTS AND DISCUSSION

The [Fe(phtpy)$_2$]$^{2+}$ and [Fe(phtpz)$_2$]$^{2+}$ complexes exhibit a typical low spin configuration, with a peculiar symmetry, where the ligands adopt a local C$_{2v}$ point group, but yielding a global D$_{2d}$ symmetry because of their orthogonal configuration, as illustrated in Figure 1. It

should be noted that the four pyrazine ligands are located at orthogonal positions, and are available for interacting with metal complexes, allowing the generation of polynuclear coordination compounds.

Electronic Spectra of the [Fe(phtpy)$_2$]$^{2+}$ and [Fe(phtpz)$_2$]$^{2+}$ complexes

The electronic spectra of the [Fe(phtpy)$_2$]$^{2+}$ and [Fe(phtpz)$_2$]$^{2+}$ complexes consist of two sets of bands: one set below 400 nm, associated with internal π→π* transitions in the organic ligand, and another set in the range of 400-700 nm, which is characteristic of the Fe(II)-terimine chromophore, being ascribed to iron(II)-phtpy or iron(II)-phtpz charge-transfer (CT) transitions (Figure 2).

DFT calculations of the structure and vibrational spectra of the iron(II)-bipyridine complexes have already been reported[16] in the literature, but not for the terimine analogues. In general, such calculations do not include the resonance Raman effect[17,18] which requires more specific considerations on the electronic states involved in the molecules, and depend on the Raman exciting wavelengths. As a matter of act, resonance Raman is chromophore selective and this is a very important feature which has been explored in a number of applications, especially in biological systems.[19] In order to discriminate the electronic levels involved in the resonance Raman effect, the use of semiempirical methods, such as ZINDO/S can be very convenient, taking into account that the large molecular complexity would require very long computational times, using for instance, TDDFT or multiconfigurational methods.

The observed visible bands can be deconvoluted into four bands as shown in the Figure 2. ZINDO/S theoretical calculations provided an approximate simulation of such bands, allowing to access the electronic distribution of the relevant HOMO and LUMO
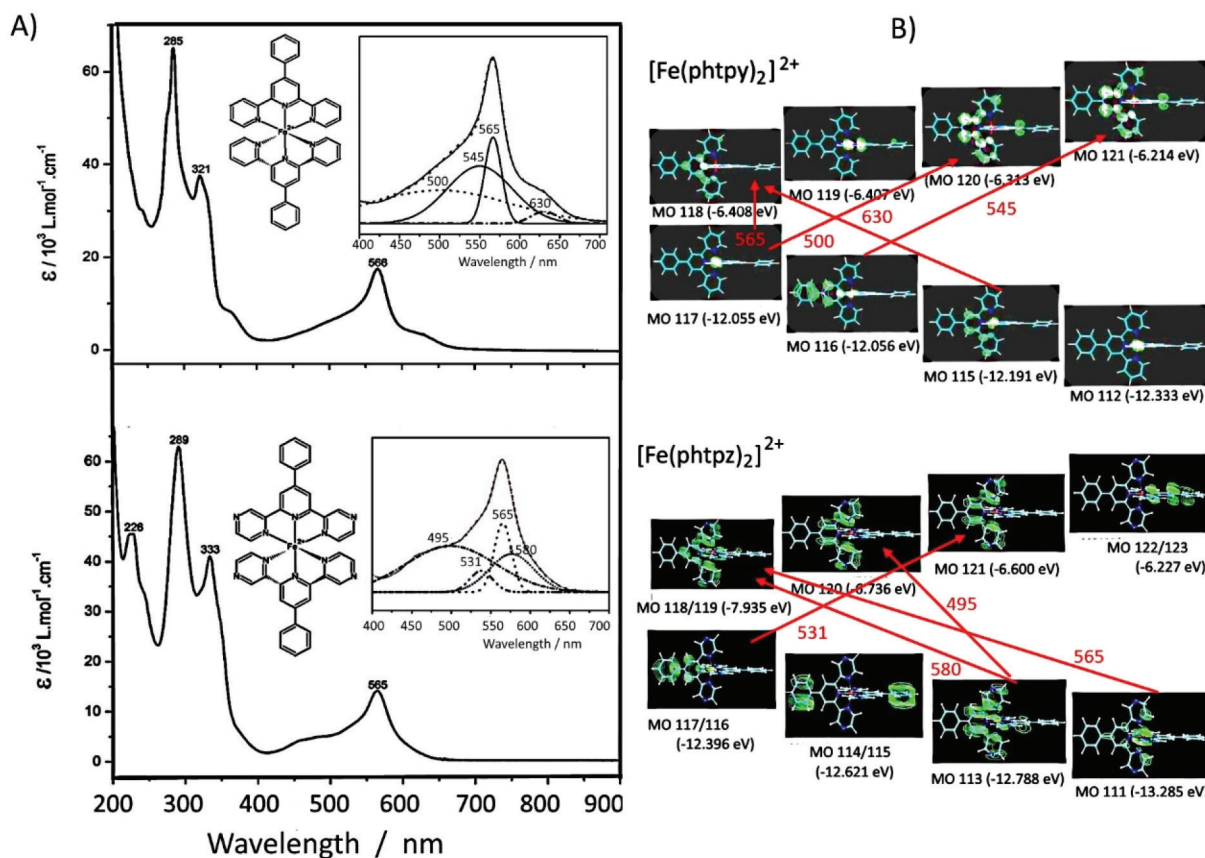
Figure 2. (A) Electronic spectra of the [Fe(phtpy)$_2$]$^{2+}$ and [Fe(phtpz)$_2$]$^{2+}$ complexes in the UV-visible region, showing the spectral deconvolution in the inset, and (B) the relevant HOMO and LUMO levels associated with the respective charge-transfer bands

67
1023

Vol. 42, No. 9   Raman studies of bis(phenylterpyrazine)iron(II) and supramolecular species with pentacyanidoferrate(II) ions

levels, and their corresponding energies, as shown in Figure 2 B and Table 1. According to the theoretical simulation, the HOMO levels of the $[Fe(phtpy)_2]^{2+}$ complex are essentially localized on the Fe(II) center, while for the $[Fe(phtpz)_2]^{2+}$ complex there is a substantial delocalization all over the molecule including the phenyl group (Figure 2 B). The LUMO levels for the $[Fe(phtpy)_2]^{2+}$ complex are also more localized on the central pyridine ring as compared with the delocalization over the terpyrazine moiety for the $[Fe(phtpz)_2]^{2+}$ complex.

The lowest energy CT bands for the $[Fe(phtpy)_2]^{2+}$ and $[Fe(phtpz)_2]^{2+}$ complexes are quite distinct, and can be observed at 630 and 580 nm, respectively, in Figure 2 A. For the terpyridine complex, the electronic delocalization in the HOMO levels (MO 115, MO 113) is smaller than in the terpyrazine case (see Figure 2 B). The same reasoning applies to the remaining levels. In the $[Fe(phtpy)_2]^{2+}$ complex the electronic distribution seems more localized on the iron(II)-terimine chromophore, while in the $[Fe(phtpz)_2]^{2+}$ species, the delocalization extends to the pyrazine moieties, thus involving an iron(II)-terpyrazine chromophore.

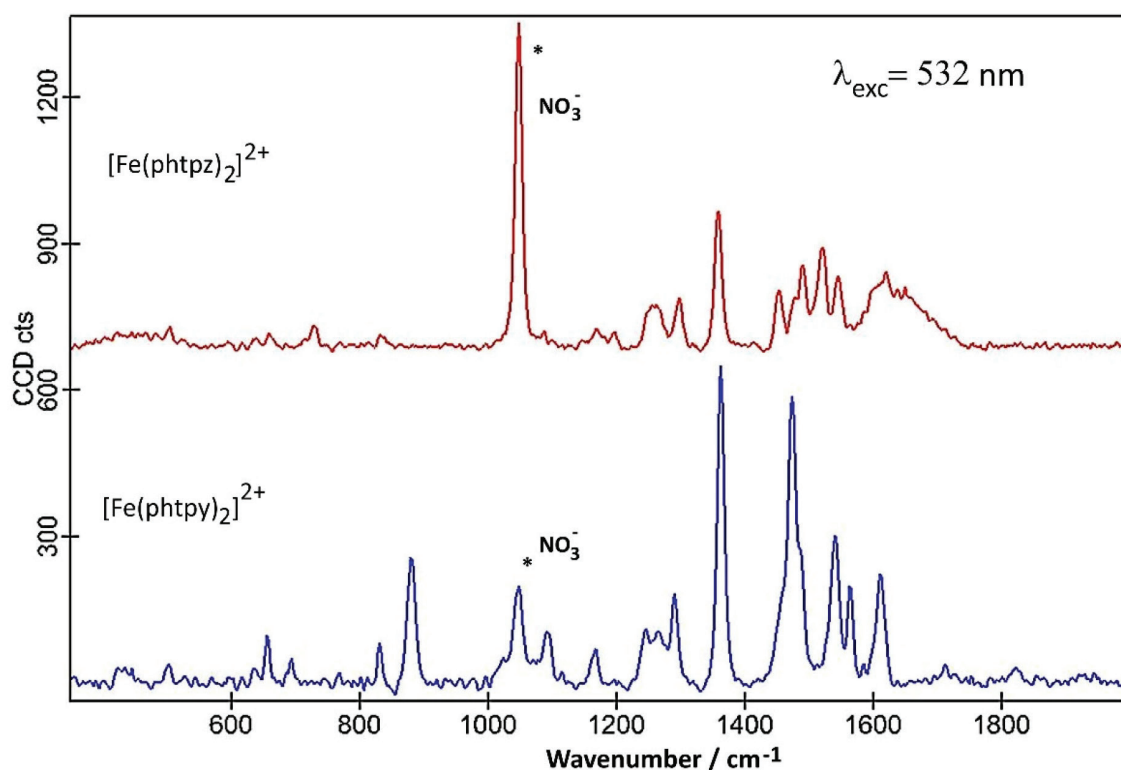### Raman spectra of the $[Fe(phtpy)_2]^{2+}$ and $[Fe(phtpz)_2]^{2+}$ complexes

As observed for the iron(II) diimine complexes, the Raman spectra of the terimine analogues excited in the visible region, exhibited a selective enhancement, reflecting the the chromophore groups in the process. It should be noted that in the resonance Raman spectra, only the vibrational groups of the chromophores are enhanced, contrasting with the general vibrational spectra in the infrared region.

The enhancement of the vibrational peaks can be demonstrated by using an internal standard, such as KNO_3. As a matter of fact, in Figure 3, the intensity of the Raman signals for the complexes, obtained at a very low concentration (5×10^{-5} mol L^{-1}), are comparable to the normal Raman scattering of the NO_3^- internal standard (0.3 mol L^{-1}), thus corroborating a large enhancement, typical of the resonance Raman effect.

DFT calculations of the Raman spectrum of the $[Fe(phtpy)_2]^{2+}$ complex led to more than 200 peaks, but the most strongly enhanced peaks were observed at 1711, 1687, 1681, 1671, 1558, 1546, 1403 and

Table 1. Experimental and Theoretical Analysis of the Visible Charge-Transfer bands of the iron(II)-terimine complexes

Compound	Experimental λ_{max}/nm (logε)	Theoretical osc.strength	Assignment MO → MO* (major distribution)
$[Fe(phtpy)_2]^{2+}$	630	624 (0.010)	MO115(Fe) → MO118/9(Fe+tpy)
	565 (4.44)	591 (0.260)	MO117(Fe) → MO118/9(Fe+tpy)
	545	513 (0.080)	MO116(Fe) → MO121(tpy)
	500	467 (0.260)	MO115(Fe) → MO120(tpy)
$[Fe(phtpz)_2]^{2+}$	580	605 (0.003)	MO113(Fe+tpz) → MO118/9(Fe+tpz)
	565 (4.16)	565 (0.196)	MO111(Fe) → MO118/9(Fe+tpz)
	535	518 (0.023)	MO116(Fe+tpz) → MO121(tpz)
	495	463 (0.523)	MO113(Fe+tpz) → MO120(tpz)

Figure 3. *Raman spectra of the [Fe(phtpy)_2]²⁺ and [Fe(phtpz)_2]²⁺ complexes (5 x 10⁻⁵ mol L⁻¹) in the presence of KNO_3 (0.3 mol L⁻¹), _exc = 532 nm*

1277 cm^{-1} involving a rather complex composition of the vibrational modes of the phenyl and pyridyl rings. Although the theoretical frequencies are close to the those experimentally observed for the complex (Figure 3), their intensities do not reproduce the observed spectral patterns because of the wavelength dependence introduced by the resonance Raman effect.

The structural characteristics of the two complexes turn the assignment the phenyl, pyridine and pyrazine bands a very challenging task. The comparison of the two complexes may be helpful, since they have in common a phenyl group and a central pyridine moiety, so that the differences should arise from the four peripheral pyridyl groups in the $[Fe(phtpy)_2]^{2+}$ complex, and the four peripheral pyrazyl groups in the $[Fe(phtpz)_2]^{2+}$ case.

The Raman spectra of the $[Fe(phtpy)_2]^{2+}$ complex is shown in Figure 4. In principle there are four spectral regions; a) from 1400 to 1700 cm^{-1} encompassing C-C stretching vibrations in the common phenyl and central pyridyl moieties, and in the distinct peripheral pyridyl groups; b) from 1000 to1400 cm^{-1} involving composite ν_{CC}, ν_{CN}, and δ_{CH} vibrational modes of the phtpy ligand; c) from 500 to 1000 cm^{-1} corresponding to δ_{CH} and δ_{CCN} modes and d) below 500 cm^{-1} involving ν_{Fe-N} and low frequency skeleton modes.[20,21]

As shown in Figure 2 B, at 633 nm the excitation of $[Fe(phtpy)_2]^{2+}$ complex involves the electronic band at 630 nm, corresponding to the excited MO 118/119 mainly localized on the central pyridyl ring with a small distribution on the neighboring diamine bonds. The phenyl group is not involved in this excitation. Therefore, it is plausible that the observed bands arise from the central pyridyl and the interconnected diimine bonds. The peaks at 504 and 349 cm^{-1} correspond to the ν_{Fe-N} stretching vibrations. The excitation at 488 nm coincides with the absorption band at 500 nm, involving MO 120 localized on the Fe-tpy chromophore. Excitation at 532 nm was less conclusive, since it involves a strong overlap of the absorption bands at 565, 545 and 500 nm, and this is reflected in a complex vibrational profile encompassing more than a single excited state.

Considering the characteristics of the molecular orbitals involved (118/119 and 120, in Figure 2 B) it is plausible that the peaks simultaneously enhanced at 488 and 630 nm belong to Fe-tpy vibrations; while those preferentially enhanced at 630 nm are associated with the Fe-py(central) core and those preferentially enhanced at 488 nm involve Fe-py(peripheral) vibrations. Therefore, the common peaks at 630 and 488 nm, e. g. 1607, 1471, 1362, 1293, 1166, 1021, 693, 655 cm^{-1} peaks should correspond to Fe-tpy vibrations. The peaks at 1521 and 1037 should correspond to Fe-py(central) vibrations, while the peaks at 1543, 1486, 1271, 1249, and 1096 cm^{-1} should correspond to Fe-py(peripheral) vibrations.

The Raman spectra of the $[Fe(phtpz)_2]^{2+}$ complex are shown in Figure 5. In this case, the 633 nm excitation involves the MO 118/119, which is delocalized over the iron(II)-terpyrazine (Fe-tpz) chromophore. The phenyl group is not involved in this excitation. Therefore, it is plausible that the observed bands arise from Fe-tpz chromophore. The peaks at 506 and 350 cm^{-1} are compatible with the ν_{Fe-N} stretching vibrations. On the other hand, the excitation at 488 nm involves preferentially MO 120 which is also localized on the Fe-tpz chromophore. The excitation at 532 nm involves a strong overlap of the absorption bands at 565, 535 and 495 nm, and this is reflected in the complex vibrational profile encompassing more than one single excited state.

As one can see in Figure 5, although the Raman profiles observed at 633 and 488 nm are quite different, the corresponding molecular orbitals are spread over the Fe-tpz chromophore (Figure 2 B), and the contributions of the central pyridine and lateral pyrazine rings in the Raman spectra cannot be readily discriminated.

In summary, the vibrational frequencies of the two complexes were collected in Table 2, with a tentative assignment as discussed before. For comparison purposes, a new column has also been added involving the corresponding pentacyanidoferrate (PC) species, commented in the following section.
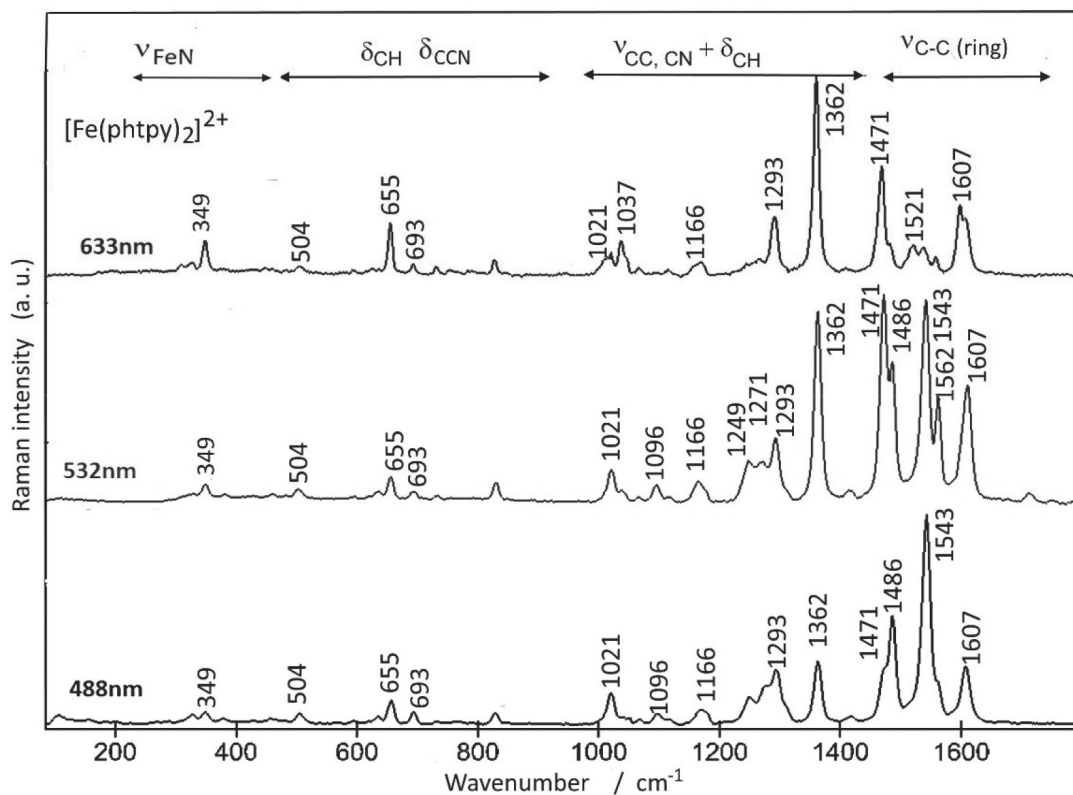

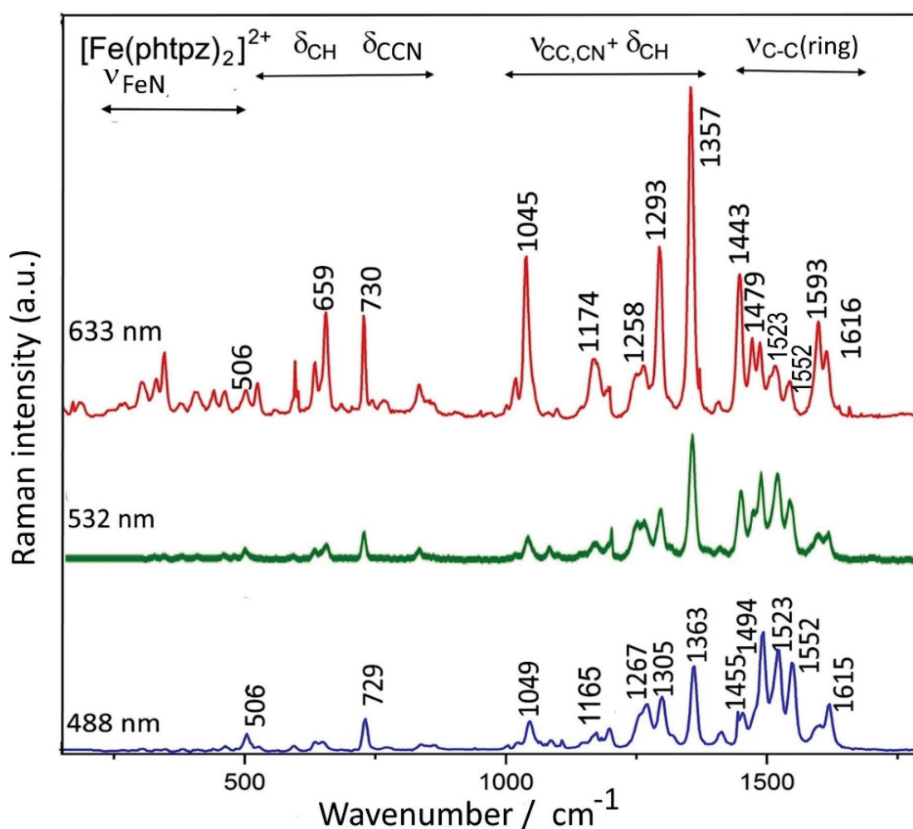**Figure 4.** *Raman spectra of $[Fe(phtpy)_2]^{2+}$ at several excitation wavelengths*

Figure 5. *Resonance Raman spectra of [Fe(phtpz)₂]²⁺ at several excitation wavelengths, showing the distribution of the vibrational modes*

Table 2. Enhanced Raman peaks (cm⁻¹) for the $[Fe(phtpy)_2]Cl_2$, $[Fe(phtpz)_2]Cl_2$ and $[Fe(phtpz)_2\{PCF\}_4]^{10-}$ complexes and their tentative assignment

cm⁻¹	$[Fe(phtpy)_2]Cl_2$	cm⁻¹	$[Fe(phtpz)_2]Cl_2$	cm⁻¹	$[Fe(phtpz)_2\{PCF\}_4]^{10-}$
				2101	ν_{CN}
				2071	ν_{CN}
1607	ν_{CC} tpy	1616	ν_{CC} tpz		
1562	ν_{CC} py(c)*	1593	ν_{CC} tpz	1576	ν_{CC} pz
1543	ν_{CC} py(p)*	1552	ν_{CC} tpz		
1521	ν_{CC} py(c)	1523	ν_{CC} tpz	1513	ν_{CC} pz
1486	ν_{CC} py(p)	1494	ν_{CC} tpz		
1471	ν_{CC} tpy	1479	ν_{CC} tpz		
		1443	ν_{CC} tpz		
1362	$\nu_{CC,CN} + \delta_{CH}$ tpy	1357	$\nu_{CC,CN} + \delta_{CH}$ tpz	1359	$\nu_{CC,CN} + \delta_{CH}$ pz
1293	$\nu_{CC,CN} + \delta_{CH}$ tpy	1293	$\nu_{CC,CN} + \delta_{CH}$ tpz	1283	$\nu_{CC,CN} + \delta_{CH}$ pz
1271	$\nu_{CC,CN} + \delta_{CH}$ py(p)	1258	$\nu_{CC,CN} + \delta_{CH}$ tpz		
1166	$\nu_{CC,CN} + \delta_{CH}$ tpy	1174	$\nu_{CC,CN} + \delta_{CH}$ tpz	1156	$\nu_{CC,CN} + \delta_{CH}$ pz
1037	$\nu_{CC,CN} + \delta_{CH}$ py(c)				
1021	$\nu_{CC,CN} + \delta_{CH}$ tpy	1045	$\nu_{CC,CN} + \delta_{CH}$ tpz	1021	$\nu_{CC,CN} + \delta_{CH}$ pz
693	$\delta_{CH}, \delta_{CCN}$ tpy	730	$\delta_{CH, CCN}$ tpz		
655	$\delta_{CH}, \delta_{CCN}$ tpy	659	$\delta_{CH, CCN}$ tpz	658	$\delta_{CH}, \delta_{CCN}$ pz
504	ν_{Fe-N} Fetpy	506	$\nu_{Fe-Ntpz}$	404	ν_{Fe-CN}

* (c) = central, (p) = peripheral.

As shown in Table 2, the differentiation of the pyridine and pyrazine vibrational modes in the $[Fe(phtpz)_2]^{2+}$ complex has not been possible based on the molecular orbitals involved, in spite of the contrasting Raman profiles observed at distinct excitation wavelenghts. However, the presence of the pyrazine moieties allow a local perturbation by forming coordination bonds with pentacyanidoferrate(II) ions.[10]

Polynuclear [Fe(phtpz)₂{Fe(CN)₅}₄]¹⁰⁻ complex

The [Fe(phtpz)₂]²⁺ complex exhibits four pyrazyl groups which can bind additional metal ions, in contrast to the pyridyl group, and this strategy can be explored to differentiate the pyrazyl and pyridyl group vibrations.

As a matter of fact, the binding of the [Fe^{II}(CN)₅]³⁻ groups to the pyrazyl moieties leads to the rise of two new MLCT bands, at 460 and 700 nm, as shown in Figure 5. No such change is observed when the [Fe(phtpy)₂]²⁺ complex is treated with [Fe(CN)₅]³⁻ ions. As a matter of fact, the absorption band at 460 nm is typical of [Fe(CN)₅L]³⁻ complexes containing pyrazine ligands,[10] and correspond to the peripheral complexes around the iron(II)-terpyrazine core. On the other hand, the absorption band at 700 nm can be ascribed to a new charge-transfer transition from the iron(II)-center to the bridging
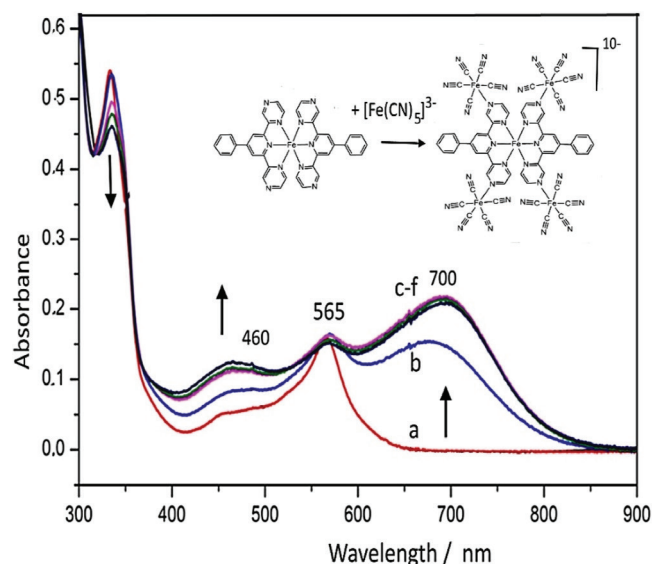

Figure 6. *Changes in the electronic spectrum of [Fe(phtpz)₂]²⁺ (a) in the presence of successive amounts of Na₃[Fe(CN)₅NH₃], in aqueous solution, up to the saturation point (b-f)*

pyrazine-Fe(CN)₅ complex. It is also observed when the pyrazine moieties are protonated, indicating the lowering of an excited π* orbital of the pyrazyl group induced by the peripheral metal ion or protons.

The [Fe(phtpz)₂]²⁺ complex reacts with [Fe(CN)₅]³⁻ ions in solution, increasing the absorption at 460 and 700 nm up to the 1:4 proportion, corresponding to the saturation point. The pentanuclear complex has a deep blue-violet color, and remains stable in aqueous solution, with no evidence of decomposition even after months. In spite of the apparent repulsion of the [Fe(CN)₅]³⁻ negative charges, one can see in the stereochemical model (Figure 7) that they are located quite far, practically in distant orthogonal positions.

The Raman spectrum of the [Fe(phtpz)₂{Fe(CN)₅}₄]¹⁰⁻ complex can be seen in Figure 8, in comparison with the spectrum of the [Fe(phtpz)₂]²⁺ species at the same excitation wavelength (633 nm). The presence of the [Fe(CN)₅]³⁻ complexes is evidenced by the characteristic[22] ν_{CN} stretching vibrations at 2070 and 2101 cm⁻¹, and the ν_{Fe-C} band at 404 cm⁻¹ (Figure 8 B). Their selective binding to the pyrazine moieties should promote a selective enhancement of the new Fe-pz-Fe chromophore group absorbing at 700 nm (Figure 6), allowing to discriminate the characteristic frequencies of the pz ring. For this reason, the Raman spectra of the pentanuclear complex was actually much simpler than that for the [Fe(phtpz)₂]²⁺ core. In this way, the ν_{CN}, ν_{CC} vibrations at 1593 and 1523 cm⁻¹ can be ascribed to the pyrazine moieties (Figure 8 A) converting into the 1576 and 1513 cm⁻¹ peaks in the pentanuclear complex, thus corroborating the proposed binding to the pentacyanidoferrate(II) ions (Figure 8 B). The $_{CC}$ peaks at 1616, 1552, 1494, 1479, 1443 cm⁻¹ and the δ_{CCN} peak at 730 cm⁻¹ are not enhanced in the pentanuclear complex and should belong to the central Fe-pyridyl group. Analogously, the $\nu_{CC,CN}$ peaks at 1357, 1293, 1174, the ν_{ring} peak at 1045 cm⁻¹ and the δ_{CCN} peak at 659 cm⁻¹ are selectively enhanced in the pentanuclear complex and can be associated with the local pyrazine modes influenced by the [Fe(CN)₅]³⁻ coordination. In this way, the elucidation of the enhanced pyrazine modes could be performed, improving the assignment of the Raman spectra of the [Fe(phtpz)₂]²⁺ complex, as shown in Table 2.

In the presence of transition metal ions, such as Fe(III) and Zn(II) the [Fe(phtpz)₂{Fe(CN)₅}₄]¹⁰⁻ complex forms insoluble extended
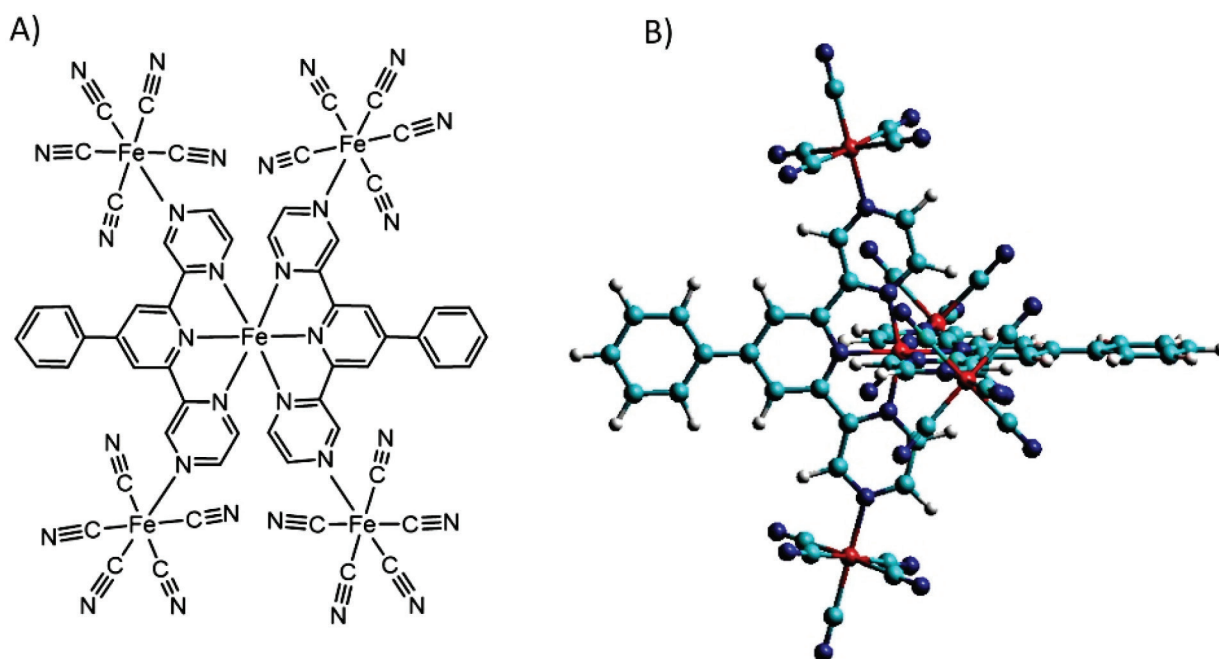
Figure 7. *Structural representation of the pentanuclear complex [Fe(phtpz)₂{Fe(CN)₅}₄]¹⁰⁻ and its stereochemical view*

71

Vol. 42, No. 9   Raman studies of bis(phenylterpyrazine)iron(II) and supramolecular species with pentacyanidoferrate(II) ions   1027
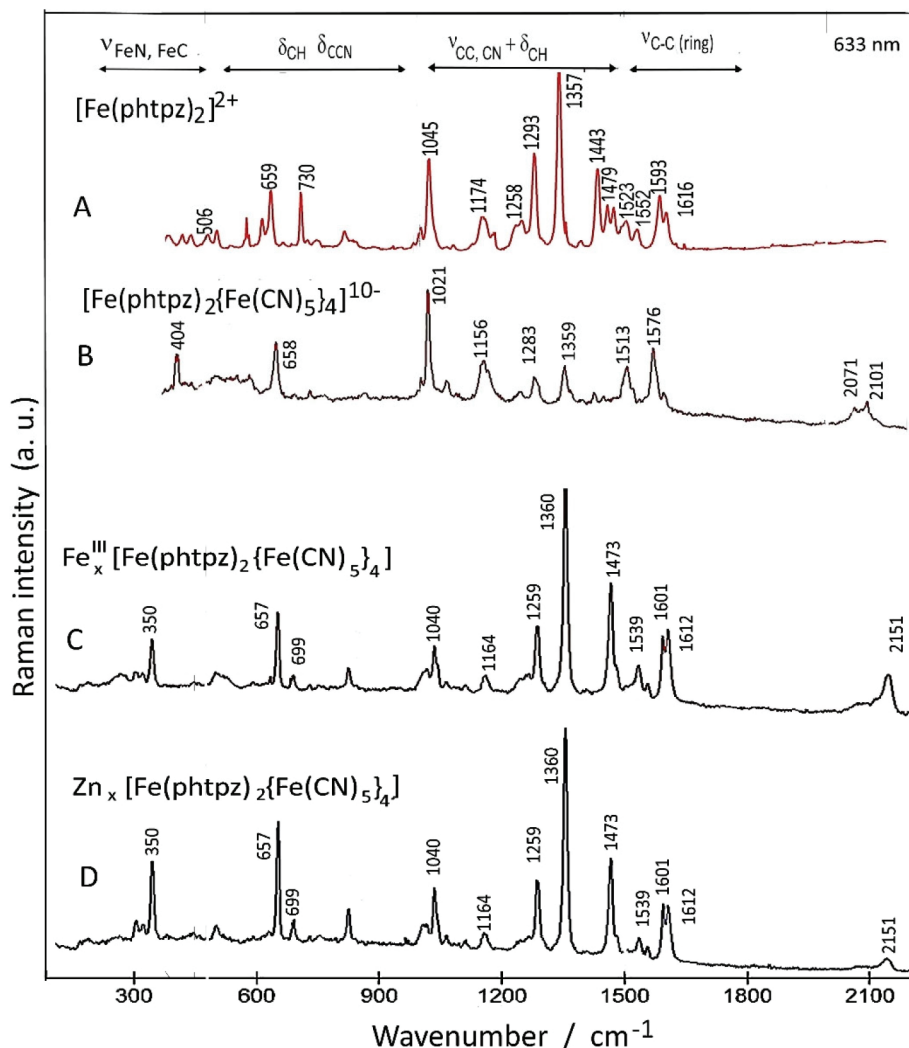
Figure 8. *Comparative resonance Raman spectra (633 nm) of the [Fe(phtpz)$_2$]$^{2+}$ (A) , [Fe(phtpz)$_2${Fe(CN)$_5$}$_4$]$^{10-}$ (B) and Fe$_x$[Fe(phtpz)$_2${Fe(CN)$_5$}$_4$] and Zn$_x$[Fe(phtpz)$_2${Fe(CN)$_5$}$_4$] complexes in PVA films (C)*

polymers, analogous to the Prussian Blue compound, through the formation of Fe^{II}-CN-Fe^{III} or Fe^{II}-CN-Zn^{II} bonds.[23] Their electronic species can be seen in Figure 9. The Fe$_x$[Fe(phtpz)$_2${Fe(CN)$_5$}$_4$] exhibit a broad intervalence transfer band around 750 nm, as in the Prussian Blue complex. The lowest energy charge transfer band is also apparent the polymeric complex, showing the perturbation of the pyrazine groups by the pentacyanidoferrate complexes.

The corresponding resonance Raman spectra are quite well defined as shown in Figure 8 C, D. The ν_{CN} frequency is shifted to 2151 cm^{-1} indicating the binding of the cyanide ligand to the Fe(III) and Zn(II) metal ions.[21] Analogously, the peak at 350 cm^{-1} can be ascribed to ν_{Fe-CN}[22] The vibrational spectra of the [Fe(phtpz)$_2${Fe(CN)$_5$}$_4$]$^{10-}$ is nearly preserved in the extended polymer, showing a large enhancement of the $\nu_{CC,CN}$ vibration of the peripheral pz vibration at 1360 cm^{-1}. The vibrational peaks of tpz at 1494, 1523 and 1552 cm^{-1} as well as at 730 cm^{-1} practically disappear, reflecting their strong perturbation by the attached pentacyanidoferrates.

CONCLUSION

The iron(II) terpyrazine complex [Fe(phtpz)$_2$]$^{2+}$ exhibits a strong electronic delocalization on the Fe(II) terimine chromophore, encompassing the lateral pyrazyl groups and contrasting with the iron(II) terpyridine derivative. The assignment of the resonance
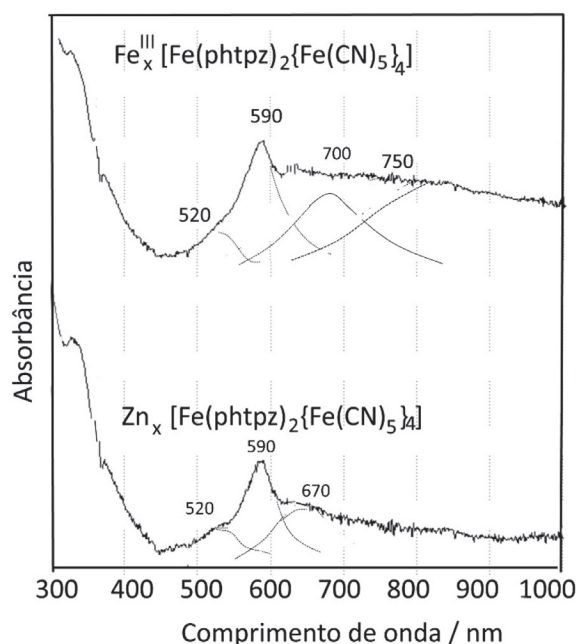
Figure 9. *Absorption spectra of the Fe$_x$[Fe(phtpz)$_2${Fe(CN)$_5$}$_4$] and Zn$_x$[Fe(phtpz)$_2${Fe(CN)$_5$}$_4$] complexes in PVA films*

Raman peaks has been tentatively proposed by comparing the spectra of these two systems. The pyrazine groups were explored to bind $[Fe(CN)_5]^{3-}$ species, generating stable pentanuclear complexes displaying additional charge-transfer bands in the visible. The resonance Raman spectra reflected the presence of the pentacyanidoferrate(II) complexes, and the strong influence on the resonance Raman bands of the pyrazine groups allowed their discrimination from a rather complicated resonance Raman study. The pyrazine coordination features were also explored in the formation of polymeric complexes, similar to Prussian Blue, in the presence of transition metal ions.

ACKNOWLEDGEMENTS

REFERENCES

1. Krumholz, P.; *J. Am. Chem. Soc.* **1953**, *75*, 2163.
2. Krumholz, P.; Serra, O. A.; DePaoli, M. A.; *Inorg. Chim. Acta* **1975**, *15*, 25.
3. Sone, K.; Krumholz, P.; Stammreich, H.; *J. Am. Chem. Soc.* **1955**, *77*, 777.
4. Li, L.; Niu, S.-Y.; Li, D.; Jin, J.; Chi, Y.-X.; Xing, Y.-H.; *Inorg. Chem. Commun.* **2011**, *14* , 993.
5. Pai, S.; Schott, M.; Niklaus, L.; Posset, U.; Kurth, D. G.; *J. Mater. Chem. C* **2018**, *6*, 3310.
6. Zedler, L.; Krieck, S.; Kupfer, S.; Dietzek, B.; *Molecules* **2019**, *24*, 245.
7. Assumpcao, A. M. C.; Bonacin, J. A.; Toma, S. H.; Zamarion, V. M.; Toma, H. E.; *Can. J. Chem.* **2014**, *92*, 918.
8. Wang, J. H.; Hanan, G. S.; *Synlett* **2005**, 8, 1251.
9. Toma, H. E.; Malin, J. M.; *Inorg. Chem.* **1973**, *12*, 2080.
10. Toma, H. E.; Malin, J. M.; *Inorg. Chem.* **1973**, *12*, 1039.
11. Toma, H. E.; Lever, A. B. P.; *Inorg. Chem.* **1986**, *25*, 176.
12. Matsumoto, F. M.; Temperini, M. L. A.; Toma, H. E.; *Electrochim. Acta* **1994**, *39*, 385.
13. Zerner, M. C.; ZINDO PROGRAM V.98.1 - Quantum Project, University of Florida, Gainesville, Florida, 1998.
14. Gorelsky, S. I.; Lever, A. B. P.; *J. Organomet. Chem.* **2001**, *635*, 187.
15. Constable, E. C.; Lewis, J.; Liprot, M. C.; Raithby, P. R.; *Inorg.Chim Acta* **1990**, *178*, 47.
16. Alexander, B. D.; Dines, T. J.; Longhurst, R. W.; *Chem. Phys.* **2008**, *352*, 19.
17. Albrecht, A. C.; *J. Chem. Phys.* **1961**, *34*, 1476.
18. Clark, R. J. H.; Dines, T. J.; *Angew. Chem., Int. Ed.* **1986**, *25*, 131.
19. Efremov, E. V; Ariese, F.; Gooijer, C.; *Anal. Chim. Acta* **2008**, *606*, 119.
20. Burger, K.; Wagner, F. E.; Vertes, A.; Bencze, E.; Mink, J.; Labadi, I.; Nemes-Vetessy, Z.; *J. Phys.Chem. Solids* **2001**, *62*, 2059.
21. Mallick, P. K.; Danzer, G. D.; Strommen, D. P.; Kincaid, J. R.; *J. Phys. Chem.* **1988**, *92*, 5628.
22. Hipps, K. W.; Williams, S. D.; Mazur, U.; *Inorg. Chem.* **1984**, *23*, 3500.
23. Shinohara, J. S.; Grasseschi, D.; Almeida, S. N.; Toma, H. E.; *An. Acad. Bras. Ciênc.* **2019**, *9*, 2.

CrossMark

RESEARCH PAPER

Facile synthesis of labile gold nanodiscs by the Turkevich method

Daniel Grasseschi [ORCID] **· Maria Luiza de O. Pereira ·
Jorge S. Shinohara · Henrique E. Toma**

Abstract The Turkevich method has been the preferred one for synthesis of gold nanoparticles (AuNPs), owing to its apparent simplicity and facility of replacing the citrate ions on the particle surface by molecules exhibiting different functionalities. Using the most common procedure labile spherical nanoparticles are usually obtained by this method. Here, by using factorial design of experiments, we demonstrated that gold nanodiscs (AuNDs) with short aspect ratio can be generated by the Turkevich method when Au:citrate ratio is 1:1. In comparison with the CTAB capped gold nanorods (AuNR), the citrate stabilized AuNDs exhibited a more labile character, allowing fast ligand exchange reactions and easy functionalization of the nanoparticle surface. In the presence of 4-mercaptopyridine (4-mpy), the surface enhancement Raman scattering effect was 100 and 1000 times higher than the one observed for CTAB-AuNR and spherical AuNPs, respectively, increasing the 4-mpy detection limit to 2.5×10^{-9} molL^{-1}.

Keywords Anisotropic gold nanoparticles · Turkevich · Factorial design · Surface ligand exchange · Nanobiomaterials

D. Grasseschi (✉)
MackGraphe - Graphene and Nanomaterials Research Center, Mackenzie Presbyterian University, 01302-907, São Paulo, Brazil
e-mail: daniel.grasseschi@usp.br

M. L. de O. Pereira · J. S. Shinohara · H. E. Toma
Departamento de Química Fundamental, Instituto de Química, Universidade de São Paulo, São Paulo, Brazil

Introduction

The most widely used method for spherical gold nanoparticle (AuNP) synthesis consists in the chemical reduction of tetrachloroauric acid by citrate ions. In this method, initially proposed by Turkevich (Turkevich et al. 1951, 1953; Turkevich 1985a, b), and slightly modified by Frens (1973), the AuNPs are stabilized with citrate (Ji et al. 2007) or its oxidation products (Grasseschi et al. 2015a). Due to the poor affinity between carboxylate species and the surface gold atoms, the resulting AuNPs can exchange the citrate ligands very easily, imparting labile properties (Toma et al. 2010). For this reason, the surface properties of Turkevich AuNPs can be engineered by simple surface ligand exchange reactions, making possible its application in different areas (Zamarion et al. 2008; Grasseschi et al. 2010; Wang and Ma 2009).

Turkevich was the first to demonstrate that the AuNP size can be controlled by citrate concentration (Turkevich et al. 1951). Since then, three distinct key roles have been attributed to the citrate ligands: reducing agent, surface stabilizing agent, and pH mediator (Ji et al. 2007). The proportion between citrate and gold salt can modify the reaction pH, affecting the gold coordination sphere (Ojea-Jiménez and Campanera 2012), the gold reduction reaction, and consequently the AuNP growth, generating particles with different size (Turkevich et al. 1951; Kimling et al. 2006), shape (Ji et al. 2007; Pei et al. 2004; Liu et al. 2009), surface functionalization (Grasseschi et al. 2015a), and growth kinetics (Pong et al. 2007).

Despite all advantages related to the simplicity of the Turkevich method, spherical AuNPs show a smaller electric field enhancement during the excitation of their localized surface plasmons. This way, the design of metallic nanoparticles with different shapes has been pursued by many research groups in recent years (Personick and Mirkin 2013; Lohse et al. 2014; DuChene et al. 2013), and a special attention has been dedicated to nanoparticles with corners and tips, such as rods and prisms, due to local enhancement of the electromagnetic field promoted by the lighting rod effect (Ermushev et al. 1993). Such nanoparticles are enabling important applications in chemistry and biology as surface-enhanced Raman scattering (SERS) substrates (Stewart et al. 2008).

Anisotropic AuNPs can be obtained by employing biological extracts as reducing and stabilizing agents (Ogi et al. 2009; Shankar et al. 2004, 2005; Liu et al. 2005). However, in this case, the particle size and shape control is hampered by the matrix complexity and usually long reaction times. The use of a polymeric matrix represents another important alternative (Kim et al. 2004; Lim et al. 2008; Xiong et al. 2006), although the use of a surfactant matrix is becoming more competitive for practical reasons, for instance, the possibility of using lower reaction temperatures and short times (Jana et al. 2001a; Lohse and Murphy 2013).

The synthesis of anisotropic gold nanoparticles in surfactant solutions has been performed by the seed-mediated method, using cetyltrimethylammonium bromide (CTAB) micelles as templates (Murphy and Jana 2002; Gole and Murphy 2004). The rationale of this method is associated with the influence of the cationic anisotropic CTAB micelles, directing the growth of pre-synthesized isotropic AuNPs (the seeds) (Gole and Murphy 2004). Murphy et al. (Lohse et al. 2014) suggested that the anisotropic growth is governed by chemical and steric factors, such as the interaction between quaternary ammonium group and the {100} gold surface. This process is accompanied by the [Au-Br-CTA] complex formation. The shape control can be achieved by changing the gold/CTAB molar ratio (Jana et al. 2001b), by the nature of surfactant counter-ion (Grasseschi et al. 2016), by adding co-surfactants like hexadecylbenzyldimethylammonium bromide (Nikoobakht and El-Sayed 2003), Ag^{+1} (Liu and Guyot-Sionnest 2005) or I^{-1} (Lohse et al. 2014; Kim et al. 2013) ions. However, the strong interaction between CTAB and the gold surface decreases the rate of surface ligand exchange reactions, making difficult further functionalization. Besides that, the high amount of surfactant on the AuNP surface can enhance temporal fluctuations of the Raman signal, known as blinking effect (Vianna et al. 2016; Mezni et al. 2014), and its removal can lead to shape changes impairing the AuNP properties (Pan et al. 2015).

Here, we show the synthesis of labile anisotropic gold nanodiscs (AuNDs) by the Turkevich method, based on a multivariated statistical analysis encompassing a 2^4 factorial design of experiments (Gunst et al. 1996). By monitoring the AuNP size and shape, we evaluated, under a wide range of experimental parameters, the synergistic effects that lead to anisotropic AuND formation. Transmission electron microscopy and UV-visible spectroscopy suggest that the anisotropic AuNDs are formed via the silver halide or attachment mechanism and the presence of stacking faults on the crystalline structure are crucial for the formation of AuNDs. Additionally, using SERS, we proved the AuND labile character, which, in combination with the lighting rod effect, leads to higher enhancement factors when compared with spherical AuNPs and gold nanorods (AuNR) synthesized by the conventional CTAB method.

Experimental section

Gold nanoparticles synthesis by Turkevich method
For precaution, all the glassware was previously

Table 1 Experimental factors of the 2^4 factorial design

Factors		T (°C)	Stirring (rpm)	V_{cit} (mL)	Addtion ($\mu L s^{-1}$)
Levels	+	95	1700	1.7	1000
	−	85	900	0.65	100
	Middle point	90	1300	1.1	500

washed with aqua regia (3HCl:1HNO$_3$). Using a three-neck round bottom flask, 50 mL of 5×10^{-4} molL^{-1} HAuCl$_4$ aqueous solution was heated using an Arduino microcontroller system with precision of ± 1 °C, under reflux and different stirring rate, during 30 min. Different volumes of a 0.038 molL^{-1} citrate aqueous solution were added to the gold precursor solution using a peristaltic pump to control the addition rate. The heating and stirring were maintained during 5 min after citrate addition. Then, the solution was cooled to room temperature. We elected four experimental parameters as factors in the 2^4 factorial design: (1) temperature, (2) stirring rate, (3) citrate concentration, and (4) citrate addition rate. Table 1 shows the factor values and the levels of the factorial design. Citrate volume was varied between 0.65 and 1.7 mL to achieve a citrate:Au proportion of 1:1 and 3:1, according to the modifications introduced by Frens (1973) and our previous study (Grasseschi et al. 2015a). Table 2 shows details of the factorial design, with four factors at two levels for the Turkevich synthesis. The middle point level was carried out in duplicate in order to estimate the error (Gunst et al. 1996). Additionally, test 2 was repeated 3 times to proceed with all the AuND characterization.

The reaction volume and gold salt precursor concentration was kept constant. Thus, variations in temperature and citrate concentration should control the gold reduction reaction and consequently the AuNP nucleation. The effect of stirring rate was included aiming to scale up the synthesis in a further study, since it has a direct influence on the convection and diffusion of the species in solution, changing the rates of AuNP growth. However, its maximum and minimum values were chosen empirically based on our previous results (Grasseschi et al. 2015a) and the AuNP stability. Statistical analysis was performed using a Dell Statistica 13 software, which allows multiple comparison taking advantage of ANOVA analysis of variance (Gunst et al. 1996).

The synthesis of AuNR capped with CTAB is described on note 1 of the supplementary information.

Instrumentation Morphological characterization was made by means of Scanning Electron Microscopy (SEM) using a JEOL field emission electron microscope model 7200 operating at 7 kV and a working distance of 3 mm using a secondary electron detector. Particle size distributions were calculated by measuring the dimensions of 1000 particles in 10 different regions of the samples using ImageJ software. The aspect ratio was calculated considering the largest and smallest radius of each particle. Transmission Electron Miscroscopy (TEM) using a FEI Talos F200s

Table 2 2^4 Factorial design of gold nanoparticles Turkevich synthesis

Test	T (°C)	Stirring (rpm)	V_{cit} (mL)	Addtion ($\mu L s^{-1}$)
1	−	−	−	−
2	+	−	−	−
3	−	+	−	−
4	+	+	−	−
5	−	−	+	−
6	+	−	+	−
7	−	+	+	−
8	+	+	+	−
9	−	−	−	+
10	+	−	−	+
11	−	+	−	+
12	+	+	−	+
13	−	−	+	+
14	+	−	+	+
15	−	+	+	+
16	+	+	+	+
17	Middle P.	Middle P.	Middle P.	Middle P.

operating at 200 kV was used to acquire high res-
olution images and Selected Area Electron Diffrac-
tion(SAED) pattern.

A CytoViva ultra resolution imaging system, com-
posed by a dark-field hyperspectral arrangement
mounted on an Olympus BX51 microscope, was used
for recording Rayleigh scattering spectra of individ-
ual particles (Vainrub et al. 2006). Ultraviolet-visible
extinction spectra were recorded on a Hewlett Packard
8453A diode-ray spectrophotometer, in the 190–1100-
nm range. SERS spectra using 785 nm excitation
wavelength were recorded on an InPhotonics model
INP-AA-785ZZ spectrophotometer, equipped with a
diode laser.

Results and discussion

AuNP synthesis and characterization In a factorial
design, morphological parameters such as particle
diameter (d), size distribution (σ), and aspect ratio

(AR) were considered dependent variables to perform
a variance analysis (ANOVA) and the effect of each
experimental factor on these parameters was calcu-
lated. The effects can be interpreted as the change of
dependent variable (d, σ, and AR) mean value, when
one or more experimental factors are changed from its
minimal to maximum values. The SEM images for all
the synthesis in Tables 1 and 2 are shown on Figs. S1
and S2 of the support information. AuNPs σ were
measured over 1000 particles and their distributions
are shown on Figs. S3 and S4. AR was calculated con-
sidering the largest and smallest radii of each particle
and the results for all factorial design are shown in
Figs. S5 and S6. Here, we focus on the analysis of par-
ticle AR as function of the experimental parameters.
Variations on AuNPs d and σ with the experimental
parameters are very well discussed on the literature
and we briefly discuss it on note 2 and Figs. S7–S10
of the support information.

Figure 1a shows the calculated effects of individ-
ual and the combination of two experimental factors
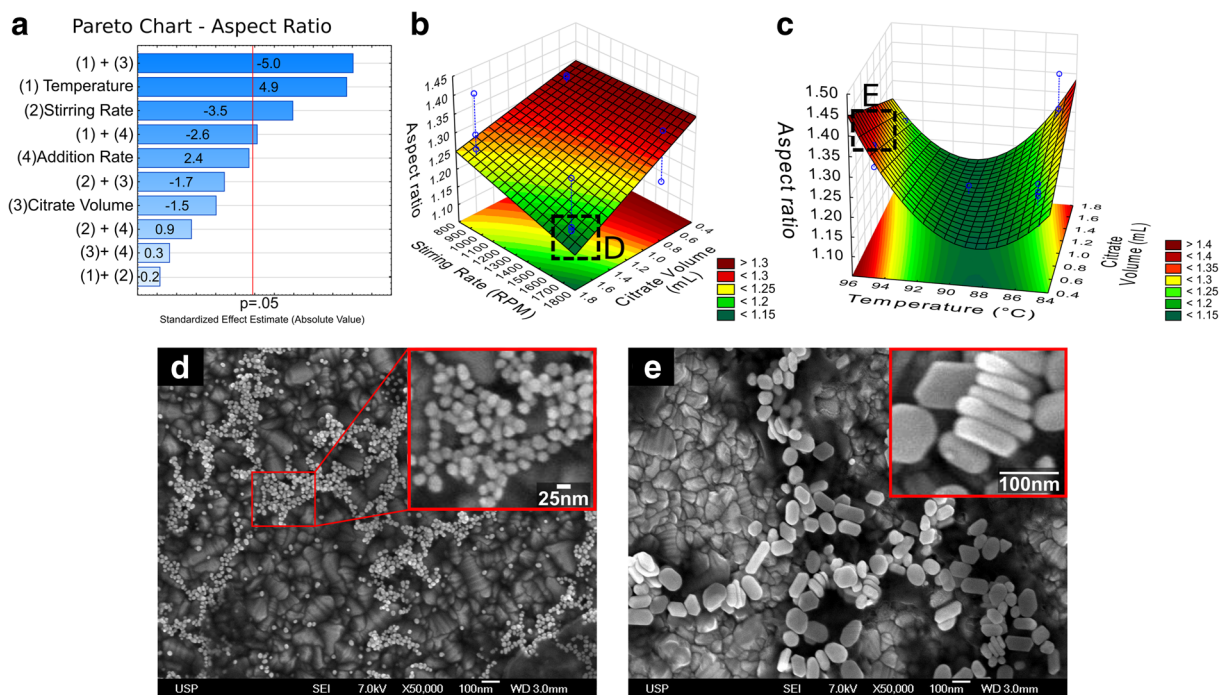
Fig. 1 a Pareto chart showing the calculated effect of experi-
mental parameters on particle aspect ratio. **b** Surface response
showing the variation on AR as function of stirring rate and
citrate concentration with temperature and addition rate fixed
on their higher values. The marked region show the optimal
conditions for AuNP synthesis. **c** Surface response showing the
variation on AR as function of temperature and citrate con-
centration with stirring rate fixed at the minimum value. The
marked region show the optimal conditions for AuND synthesis.
SEM imagens of AuNP (**d**) and AuND (**e**) samples

on particles AR in form of Pareto's chart (Gunst et al. 1996). In the ANOVA analysis, effects of combination of three and four experimental factors and the responses values at the middle point are used to calculate the experimental error (p). This error can be attributed to aleatory system fluctuations, e.g., uncertainties in the reactants weighted masses, and represents the system noise. Factors with effects smaller than the error can be discarded, because the fluctuations caused by changes on this factor are smaller than the noise. It is worthy to be notice that the middle point was duplicated to ensure good approximation for the error value, validating our experimental design.

This way, on Fig. 1a, the value of 4.9 for the temperature effect means that when the temperature increases in the average the AR becomes 4.9% greater. Therefore, according to Fig. 1a, a complex combination of experimental factors have significant influence on the AR. Surprisingly, the combination of citrate concentration and temperature shows a higher effect on the AuNP aspect ratio, and when both factors are increased simultaneously, a decrease of AuNPs AR is observed. In contrast, if only the temperature is altered an increase in the AR is observed. More surprising is the low effect of the citrate concentration when only this parameter is changed. This way, temperature and citrate concentration acts in a synergistic way to control the particles anisotropy.

Visualization of these tendencies on the AR becomes clear by plotting the response surfaces. Figure 1b shows the AR variation as a function of stirring rate and citrate concentration, considering the temperature and addition rate at their maximum values. The adjusted R^2 was 0.926, showing a good fitting of experimental data with the surface response. As can be seen in Fig. 1b, using high stirring rates and citrate concentration the AR drops, reaching values closer to 1. Figure 1d shows that AuNPs synthesized in this conditions are spherical with a small σ (see Fig. S3 and Table S1 on the Support Information). On the other hand, using smaller stirring rate the AR increases.

Now, looking at the AR response surface considering variations in temperature and citrate concentration, with stirring rate fixed at its minimum value (Fig. 1c), a parabolic behavior is observed, where for intermediate temperatures particles that are more spherical, with AR close to 1, are formed. While for extreme temperatures (85 and 95 °C), anisotropic nanoparticles with AR higher than 1.4 are predominant. More intriguing is the antagonistic effect of the citrate concentration. At 95 °C, an increase of the citrate concentration leads to a decrease of the AR, while at 85 °C its increase leads to a slight AR increase. Figure 1e shows the SEM image for AuNP synthesized with conditions inside the marked region on Fig. 1c (test 2 of Table 2) and reveals the formation of highly anisotropic particles with a disc-like geometry (AuNDs).

Using a 2^4 factorial design of experiments electing four experimental factors, we found out that AuNDs can be synthesized using the Turkevich method by using a citrate:Au molar ratio of 1:1, temperatures

Fig. 2 Comparison between AuNP AR and AuND largest radii (d) divided by the average thickness (t)
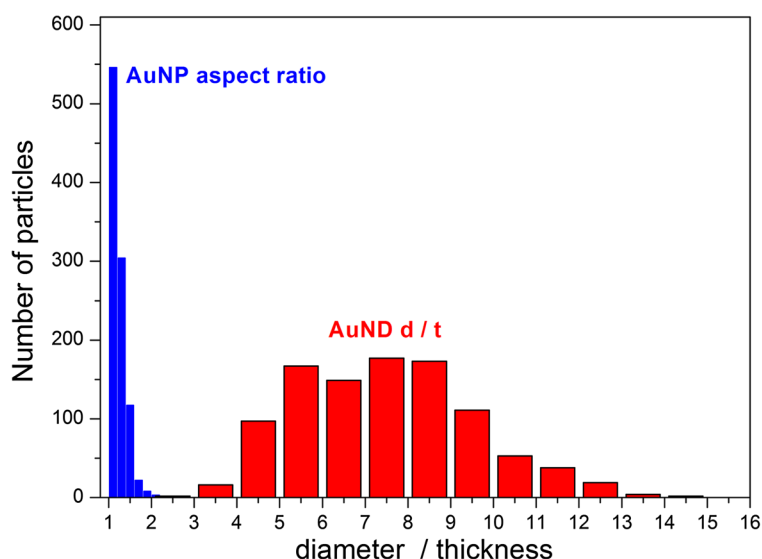
around 95 °C, and stirring rate of 900 rpm. The particles exhibit an average AR of 1.45 with sizes of 105 × 73 nm ± 20 nm, and thickness of 14 ± 4 nm (Fig. 1e). The thickness was measured in regions where the AuNDs formed a stacked arrangement exposing their lateral profiles (inset in Fig. 1e). In order to assess the selectivity in AuNDs formation, a statistical analysis bases on the SEM images was preformed and the AR for spherical AuNPs was compared with the AuNDs diameter/thickness ratio (d/t). As shown on Fig. 2 d/t varies between 4 and 13, with an average value of 7.5 ± 2.5, while the AuNP AR is close to 1. This result indicates that using Au:citrate of 1:1, 95 °C and stirring rate of 900 rpm (test 2 on Table 2), AuNDs are preferentially formed.

Formation mechanism The conventional synthetic method to make anisotropic particles is based on the use of directing agents that induces the growth of certain crystallography planes, breaking the crystal symmetry (Lohse and Murphy 2013). Citrate ions are known to be a weak complexing agents for gold atoms, due to its hard-base nature, and cannot selectively

change the surface free energy of specific crystalline planes. Thus, what is the driving force for the symmetry breaking during the formation of anisotropic gold nanoparticles in Turkevich method?

High-resolution electron microscopy (HRTEM) and selected area electron diffraction (SAED) (Fig. 3), reveal the formation of crystalline nanodiscs with face-centered cubic structure (fcc), as expected for gold nanoparticles (Elechiguerra et al. 2006). The diffraction pattern shown on Fig. 3c exhibits bright spots with sixfold symmetry, corresponding to reflections at {220} planes indicating that the crystal is oriented in the [111] direction and the AuND flat surface is parallel to the (111) plane. In fact, HRTEM images of AuNDs laying on their side (Fig. 3e) shows planes with interplanar distance of 2.38 Å, corresponding to the (111) planes, proving that the planar face is parallel to (111) planes. For the HRTEM images of AuNDs laying on their face (Fig. 3b), it can be observed that the lattice spacing is 2.55 Å, assigned to reflections at 1/3{422}, justified as 3 times the lattice spacing of the {422} planes of fcc gold crystals (Elechiguerra et al. 2006; Pastoriza-Santos and Liz-Marzan 2008). This
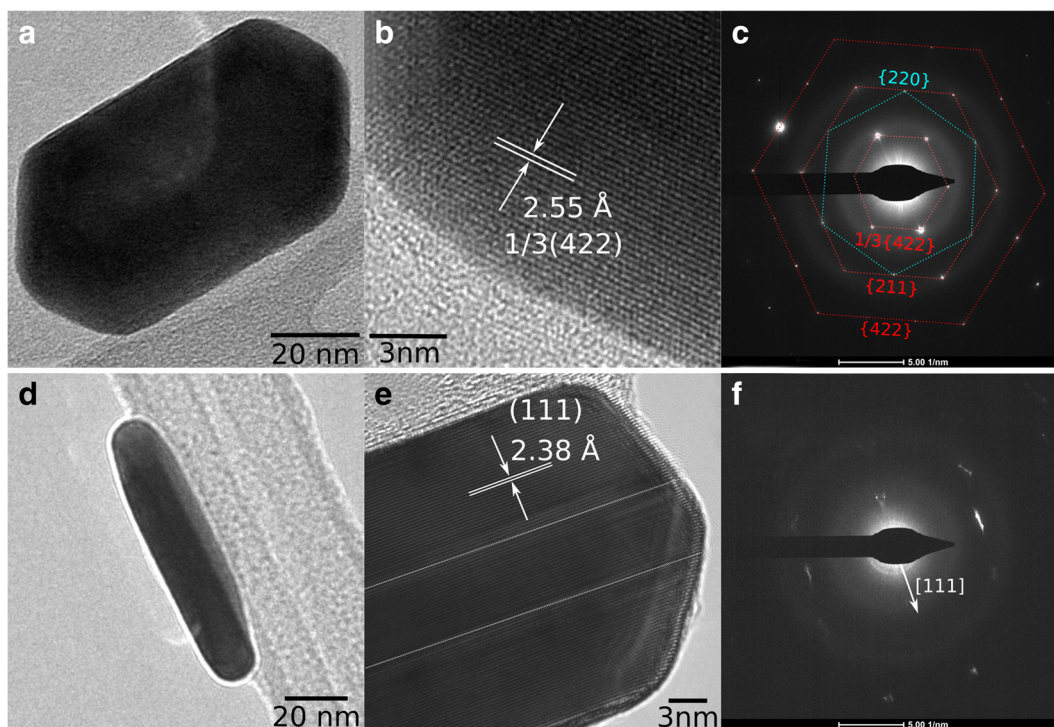
Fig. 3 **a–c** Shows the TEM, HRTEM, and SAED pattern for an AuND laying on its face. **d–f** Shows the TEM, HRTEM, and SAED pattern for an AuND laying on its side

agrees with the observation of the diffractions spots related to the 1/3{422} reflection on Fig. 3c.

Reflections at 1/3{422} are forbidden for fcc crystals and their observation can be related to the presence of dislocations or twin planes parallel to (111) planes (Elechiguerra et al. 2006; Pastoriza-Santos and Liz-Marzan 2008). Additionally, the presence of fringes in the HRTEM images with varying contrast on Fig. 3e can be explained by the visualization of the stress field in the lattice, created by the presence of dislocations or twin planes. SAED pattern of AuND laying on their side shows spots deformed from a usual circular shape to stretched and irregular spots (Fig. 3f). Dislocations change the crystal orientation locally and the diffraction spots are extended along the diffraction ring as seen in Fig. 3f (Asadabad and Eskandari 2016).

Based on the HRTEM and SAED images, the formation mechanism of AuND could be explained by the silver halide growth mechanism. Since gold has the lowest stacking fault energies among metals, the energy to form a twin plane is decreased and twins or stacking faults readily form. Because of the sixfold symmetry of the fcc system, these twinned crystals should form hexagonally-outlined nuclei that grow into rod like or hexagonal nanodiscs.

An alternative way to form stacking faults is via an oriented attachment of the particles (Leite and Ribeiro 2012). Biggs and coworkers proposed that an aggregation step can be observed just after the nucleation (Ji et al. 2007; Pei et al. 2004; Pong et al. 2007; Biggs et al. 1994). They showed by atomic force microscopy that during the nucleation step the potential barrier that stabilizes the nucleus is smaller than 20 mV and due to the adsorption of the remaining $[AuCl_4]^-$ ions, the surface forces are mainly attractive (Biggs et al. 1994). In the experimental conditions where AuNDs are formed, due to the low citrate concentration, the Au reduction reaction has a smaller yield, consequently the $[AuCl_4]^-$ concentration at the end of the nucleation step tends to be higher. At this point the $[AuCl_4]^-$ adsorption on the nucleus surfaces gives rise to attractive forces between particles, causing their aggregation. Owing to the very low citrate concentration in the nucleus electric double layer, the particles can attach irreversibly, forming anisotropic nucleus with some stacking fault. Figure S11 depicts the AuNDs temporal evolution of the extinction spectra, showing that after the nucleation, the absorbance at 900 nm increases and after a few seconds, it

decreases to the base line level. The absorption of long wavelengths can be related to the plasmon coupling between the nucleus, and after the particle attachment this band decreases. However, the experimental conditions were changed to fit limitations of our spectrophotometer. Even keeping the Au:citrate ratio at 1:1, variations on reactants concentrations, temperature and stirring rate can drastically affect the particles morphology (Fig. 1) and their growth mechanism.

These results show that changes in experimental conditions in the Turkevich method can deviate significantly the particle formation mechanism from the one recent proposed by Polte et al. (Wuithschick et al. 2015) where the burst nucleation is followed by a growth controlled by the "seed" surface to a silver halide or oriented attachment mechanism, where the formation of stacking faults is crucial for the anisotropic growth and formation of AuND.

AuND optical properties To characterize the particle optical properties, we measured the Rayleigh scattering spectra of individual particles using a dark-field optical microscope. Figure 4 depicts the hyperspectral images and scattering spectra of selected points on the images for AuNP and AuND samples. For AuNP, the majority of particles scatter green light and their scattering spectra are marked by just one band with λ_{max} between 500–600 nm (green curve on Fig. 4b and Fig. S12), assigned to the dipolar plasmonic mode (Fig. 4c). The AuNP extinction spectra measured on a particle suspension (black curve on Fig. 4b), is an average spectrum over the particle size distribution and the higher contribution of the absorption cross section is responsible for the blue shift in the extinction spectra relative to scattering spectra (Grasseschi et al. 2013, 2015b).

For the AuND sample, there are mainly two particle population: the bigger one encompasses particles with yellow-reddish color and the smaller one particles with green color. The particles on first population show three bands on the scattering spectra (Fig. 4e): one below 500 nm, that can be assigned as out-of-plane plasmonic modes (Grasseschi et al. 2015b; Hermoso et al. 2013; Pastoriza-Santos and Liz-Marzan 2008), and two other between 500–600 nm and 700–900 nm, which can be assigned to transverse and longitudinal in-plane dipolar plasmonic modes (Grasseschi et al. 2015b; Hermoso et al. 2013; Pastoriza-Santos and Liz-Marzan 2008), respectively,

80
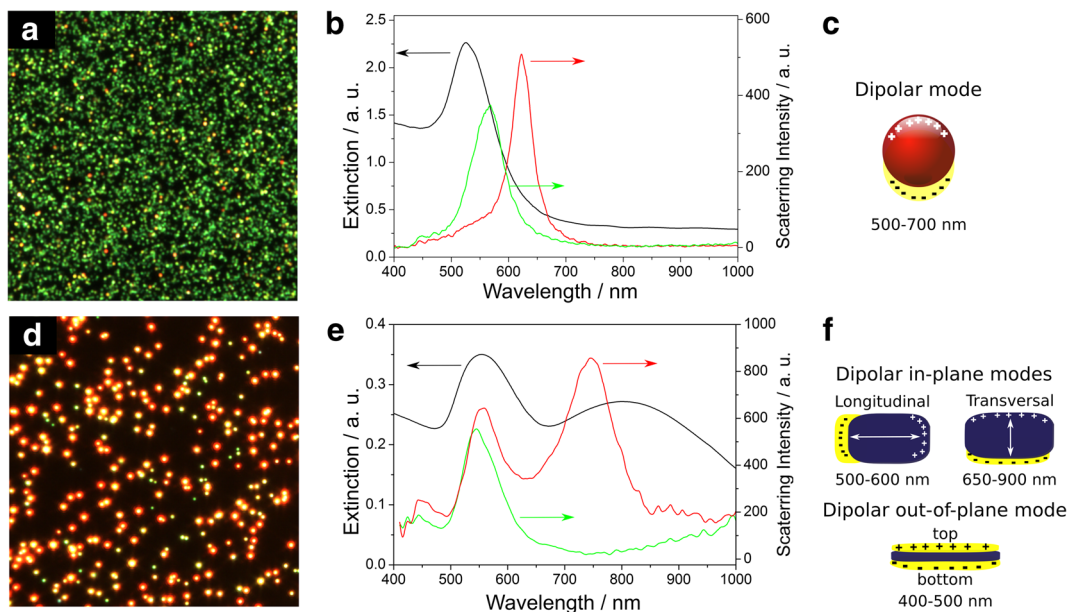
Fig. 4 AuNP hyperspetral dark-field image (**a**), extinction (black curve) and scattering spectra (green and red curves) (**b**), and schematic representation of the plasmon modes in spherical particles (**c**). AuND hyperspetral dark-field image (**d**), extinction (black curve) and scattering spectra (green and red curves) (**e**), and schematic representation of the resonance plasmon modes in nanodiscs (**f**)

as showed in Fig. 4f. The λ_{max} for longitudinal modes varies with the particle length, being red shifted for bigger particles and blue shifted for smaller ones (see Fig. S13 on the support information).

In contrast, the scattering spectra of the green particles are marked by two bands (green curve on Fig. 4e), the out-of-plane mode below 500 nm, and one in-plane mode between 550 and 700 nm, suggesting a hexagonal disc with an AR close to 1 and a thickness smaller than the other dimensions. It should be notice that the band below 500 nm is absent for spherical particles (Fig. 4b), confirming its assignment as the out-of-plane mode and proving the disc like geometry of the AuND. In Fig. 4e, the AuND extinction spectrum is also shown, and can be seen that it is an average spectrum of all particles with two broad band between 600 and 900 nm (Grasseschi et al. 2015b).

Surface ligand exchange and SERS study The synthesis of stable anisotropic nanoparticles with short aspect ratio by the Turkevich method, could facilitate their application on surface-enhanced Raman spectroscopy, for example, where stabilizer agents, such as

CTAB, generally used to obtain anisotropic nanoparticles, is a problem. The chemistry of the metal nanoparticles is essentially controlled by the surface atoms, which exhibit external orbitals available for binding donor-acceptor ligands. Interaction between the citrate ions and gold surface atoms should be governed by electrostatic interactions, since citrate has a hard-base nature (Klopman 1968; Pearson 1963). On the other hand, the coordination of bromide ions from CTAB should exhibit a greater covalent character due to its soft-base character. Then, the ligand exchange reaction in CTAB capped AuNR is expected to be slower, or even absent, than for the AuNDs.

In order to probe the AuND labile properties, 4-mercaptopyridine (4-mpy) was employed in the substitution kinetics, due to its strong affinity to gold atoms. The addition of an aqueous solution of 4-mpy (pH 6.5) (final concentration of 2.5×10^{-8} molL^{-1}) to the AuND and AuNP led to the replacement of citrate ligands with a fast kinetics, followed by particles agglomeration, giving rise to a plasmon coupling band above 900 nm for AuND and above 700 nm for AuNP (Fig. 5a). The substitution of citrate by 4-mpy on the AuND surface has a slightly slower kinetics

a

b

c
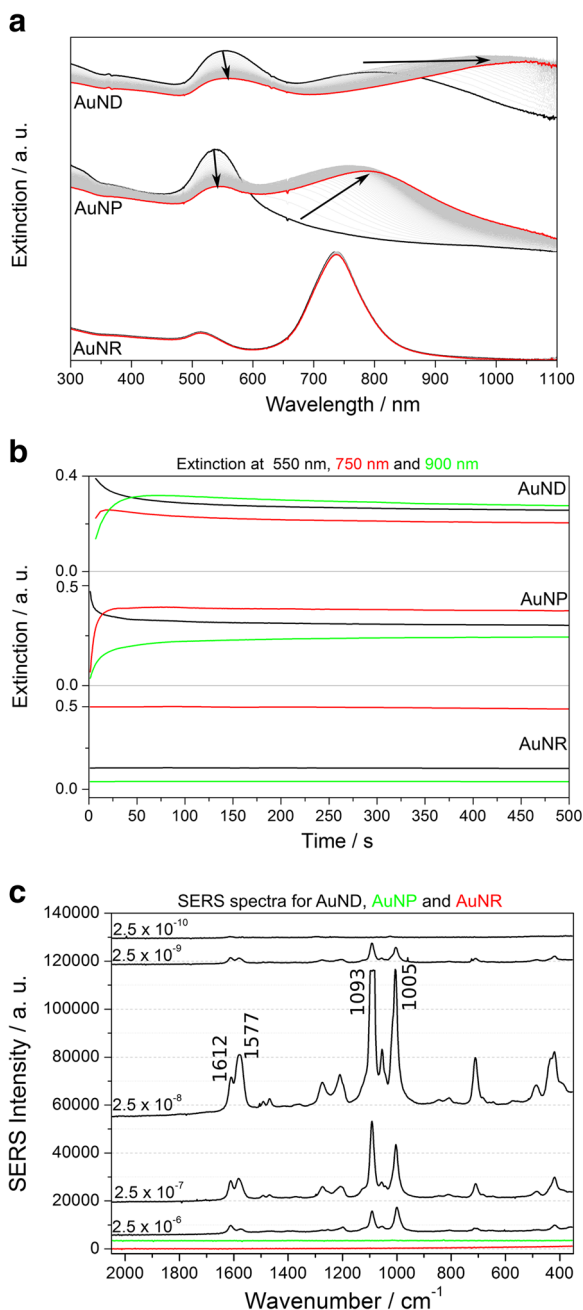
Fig. 5 a Extinction spectra time evolution, **b** aggregation kinetics for AuND, AuNP, and AuNR after addition of 4-mercaptopyridine 2.5×10^{-8} molL^{-1}. **c** SERS spectra for AuND after the addition of 4-mpy with concentration varying between 2.5×10^{-6} molL^{-1} and 2.5×10^{-10} molL^{-1} (black curves), and SERS spectra of AuNP (green curve) and AuNR (red curve) after addition of 4-mpy 2.5×10^{-8} molL^{-1}. All the SERS spectra where recorded with $\lambda_{excitation}$ of 785 nm and 120 s of integration time

than for AuNPs (Fig. 5b and Fig. S14), possibly due to the presence of dicarboxyketone, the citrate oxidation product, on the gold surface (Grasseschi et al. 2015a). In this case, dicarboxykenote has a keto-enol equilibrium which favors the formation of a AuND-enol complex involving the C=C bond of the enol group and a gold atom on the AuND surface (Grasseschi et al. 2015a).

We compared this result with AuNR synthesized by the conventional CTAB method (see note 1 on the support information). The addition of 4-mpy 2.5×10^{-8} molL^{-1} to CTAB capped AuNR produces no changes in the extinction spectra and aggregation kinetics (Fig. 5a and b bottom). Therefore, Br^- ions from CTAB have stronger interaction with the nanoparticles surfaces than citrate or dicarboxyketone, probing the more labile character of the AuND synthesized by the Turkevich method.

Figure 5c shows the SERS spectra of AuND, AuNP, and AuNR treated with 4-mpy 2.5×10^{-8} molL^{-1}. As can be seen, the AuND shows a very strong SERS response even for small 4-mpy concentrations, while AuNP and AuNR exhibit just noise. Figure 5c shows that for AuND the 4-mpy detection limit is around 2.5×10^{-9} molL^{-1}, being 100 and 1000 times higher than AuNR and AuNP, respectively (see Fig. S14). This shows that both the labile character and the lighting rod effect of AuND enables higher concentration of 4-mpy on particle surface in regions with high electric field, increasing the SERS enhancement factor.

In the SERS spectra, the high intensity peaks at 1005, 1093, and 1577 cm^{-1} indicate that 4-mpy coordination occurs via sulfur atoms with the pyridine ring perpendicular to the particle surface. The higher intensity of peak at 1577 cm^{-1} in relation to the one at 1612 cm^{-1} suggests that presence of N-protonated mpy (Nunes et al. 2006; Yu et al. 1999; Jung et al. 1997). The proportion between N-protonated and N-deprotonated changes with the 4-mpy concentration, changing the AuND aggregations dynamics (see Fig. S14 on the support information), explaining the increase in SERS intensity when the 4-mpy concentration goes from 2.5×10^{-6} to 2.5×10^{-8} molL^{-1} (Fig. 5c). The same behavior was observed for the AuNP sample in contrast with the AuNR, where the proportion of N-protonated species was higher for all concentrations.

82

These results show that the presence of citrate and/or its oxidation products on the AuND surface facilitates a further functionalization process, increasing the SERS spectra enhancement factor. In contrast, for CTAB-capped AuNR, the strong bond between bromide and gold hampers the surface ligand exchange reactions (Fig. S14).

Conclusions

By investigating the effect of experimental conditions on the size and shape of gold nanoparticle synthesized by Turkevich method, with a 2^4 factorial design, and the constructed response surfaces, we were able to identify the conditions in which anisotropic particles with disc-like geometry and short aspect ratio can be synthesized. According to the HRTEM and SAED images, the formation of stacking faults parallel to the (111) plane are the responsible for the symmetry breaking during the particles growth, suggesting that a silver halide or oriented attachment mechanism are actuating.

Unlike the conventional anisotropic nanoparticles prepared with CTAB as passivating agent, the anisotropic particles formed by Turkevich method are labile, due the presence of citrate ions, or its oxidation product on the particles' surface, and its properties can be tailored by simple ligand exchange reactions, as showed by the aggregation kinetics and SERS spectra with 4-mpy. Therefore, both labile characteristic and the lightning rod effect on AuND edges enable a higher concentration of 4-mpy on the particle surface, increasing the SERS enhancement factor 100 to 1000 times.

Compliance with Ethical Standards

Conflict of interests   The authors declare that they have no conflict of interest.

References

Asadabad MA, Eskandari MJ (2016) Electron diffraction. In: Modern electron microscopy in physical and life sciences. InTech

Biggs S, Mulvaney P, Zukoski CF, Grieser F (1994) Study of anion adsorption at the gold-aqueous solution interface by atomic force microscopy. J Am Chem Soc 116(20):9150–9157

DuChene JS, Niu W, Abendroth JM, Sun Q, Zhao W, Huo F, Wei WD (2013) Halide anions as shape-directing agents for obtaining high-quality anisotropic gold nanostructures. Chem Mater 25(8):1392–1399

Elechiguerra JL, Reyes-Gasga J, Yacaman MJ (2006) The role of twinning in shape evolution of anisotropic noble metal nanostructures. J Mater Chem 16(40):3906–3919

Ermushev AV, Mchedlishvili BV, Olenikov VA, Petukhov AV (1993) Surface enhancement of local optical fields and the lightning-rod effect. Quantum Electronics 23(5):435–440

Frens G (1973) Controlled nucleation for the regulation of the particle size in monodisperse gold suspensions. Nat Phys Sci 241(105):20–22

Gole A, Murphy CJ (2004) Seed-mediated synthesis of gold nanorods: role of the size and nature of the seed. Chem Mater 16(19):3633–3640

Grasseschi D, Zamarion VM, Araki K, Toma HE (2010) Surface enhanced raman scattering spot tests: a new insight on Feigl's analysis using gold nanoparticles. Anal Chem 82(22):9146–9149

Grasseschi D, Parussulo ALA, Zamarion VM, Guimarães RR, Araki K, Toma HE (2013) How relevant can the SERS effect in isolated nanoparticles be? RSC Adv 3(46):24465–24472

Grasseschi D, Ando RA, Toma HE, Zamarion VM (2015a) Unraveling the nature of Turkevich gold nanoparticles: the unexpected role of the dicarboxyketone species. RSC Adv 5(8):5716–5724

Grasseschi D, Lima FS, Nakamura M, Toma HE (2015b) Hyperspectral dark-field microscopy of gold nanodisks. Micron 69:15–20

Grasseschi D, Lima FS, Chaimovich H, Toma HE (2016) A critical evaluation of the role of the precursor complex and counterions in synthesis of gold nanoparticles in micellar media. arXiv:1607.00530

Gunst RF, Myers RH, Montgomery DC (1996) Response surface methodology: process and product optimization using designed experiments. Technometrics 38(3):285

Hermoso W, Alves TV, de Oliveira CC, Moriya EG, Ornellas FR, Camargo PH (2013) Triangular metal nanoprisms of Ag, Au, and Cu: modeling the influence of size, composition, and excitation wavelength on the optical properties. Chem Phys 423:142–150

Jana NLGCMR, Gearheart L, Murphy CJ (2001a) Seed-mediated growth approach for shape-controlled synthesis of spheroidal and rod-like gold nanoparticles using a surfactant template. Adv Mater 13(18):1389–1393

Jana NR, Gearheart L, Murphy CJ (2001b) Wet chemical synthesis of high aspect ratio cylindrical gold nanorods. J Phys Chem B 105(19):4065–4067

Ji X, Song X, Li J, Bai Y, Yang W, Peng X (2007) Size control of gold nanocrystals in citrate reduction: the third role of citrate. J Am Chem Soc 129(45):13939–13948

Jung HS, Kim K, Kim MS (1997) Raman spectroscopic investigation of the adsorption of 4-mercaptopyridine on a silver-sol surface. J Mol Struct 407(2-3):139–147

Kim F, Connor S, Song H, Kuykendall T, Yang P (2004) Platonic gold nanocrystals. Angew Chem (International ed. in English) 43(28):3673–3677

Kim J, Hong S, Jang H-J, Choi Y, Park S (2013) Influence of iodide ions on morphology of silver growth on gold hexagonal nanoplates. J Colloid Interface Sci 389(1): 71–76

Kimling J, Maier M, Okenve B, Kotaidis V, Ballot H, Plech A (2006) Turkevich method for gold nanoparticle synthesis revisited. J Phys Chem B 110(32):15700–15707

Klopman G (1968) Chemical reactivity and the concept of charge- and frontier-controlled reactions. J Am Chem Soc 90(2):223–234

Leite ER, Ribeiro C (2012) Crystallization and growth of colloidal nanocrystals. SpringerBriefs in Materials. Springer, New York

Lim B, Camargo PHC, Xia Y (2008) Mechanistic study of the synthesis of Au nanotadpoles, nanokites, and microplates by reducing aqueous HAuCl4 with poly(vinyl pyrrolidone). Langmuir: the ACS Journal of Surfaces and Colloids 24(18):10437–10442

Liu MZ, Guyot-Sionnest P (2005) Mechanism of silver(I)-assisted growth of gold nanorods and bipyramids. J Phys Chem B 109(47):22192–22200

Liu B, Xie J, Lee JY, Ting YP, Chen JP (2005) Optimization of high-yield biological synthesis of single-crystalline gold nanoplates. J Phys Chem B 109(32):15256–15263

Liu Z, Zu Y, Guo S (2009) Synthesis of micron-scale gold nanochains by a modified citrate reduction method. Appl Surf Sci 255(11):5827–5830

Lohse SE, Murphy CJ (2013) The quest for shape control: a history of gold nanorod synthesis. Chem Mater 25(8):1250–1261

Lohse SE, Burrows ND, Scarabelli L, Liz-Marzán LM, Murphy CJ (2014) Anisotropic noble metal nanocrystal growth: the role of halides. Chem Mater 26(1):34–43

Mezni A, Dammak T, Fkiri A, Mlayah A, Abid Y, Smiri LS (2014) Photochemistry at the surface of gold nanoprisms from surface-enhanced raman scattering blinking. J Phys Chem C 118(31):17956–17967

Murphy CJ, Jana NR (2002) Controlling the aspect ratio of inorganic nanorods and nanowires. Adv Mater 14(1):80–82

Nikoobakht B, El-Sayed MA (2003) Preparation and growth mechanism of gold nanorods (NRs) using seed-mediated growth method. Chem Mater 15(10):1957–1962

Nunes FS, Bonifácio LDS, Araki K, Toma HE (2006) Interaction of 2- and 4-Mercaptopyridine with Pentacyanoferrates and gold nanoparticles. Inorg Chem 45(1):94–101

Ogi T, Saitoh N, Nomura T, Konishi Y (2009) Room-temperature synthesis of gold nanoparticles and nanoplates using Shewanella algae cell extract. J Nanopart Res 12(7): 2531–2539

Ojea-Jiménez I, Campanera JM (2012) Molecular modeling of the reduction mechanism in the citrate-mediated synthesis of gold nanoparticles. J Phys Chem C 116(44):23682–23691

Pan H, Low S, Weerasuriya N, Shon Y-S (2015) Graphene oxide-promoted reshaping and coarsening of gold nanorods and nanoparticles. ACS Appl Mater Interfaces 7(5):3406–3413

Pastoriza-Santos I, Liz-Marzan LM (2008) Colloidal silver nanoplates. State of the art and future challenges. J Mater Chem 18(15):1724

Pearson RG (1963) Hard and soft acids and bases. J Am Chem Soc 85(22):3533–3539

Pei L, Mori K, Adachi M (2004) Formation process of two-dimensional networked gold nanowires by citrate reduction of AuCl4- and the shape stabilization. Langmuir 20(18):7837–7843

Personick MLM, Mirkin CCA (2013) Making sense of the mayhem behind shape control in the synthesis of gold nanoparticles. J Am Chem Soc 135(49):18238–47

Pong B-K, Elim HI, Chong J-X, Ji W, Trout BL, Lee J-Y (2007) New insights on the nanoparticle growth mechanism in the citrate reduction of gold(III) salt: formation of the Au nanowire intermediate and its nonlinear optical properties. J Phys Chem C 111(17):6281–6287

Shankar SS, Rai A, Ankamwar B, Singh A, Ahmad A, Sastry M (2004) Biological synthesis of triangular gold nanoprisms. Nat Mater 3(7):482–488

Shankar SS, Rai A, Ahmad A, Sastry M (2005) Controlling the optical properties of lemongrass extract synthesized gold nanotriangles and potential application in infrared-absorbing optical coatings. Chem Mater 17(3):566–572

Stewart ME, Anderton CR, Thompson LB, Maria J, Gray SK, Rogers JA, Nuzzo RG (2008) Nanostructured plasmonic sensors. Chem Rev 108(2):494–521

Toma HE, Zamarion VM, Toma SH, Araki K (2010) The coordination chemistry at gold nanoparticles. J Braz Chem Soc 21(7):1158–1176

Turkevich J (1985a) Colloidal gold. Part I. Gold Bull 18:86–91

Turkevich J (1985b) Colloidal gold. Part II. Gold Bull 18:125–131

Turkevich J, Stevenson PPC, Hillier J (1951) A study of the nucleation and growth processes in the synthesis of colloidal gold. Discuss Faraday Soc 11:55–75

Turkevich J, Stevenson PC, Hillier J (1953) The formation of colloidal gold. J Phys Chem 57(7):670–673

Vainrub A, Pustovyy O, Vodyanoy V (2006) Resolution of 90 nm (λ/5) in an optical transmission microscope with an annular condenser. Opt Lett 31(19):2855

Vianna PG, Grasseschi D, Costa GKB, Carvalho ICS, Domingues SH, Fontana J, de Matos CJS (2016) Graphene oxide/gold nanorod nanocomposite for stable surface-enhanced raman spectroscopy. ACS Photonics 3(6):1027–1035

Wang Z, Ma L (2009) Gold nanoparticle probes. Coord Chem Rev 253(11-12):1607–1618

Wuithschick M, Birnbaum A, Witte S, Sztucki M, Vainio U, Pinna N, Rademann K, Emmerling F, Kraehnert R, Polte J (2015) Turkevich in new robes: key questions answered for

the most common gold nanoparticle synthesis. ACS Nano 9(7):7052–7071

Xiong Y, Washio I, Chen J, Cai H, Li Z-Y, Xia Y (2006) Poly(vinyl pyrrolidone): a dual functional reductant and stabilizer for the facile synthesis of noble metal nanoplates in aqueous solutions. Langmuir 22(20):8563–8570

Yu HZ, Xia N, Liu ZF (1999) SERS titration of 4-Mercaptopyridine self-assembled monolayers at aqueous buffer/gold interfaces. Anal Chem 71(7):1354–8

Zamarion VM, Timm RA, Araki K, Toma HE (2008) Ultrasensitive SERS nanoprobes for hazardous metal ions based on trimercaptotriazine-modified gold nanoparticles. Inorg Chem 47(8):2934–2936

Gold Nanoparticle Conjugation with Microtubules for Nanobiostructure Formation

Daniel Oliveira, Jorge D. Shinohara, and Henrique E. Toma*

Instituto de Química, Universidade de São Paulo, São Paulo-SP, 05508-000, Brazil

The use of naturally occurring biomolecules as templates for the design and formation of hybrid nanostructures is highly attractive, since it combines the unique electronic and optical properties of nanoparticles with the controllable physical support provided by biomolecules. Here, microtubules were investigated as templates for the formation of gold nanoparticles-decorated linear structures. The binding of synthesized gold nanoparticles to the microtubules surface was monitored by Cytoviva™ dark field hyperspectral microscopy and studied by means of the surface plasmon resonance (SPR) technique. The interaction with specific amino acids in the binding sites were probed by surface enhanced Raman spectroscopy (SERS). In addition to the expected gold-thiol bonds between cysteine and methionine on the microtubule's surface atoms, the gold nanoparticles also bind to microtubules through the imidazole functional group of exposed histidine amino acids and to the indole group of available tryptophan residues.

Keywords: Microtubule, Gold Nanoparticle, Bioconjugation, Binding Interaction, SERS.

1. INTRODUCTION

In order to better understand biological processes at the nanoscale level, nanoparticles and nanomaterials are arguably considered the most efficient probes capable of monitoring the cellular machinery of the cell.[1] In fact, knowledge of such biomolecular systems is one of the main incentives behind the advancement of nanotechnology.

Due to their attractive optical and electric properties[2] gold nanoparticles have found extensively applications in chemical and biological systems.[3] Gold nanoparticles have been employed as contrasting agents,[4–6] as delivery vehicle,[7,8] as sensitive sensors,[9,10] and lately there is a lot of attention on the use of gold nanoparticles to detect and sequence DNA strands.[11,12] The ever-growing interest on gold nanoparticle-based research is mainly due to their very high extinction coefficient and photostability, straightforward synthetic routes, uncomplicated functionalization and surface plasmon resonance effect. Particularly interesting to nanobiological systems is its high biocompatibility coupled with low cytotoxicity.[13,14]

There is also enthusiasm in using biological systems as templates in the synthesis, self-assembly and formation of nanoparticles and specially nanosized structures with well-defined size, geometry and configuration. Gold nanoparticles nanoscale structures were in fact previously achieved using several templates such as viruses,[15] bacteria,[16–18] fungus,[19] and DNA strands.[20,21] The greatest advantage of using biotemplates in order to create organized nanosized systems is the simplicity in the formation of the desired structure as it can rely on the straightforward physical adsorption of nanoparticles onto biological structures. With that in mind, microtubules are sought as highly attractive biological materials for biotemplating.

Microtubules are naturally occurring, filamentous fibers made up of α- and β-tubulin globular protein monomers. Tubulin polymerizes yielding relatively straight hollow tubes with an outer diameter of approximately 25 nm and tens of micrometer in length.[22,23] They provide cytoskeletal filaments which play essential roles in eukaryotic cells, transporting intracellular cargoes, and are responsible for the cell motility, including muscle contraction. Microtubule malfunctioning and instability in the cell's cytoskeleton have been previously associated with Alzheimer's disease and cancer.[24] Such cytoskeletal filaments have been of great interest for nanotechnological applications, such as in miniaturized sensors and lab-on-a-chip devices. For this purpose, the microtubules are being modified by chemical or genetic engineering procedures in order to conjugate with fluorophores, antibodies, oligonucleotides or nanoparticles.[25]

Since microtubules are polymers of the tubulin protein, there are several amino acids moieties present on its outer surface, and consequently several functional groups that

could potentially be used for nanoparticle binding. It was already reported the binding of several nanosized materials to the surface of microtubule, including Ag,[26] Co,[27] Ni[28] and Pd.[26] The binding of such particles to microtubules shows that such biomolecules can be employed to direct the spatial arrangement and consequently, the formation of peculiar nanostructures, especially nanoarrays.

By incubating nanoparticles with microtubules, it is possible to decorate the surface of the biomolecules with nanoparticles, yielding filamentous metallic arrays. Zhou and coworkers studied the design and assembly of gold nanowires through templates of gold-decorated microtubules.[29] By irradiating previously polymerized microtubules with UV radiation in the presence of HAuCl$_4$ and Triton X-100 surfactant, they were able to photochemically decorate microtubules with gold nanoparticles. Currently, it is unclear whether microtubules are sensitive to UV radiation and whether radiation contributes to loss of filament structure.[30] Since tubulin absorbs maxima at 280 nm,[31] and such studies were performed applying UV radiation at 254 nm, it is possible that UV radiation might affect the structure of native microtubules. With that in mind, it is clear the need for better insights into the interaction of nanoparticles and native microtubules, especially given its vast potential as biotemplates for the development of nanoarrays.

The binding sites involved in the interaction of the gold nanoparticles generated in the presence of microtubule have also been investigated by Zhou et al.[32] They considered that the histidine moieties located on the microtubule's outer surface is acting as the main functional group responsible for gold coordination, in agreement with the literature.[33, 34]

In this study, we focused on the direct interaction of gold nanoparticles with the microtubule biomolecule, instead of generating such nanostructures *in situ*, as reported before.[29, 32] The Cytoviva™ hyperspectral system was used to visualize the interaction between nanosized materials and biomolecules that were individually prepared and incubated over a period of time. Furthermore, the surface enhanced Raman spectroscopy (SERS) technique was used to investigate the binding sites of such interactions. It seems that several functional groups contribute to the binding of gold to microtubules, the most prominent amino acids processing these groups being histidine, tryptophan, cysteine and methionine.

2. EXPERIMENTAL DETAILS

2.1. Chemicals
Lyophilized porcine brain tubulin was purchased from Cytoskeleton. Ethylene glycol bis(2-aminoethylether)-N,N,N',N'-tetraacetic acid (EGTA), piperazine-N,N''-bis(2-ethanesulfonic acid) (PIPES), magnesium chloride (1 M), glycerol, paclitaxel (taxol), polysorbate 20 (Tween 20), guanosine 5'-triphosphate (GTP), HAuCl$_4$, and

sodium citrate were purchased from Sigma-Aldrich. Glycine-HCl (10 nM, pH 1.5), NaOH (50 mM), 1-ethyl-3-(3-dimethylpropyl)-carbodiimide (EDC), N-hydroxy-succinimide (NHS) and ethanolamine were purchased from BIAcore.

2.2. Microtubules Preparation
Porcine tubulin protein was prepared to a final concentration of 50 μM in BRB80 buffer (80 mM PIPES, 1 mM EGTA, 1 mM MgCl$_2$, pH 6.9) containing GTP (1 μM) and 5% glycerol, aliquoted and stored at −80 °C. A fresh tubulin aliquot was thawed at 37 °C and allowed to polymerize for 30 minutes, followed by dilution to 0.5 μM with warm BRB80 buffer supplemented with 20 μM taxol as stabilizing agent.

2.3. Gold Nanoparticle Synthesis and Conjugation
Suspension of gold nanoparticles in water was prepared following a previously described method.[35] Briefly, a HAuCl$_4$ (0.03% m/v) solution in water was heated until boiling, followed by the addition of a sodium citrate solution (1% m/v) water solution under vigorous stirring. The method produced gold nanoparticles with average size of 20 nm (DLS). After polymerization, microtubules (20 μL) were incubated with the prepared gold nanoparticle suspension (2 μL) for 30 minutes before experiments were initiated allowing for formation of the microtubule-gold nanoparticle conjugate.

2.4. Surface Plasmon Resonance (SPR) Measurement
Binding events of kinesin to microtubules were monitored in real-time using a BIAcore™ T200 instrument. All experiments were performed at 25 °C using a running solution of BRB80 supplemented with Tween 20 (0.005%) at a flow rate of 10 μL/min. The C1 sensor chip was used as part of this study. Polymerized tubulin (0.5 μM) in BRB80 buffer was covalently coupled onto the second channel of the sensor chip by carbodiimide coupling to amine groups using NHS/EDC. Following immobilization, ethanolamine was injected over the sensor's surface in order to deactivate excessive reactive groups. The sensor chip's first channel was used for reference and thus treated similarly to the second channel except that no polymerized tubulin was immobilized on its surface. Gold nanoparticles was injected over immobilized microtubules and control surfaces to test for binding. Following SPR sensorgram acquisition, data was normalized by subtracting the response from the reference channel.

2.5. Dark-Field Microscopy Measurement
Dark-field microscopy was performed with the aid of the Cytoviva™ 150 hypermicroscope system equipped with a Xe 75 W light source, and a 100×/1.30 oil lens. Tubulin was polymerized and conjugated as previous described, placed into a flow cell and imaged at the microscope.

The employed flow cell consisted of a coverslip mounted on top of a microscope glass slide using two pieces of double-sided scotch tape. Once solutions are injected onto the chamber, the flow cell exposed ends are capped with nail polish to prevent evaporation.

2.6. Surface Enhanced Raman Spectroscopy (SERS) Measurement

SERS experiments were made using a WITec alpha-300R confocal Raman microscope. The Raman spectrum was obtained using a Nd:YAG laser with excitation wavelength of 532 nm and a laser power output of 8 mw/cm^2, using a Nikon 100× 0.8 NA objective. Tubulin was polymerized and conjugated as previous described; a drop of the conjugate was placed on a glass slide and imaged at the microscope.

3. RESULTS AND DISCUSSION

The transmission electron microscopy (TEM) image shown in Figure 1. Shows spherical gold nanoparticles with an average core diameter of 15 ± 5 nm and interplanar (111) distances of 2.37 Å compatible with gold nanocrystals. The well-researched surface plasmon resonance effect[35, 36] which causes metallic nanoparticles to enhance their light scattering and absorption patterns, makes gold nanoparticles particularly suited for dark-field microscopy visualization and analysis. The reason for such statement is because the increased light scattering in gold nanoparticles induces an amplification response, which in turn makes it possible for single-particle optical detection.[37]

In Figure 2 it is shown a dark-field microscope image of a single microtubule conjugated with 20-nm gold nanoparticles. The image was acquired on a Cytoviva™ hyperspectral dark-field microscope using a 100×/1.30 NA oil-immersion objective. Microtubules were polymerized from tubulin as previously stated and incubated at a 1:10 ratio (gold nanoparticle: microtubule, v/v) for 30 min. The mixture was injected into a previously prepared flow-cell
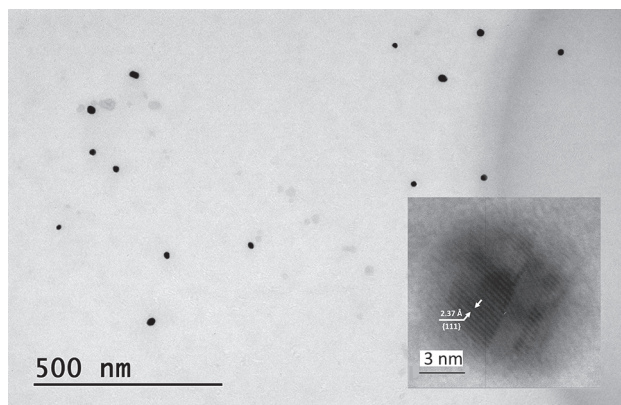
Fig. 1. TEM micrograph of the synthesized gold nanoparticles employed for microtubule bioconjugation (inset—High resolution spot, showing the 111 interplanar distances).
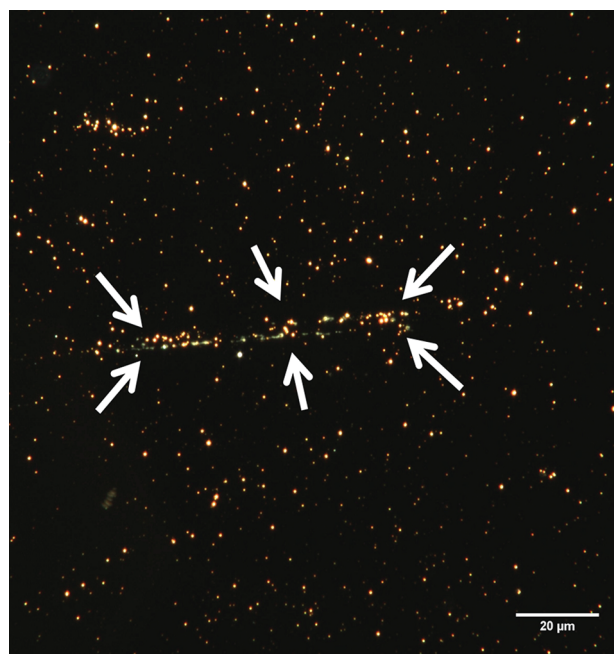
Fig. 2. Hyperspectral image acquired with the Cytoviva™ instrument of a single microtubule incubated with gold nanoparticles (scale bar is 20 μm). Arrows were inserted in the figure in order to better display the decorated microtubule.

(see the experimental details for flow-cell details) and placed on the focus of the dark-field microscope for observation. The approximate 70 μm length microtubule is decorated with gold nanoparticles bound to the surface through diverse functional groups, which will be addressed later on this report. White arrows were inserted in the figure to facilitate microtubule observation.

Although Figure 2 indicates the binding of gold nanoparticles to a microtubule template, the gold material does not uniformly cover the biomolecule's surface. Additional experiments were conducted aiming to induce denser coverage of the microtubule by increasing microtubule-nanoparticle incubation time for up to 12 hours but no discernable effect could be observed (data not shown). Nevertheless, data displayed in Figure 2 clearly demonstrates that by simply incubating gold nanoparticles in the presence of microtubules, it is possible to observe their biomolecular binding interaction. Furthermore, synthesized gold nanoparticles could be readily visualized using transmission dark-field microscopy.

Since the dark-field collected image is indicating the binding of the gold nanoparticles to the microtubule filament, the process was further investigated by monitoring the real-time binding events of gold nanoparticles to microtubules using the surface plasmon resonance (SPR) technique. SPR has been widely employed[38, 39] to study the dynamic binding behavior between a moving analyte to its binding partner which is immobilized onto a given surface. The appealing power from using such technique stems from the fact that both binding partners can be analyzed

without any requirement to label them. Moreover, both the binding and dissociation events from the binding interaction can be monitored on-time.[40]

The interaction between gold nanoparticles and microtubules was monitored using a BIAcore™ T200 instrument. The C1 sensor chip, which has a flat carboxylated surface, was used in the studies. Other sensor chips bearing a dextran layer could not be used as the presence of such matrix would evidently hinder access of microtubules to the active sites present within the dextran layer. Thus, the carboxylated surface of the C1 sensor chip was activated using NHS/EDC chemistry and polymerized microtubules were immobilized to the sensor's surface through the free amine groups located on the microtubules' surface via carbodiimide coupling. All species flowing through the instrument were injected at 25 °C using a flow rate of 10 μL/min and a running buffer of BRB80 with added Tween 20 (0.005%). Microtubules were immobilized on the C1 sensor surface with a response level of 350 RUs. Following microtubule immobilization, gold nanoparticles were injected onto the C1 sensor chip surface to monitor their specific binding interaction.

A real-time binding profile, known as a sensorgram, of gold nanoparticles flowing over 2 separate channels of the BIAcore™ C1 sensor chip can be seen in Figure 3(A). It is shown the channel where no microtubule was immobilized over the sensor's surface, i.e., the reference channel (dashed line); and over the channel where microtubules were previously immobilized onto the surface of the sensor (solid line). The dashed line in the figure shows that even though no binding between gold nanoparticles and the surface with any microtubules was expected, some binding interaction between the injected nanomaterial and such surface was observed. This non-specific binding is thought to be due the high hydrophilic nature of the C1 sensor chip. This particular sensor surface, which does not contain the

widely employed dextran layer, is believed to be considerably hydrophobic. In turn it leads to higher probabilities of non-specific binding events between the monitored analyte and the sensor surface via hydrophobic interactions.[41] Tween 20 (0.005% v/v) was added to the flowing buffer as this non-ionic surfactant is known to disrupt hydrophobic interactions, which were indeed significantly greater when no surfactant was added (data not shown).

Nevertheless, the presence of such non-specific binding is unquestionably lower than the observed binding interactions between gold nanoparticles and the microtubule-covered surface (solid line in Fig. 3(A)). It is clear from the displayed graph that gold nanoparticles significantly bind to immobilized microtubules, which is more evidently observed when the reference channel (dashed line) is subtracted from the working channel (solid line). Figure 3(B) shows the association and dissociation phases for the gold nanoparticles/microtubules interaction after reference channel subtraction.

It can be seen in Figure 3(B) that from 30 to 210 seconds there is a continuous binding interaction between free-flowing gold nanoparticles and immobilized microtubule filaments along the duration of the nanosized material injection, i.e., 3 minutes. After the injection of gold nanoparticles was concluded (at 210 seconds), by running a buffer solution through the system the dissociation of the bound gold nanoparticles was expected to occur. Surprisingly, however, this dissociation process was not observed, suggesting the involvement of factors such as strong avidity and re-binding processes. As previously stated, microtubule polymers are considerable lengthy (several micrometers), providing several sites for binding interactions with flowing gold nanoparticles. Microtubules' binding sites are believed to involve functional groups from different amino acids present on the outer surface of the filament; therefore, several binding sites are available at a given time. It is possible that as a consequence of the
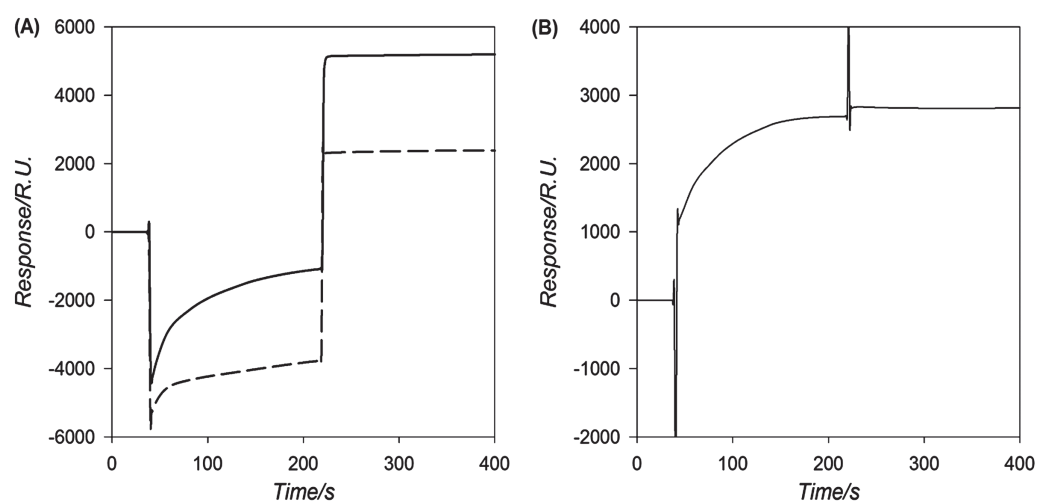
Fig. 3. Real-time SPR sensorgrams displaying the binding interactions of gold nanoparticles with: (A) no immobilized species, i.e., negative control (dashed line), and taxol-stabilized microtubules (0.5 μM) (solid line), and (B) differential sensorgram (dashed line subtracted from solid line in (A)).

avidity effect, gold nanoparticles are not being diffused away from the surface of microtubules since another binding event is likely to occur, provoking re-binding of the nanoparticle to the biomolecule.

It should also be stated here that mass transport limitations could also be involved in the apparent lack of dissociation on the observed sensorgram. In surface plasmon resonance experiments, mass transport can arise if the diffusion rate of free-flowing analyte from the bulk is slower than the association rate generated with its binding partner. Such effect is specially seen in fast binding reactions, since diffusion limits the association rate.[42] The steep rise in the measured SPR signal observed in the solid line on Figure 3(A) seems to suggest the binding of gold nanoparticles to microtubules is taken place under relatively fast rates, which in turn could potentially suggest the presence of mass transport in the binding interaction. If indeed mass transport issues are occurring during the dynamic interaction between microtubule and gold nanoparticles, one would expect re-binding events to also occur, indicating a complex binding interaction where avidity and mass transport limitations could be causing analyte re-binding to the sensor's chip surface.

Another critical factor impacting the lack of dissociation of gold nanoparticles from the microtubule surface might be due to the specific binding interaction between the two species. Nogales et al.[42] were able to obtain the crystallographic data for the $\alpha\beta$-tubulin dimer, generating a high-resolution model for microtubules, where the specific position of amino acids moieties was established.[22] It was shown that a small number of methionine and cysteine moieties are located on the outer surface of the microtubule. Even though such residues are not located at readily accessible sites at the outer surface, they nevertheless represent available sites were interaction with another species have the potential to occur. Since methionine and cysteine both contain sulfur atoms on their side chains, there is the possibility of a widely studied binding interaction: the strong covalent bond formation between gold and sulfur atoms, namely, the gold-thiol bond.[43, 44]

Below, the report the binding nature between microtubule and gold nanoparticle will be addressed thoroughly relaying on Raman spectroscopy studies, where specific amino acids' functional groups involved in binding interaction process are identified.[45] Here, it suffices to say that the event observed in Figure 3(B), e.g., the apparent lack of dissociation of gold nanoparticles to microtubules, might be a result of the formation of gold-thiol bonds. The formation of such bonds, which have been described as "semi-covalent," meaning they are believed to be part covalent and part electrostatic,[46] would certainly explain why there is no decrease in the measure SPR signal once the injection of gold nanoparticles is terminated, as the formed partially covalent bond between gold and sulfur would not allow for free dissociation of gold nanoparticles onto solution.

As previously stated, microtubules were polymerized from raw, unlabeled tubulin by thawing a fresh tubulin aliquot at 37 °C and allowing it to polymerize for 30 minutes, followed by dilution to 0.5 μM with warm BRB80 buffer supplemented with 20 μM taxol. After polymerization, 20 μL of microtubules was incubated with 2 μL of prepared gold nanoparticle suspension for 30 min, followed by placing a single drop of the conjugate onto a glass slide, and measuring its Raman spectrum on a WITec alpha-300R confocal Raman microscope. The Raman spectrum was obtained using a Nd:YAG laser with excitation wavelength of 532 nm and a laser power output of 8 mw/cm^2, using a Nikon 100× 0.8 NA objective.

In Figure 4 one can see the measured Raman spectrum for the microtubule and gold nanoparticle conjugate. Before assigning the functional groups on the microtubules' surface which are believed to be binding to gold, it is necessary to discuss which amino acids are present on the microtubule's outer surface. It was already stated the presence of cysteine and methionine residues. Aside from those, the most prominent amino acid
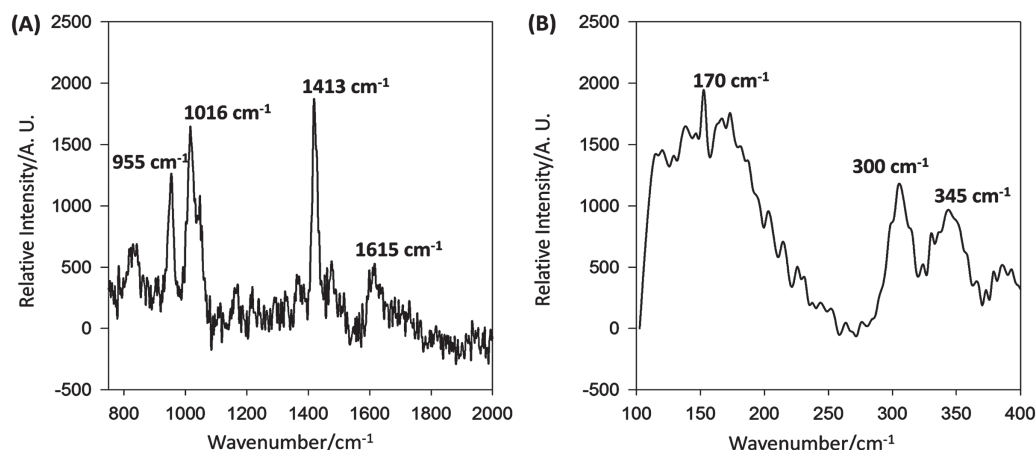

Fig. 4. Raman spectra of the microtubule-gold nanoparticle conjugate at two distinct spectral ranges (A) 750 to 2000 cm^{-1}, and (B) 100 to 400 cm^{-1}.

on the biomolecule's surface is histidine. The imidazole-containing amino acid is the easiest accessible residue for binding since it is centrally located on the tubulin surface.[42] In fact, the binding of histidine through the coordination of imidazole to gold-containing biological species have been previously studied, it is believed that the imidazole ring coordinates to gold atoms through its deprotonated N3 atom.[45] Tryptophan amino acids are also situated on the microtubule's external surface, providing another site for interaction with gold nanoparticles. It has been reported that tryptophan binds to gold nanoparticles through interaction with both tryptophan's indole and the carboxyl functional groups, being also suggested that the conjugate is further stabilized through specialized π electron interaction from the indole group.[46] There are thus, four externally-located amino acids at the surface of microtubules which capable of providing discrete binding sites for gold nanoparticle interaction via their functional groups, namely, cysteine, methionine, histidine and tryptophan.

Here, Raman spectroscopy was employed to determine specific functional groups of amino acids present on the microtubule, which are involved in interactions with gold nanoparticles. More specific, surface Raman enhanced spectroscopy (SERS) is particularly suited in analyzing the interface between gold nanoparticles and biomolecules as a consequence of the enhancement of the molecular vibration modes characteristic of the SERS technique.[35] Figure 4(A) shows the acquired Raman spectrum of the gold nanoparticle-microtubule conjugate displayed from 750 to 2000 cm^{-1}. From the Raman data displayed in Figure 4(A) it seems that the tryptophan residue is likely involved in the binding with gold, since the bands at 1016 cm^{-1} (assigned to the symmetric benzene and pyrrole breathing mode)[47] and at 1615 cm^{-1} (assigned to the C2–C3 pyrrole stretching mode)[48] indicates the close proximity of tryptophan to gold nanoparticles. Moreover, the presence of histidine involved in gold binding is also indicated in Figure 4(A), as the most intense band in the SERS spectrum at 1413 cm^{-1} is assigned to the N–C–N symmetric stretch of the protonated imidazole ring of histidine.[49]

Since it was proposed[50] that the Au–S interface might be playing an important role in the bioconjugate formation, special attention will be given to the vibrations of the Au–S, which lies below about 350 cm^{-1}.

Figure 4(B) displays the same Raman spectrum obtained at the region between 100 and 400 cm^{-1}. The three relevant peaks of the gold nanoparticle-microtubule conjugate displayed in Figure 4(B) can be observed at 170, 300 and 345 cm^{-1}. All three peaks have been associated with the vibrations of the Au–S interface. Bürgi assigned different types of Au–S vibrations that closely relate to the vibrations observed here. Namely, he assigned the Au–S–C bending modes around 180 cm^{-1}, and Au–S stretching modes around 220–280 cm^{-1}, and also around 320 cm^{-1}

and above.[51] These 3 assigned vibrations modes of the Au–S interface are notably close to the values reported here, indicating gold nanoparticles seems to be coupled to the surface of microtubules through thiol bonds.

The proposed assignments cannot be taken under strict conditions, since the binding modes of the amino acids to the gold nanoparticles do not correspond exactly to those involved in the interaction with the specific imidazole, thiol (cysteine), thioether (methionine) and tryptophan residues on the microtubules, and conformational changes have been neglected. Although cysteine is not a good SERS probe, its binding can put the gold nanoparticles very close to the existing imidazole and tryptophan residues. Therefore, the observed Raman spectrum seems to reflect the presence of the tryptophan, and perhaps methionine and histidine residues close to the gold nanoparticles.

Recently, tryptone-stabilized gold nanoparticles have been reported to induce a tubulin-targeted antiproliferative mechanism of human pancreatic (PANC-1), cervical (HeLa) and breast (MDA-MB-231) cancer cells.[52] The attached gold nanoparticles seem to inhibit cell viability by disrupting the dynamicity of the cellular microtubules. This result calls the attention for the importance of understanding the molecular mechanisms involved, starting from the nature of the tubulin-gold nanoparticles conjugates and their molecular binding modes, as discussed in this work.

4. CONCLUSION

Dark-field optical microscopy successfully allowed to detect a linear hybrid composite of gold nanoparticles bound to microtubule, by exciting the corresponding plasmonic resonance in the visible. By means of the surface plasmon resonance technique, the occurrence of specific binding between gold nanoparticles and the microtubules has been characterized in aqueous solution. On the other hand, by applying confocal Raman spectroscopy in the investigation of the specific binding sites participating in the gold nanoparticle-microtubule interaction, it was proposed the formation of gold-sulfur bond between gold nanoparticles and microtubule, in addition to the possible contribution of the tryptophan and histidine amino acid residues in the binding process. Even though it was possible to demonstrate that microtubules can be decorated with gold nanoparticles by a straightforward incubation step, the drawback is that the microtubules could not yet be densely and evenly covered with gold nanoparticles.

References and Notes

1. R. Villanuva, D. Ganta, and D. A. Molina, *J. Bionanoscience* 11, 461 (**2017**).
2. M.-C. Daniel and D. Astruc, *Chem. Rev.* 104, 293 (**2004**).
3. M. Hashimoto, H. Kawakami, K. Kawai, and S. Imazato, *Journals Biomater. Tissue Engineeering* 7, 139 (**2017**).
4. J. Kim, P. Chhour, J. Hsu, H. I. Litt, V. A. Ferrari, R. Popovtzer, and D. P. Cormode, *Bioconjug. Chem.* 28, 1581 (**2017**).
5. J. Weber, P. C. Beard, and S. E. Bohndiek, *Nat. Methods* 13, 639 (**2016**).
6. Y. Jin, C. Jia, S.-W. Huang, M. O'Donnell, and X. Gao, *Nat. Commun.* 1, 41 (**2010**).
7. R. Raliya, D. Saha, T. S. Chadha, B. Raman, and P. Biswas, *Sci. Rep.* 7 (**2017**).
8. T. Cui, J.-J. Liang, H. Chen, D.-D. Geng, L. Jiao, J.-Y. Yang, H. Qian, C. Zhang, and Y. Ding, *ACS Appl. Mater. Interfaces* 9, 8569 (**2017**).
9. K. M. Mayer and J. H. Hafner, *Chem. Rev.* 111, 3828 (**2011**).
10. A. Y. Chen, Z. Deng, A. N. Billings, U. O. S. Seker, M. Y. Lu, R. J. Citorik, B. Zakeri, and T. K. Lu, *Nat. Mater.* 13, 515 (**2014**).
11. P. Valentini and P. P. Pompa, *Angew. Chemie-International Ed.* 55, 2157 (**2016**).
12. J. Zheng, P. E. Constantinou, C. Micheel, A. P. Alivisatos, R. A. Kiehl, and N. C. Seeman, *Nano Lett.* 6, 1502 (**2006**).
13. S. J. Soenen, B. Manshian, J. M. Montenegro, F. Amin, B. Meermann, T. Thiron, M. Cornelissen, F. Vanhaecke, S. Doak, W. J. Parak, S. De Smedt, and K. Braeckmans, *ACS Nano* 6, 5767 (**2012**).
14. A. M. Alkilany and C. J. Murphy, *J. Nanoparticle Res.* 12, 2313 (**2010**).
15. A. A. Khan, E. K. Fox, M. L. Gorzny, E. Nikulina, D. F. Brougham, C. Wege, and A. M. Bittner, *Langmuir* 29, 2094 (**2013**).
16. S. He, Z. Guo, Y. Zhang, S. Zhang, J. Wang, and N. Gu, *Mater. Lett.* 61, 3984 (**2007**).
17. C. Ashajyothi and R. K. Chandrakanth, *J. Bionanoscience* 8, 255 (**2014**).
18. S. Biglari, G. H. S. Bonjar, and G. R. S. Sirchi, *J. Bionanoscience* 8, 39 (**2014**).
19. A. Mishra, S. K. Tripathy, and S.-I. Yun, *Process Biochem.* 47, 701 (**2012**).
20. Q. Gu, C. D. Cheng, R. Gonela, S. Suryanarayanan, S. Anabathula, K. Dai, and D. T. Haynie, *Nanotechnology* 17, R14 (**2006**).
21. A. Satti, D. Aherne, and D. Fitzmaurice, *Chem. Mater.* 19, 1543 (**2007**).
22. E. Nogales, M. Whittaker, R. A. Milligan, and K. H. Downing, *Cell* 96, 79 (**1999**).
23. A. Desai and T. J. Mitchison, *Annu. Rev. Cell Dev. Biol.* 13, 83 (**1997**).
24. O. Rath and F. Kozielski, *Nat. Rev. Cancer* 12, 527 (**2012**).
25. S. Kumar and A. Mansson, *Biotechnol. Adv.* 35, 867 (**2017**).
26. S. Behrens, K. Rahn, W. Habicht, K. J. Bohm, H. Rosner, E. Dinjus, and E. Unger, *Adv. Mater.* 14, 1621 (**2002**).
27. M. Mertig, R. Kirsch, and W. Pompe, *Appl. Phys. A-Mater. Sci. Process.* 66, S723 (**1998**).
28. R. Kirsch, M. Mertig, W. Pompe, R. Wahl, G. Sadowski, K. J. Bohm, and E. Unger, *Thin Solid Films* 305, 248 (**1997**).
29. J. C. Zhou, Y. Gao, A. A. Martinez-Molares, X. Jing, D. Yan, J. Lau, T. Hamasaki, C. S. Ozkan, M. Ozkan, E. Hu, and B. Dunn, *Small* 4, 1507 (**2008**).
30. I. Staxen, C. Bergounioux, and J. F. Bornman, *Protoplasma* 173, 70 (**1993**).
31. L. Bjorn, J. Moan, W. Nultsch, and A. Young, Environmental UV Photobiology, Springer, New York (**1993**).
32. J. C. Zhou, X. Wang, M. Xue, Z. Xu, T. Hamasaki, Y. Yang, K. Wang, and B. Dunn, *Mater. Sci. Eng. C-Mater. Biol. Appl.* 30, 20 (**2010**).
33. L. C. Ciacchi, M. Mertig, R. Seidel, W. Pompe, and A. De Vita, *Nanotechnology* 14, 840 (**2003**).
34. T. G. Appleton, F. J. Pesch, M. Wienken, S. Menzer, and B. Lilppert, *Inorg. Chem.* 31, 4410 (**1992**).
35. D. Grasseschi and H. E. Toma, *Coord. Chem. Rev.* 333 (**2017**).
36. V. Amendola, R. Pilot, M. Frasconi, O. M. Marago, and M. A. Iati, *J. Physics-Condensed Matter* 29 (**2017**).
37. J. A. Fan, K. Bao, J. B. Lassiter, J. Bao, N. J. Halas, P. Nordlander, and F. Capasso, *Nano Lett.* 12, 2817 (**2012**).
38. D. Oliveira, D.-M. Kim, M. Umetsu, I. Kumagai, T. Adschiri, and W. Teizer, *J. Appl. Phys.* 112 (**2012**).
39. T. Ibii, M. Kaieda, S. Hatakeyama, H. Shiotsuka, H. Watanabe, M. Umetsu, I. Kumagai, and T. Imamura, *Anal. Chem.* 82, 4229 (**2010**).
40. M. Umetsu, T. Hattori, S. Kikuchi, I. Muto, T. Nakanishi, H. Watanabe, and I. Kumagai, *J. Mater. Res.* 23, 3241 (**2008**).
41. L. Nieba, A. Krebber, and A. Pluckthun, *Anal. Biochem.* 234, 155 (**1996**).
42. E. Nogales, S. G. Wolf, and K. H. Downing, *Nature* 391, 199 (**1998**).
43. H. Hakkinen, *Nat. Chem.* 4, 443 (**2012**).
44. A. H. Pakiari and Z. Jamshidi, *Journal Phys. Chem. A* 114, 9212 (**2010**).
45. T. N. Parac and N. M. Kostic, *J. Am. Chem. Soc.* 118, 5946 (**1996**).
46. P. Joshi, V. Shewale, R. Pandey, V. Shanker, S. Hussain, and S. P. Karna, *J. Phys. Chem. C* 115, 22818 (**2011**).
47. T. Kitagawa and S. Hirota, Handbook of Vibrational Spectroscopy, John Wiley & Sons, New York, USA (**2002**).
48. E. Smith and G. Dent, Modern Raman Spectroscopy, John Wiley & Sons, New York, USA (**2005**).
49. S. Hashimoto and H. Takeuchi, *J. Am. Chem. Soc.* 120, 11012 (**1998**).
50. A. Tlahuice-Flores, R. L. Whetten, and M. Jose-Yacaman, *J. Phys. Chem.-C* 117, 12191 (**2013**).
51. T. Buergi, *Nanoscale* 7, 15553 (**2015**).
52. T. Mahaddalkar, S. Mehta, S. Cheriyamundath, H. Muthurajan, and M. Lopus, *Exp. Cell Res.* 360, 163 (**2017**).

RESEARCH ARTICLE

RESEARCH ARTICLE

Room temperature synthesis and Raman spectral evidence of carbon bond ranelate–gold nanoparticles

Júlio C. da Rocha | João V. Mattioni | Luca M. Sihn | Jorge S. Shinohara [ORCID] |
Fernando M. Melo | Mauricio P. Franco [ORCID] | Ataualpa A.C. Braga [ORCID] |
Henrique E. Toma [ORCID]

Instituto de Química, Universidade de São
Paulo, São Paulo, Brazil

Correspondence
Henrique E. Toma, Instituto de Química,
Universidade de São Paulo, 05508-000 São
Paulo, SP, Brazil.
Email: henetoma@iq.usp.br

Funding information
Fundação de Amparo à Pesquisa do
Estado de São Paulo, Grant/Award
Number: FAPESP 2018/21489-1

Abstract
Ranelate ions, employed in the past as strontium salt for the treatment of osteoporosis, exhibit a rather interesting chemistry associated with a central thiophene ring encompassing two carboxylic groups, a cyanonitrile substituent, and a nitrile diacetate group. In spite of their unfavorable reduction potentials, around 1.26 V, they react very rapidly with $HAuCl_4$ at room temperature, leading to decarboxylation at the C5 position in order to generate gold nanoparticles strongly stabilized by Au–C bonds. The reactions were elucidated by electrospray ionization mass spectrometry, ligand exchange kinetics, and by means of the surface-enhanced Raman scattering effect. The gold nanoparticles were further characterized based on transmission electron microscopy and CytoViva hyperspectral microscopy.

KEYWORDS
gold nanoparticles, gold ranelates, gold–carbon bond, plasmonics, SERS

1 | INTRODUCTION

Plasmonic nanoparticles have received special attention in the last years because of their wide range applications in medicine and nanotechnology.[1–4] Among the several types, a special class is formed by the gold nanoparticles (AuNPs). They have been obtained in many ways, exhibiting strong plasmon resonance bands responsible for their red–violet colors. In addition, the presence of plasmonic waves generates enhanced electric fields or "hot spots," particularly at the conjunction of two or more nanoparticles, or at the edge of anisotropic nanocrystals.[5] Such electric fields are responsible for the enhancement of the Raman scattering spectra of the molecules at the nanoparticles surface located at such hot spots. This effect is known as surface-enhanced Raman scattering (SERS)[4, 6, 7] and can promote a huge enhancement of the Raman signals up to 14 orders of magnitude, eventually approaching the conditions for a single molecule detection.

The properties of such plasmonic nanoparticles are deeply associated with the physical and chemical interactions of the molecules with the surface plasmonic waves and are manifested by means of the electromagnetic effect and/or by means of chemical effects involving charge-transfer and resonant excitation of the molecules close to the surface Fermi levels.[8, 9] In this way, the surface molecules are extraordinarily relevant in dictating the behavior of the plasmonic nanoparticles.[4]

One of the most important examples are the so-called Turkevich gold nanoparticles.[10, 11] They are obtained by the reduction of $[AuCl_4]^-$ with citrate ions in aqueous solution, and the process is strongly dependent upon the experimental conditions, proceeding mainly at the boiling point temperatures. The mechanism seems to involve a gold–carbon bound ketone form of the decarboxylated

citrate ion.[12] Such species is surprisingly stable and has been recognized by means of their strong SERS signals, contrasting with the conventional Turkevich O-bond citrate–gold nanoparticles.[12] Although a large number of reducing species, such as ascorbate and natural products,[13] have already been employed for generating gold nanoparticles, the reactions usually take place very slowly, requiring high temperatures and generating agglomerated products.

In this work, we have observed that the ranelate ion reacts rapidly with Au(III) ions, at room temperature, yielding stabilized gold nanoparticles in solution. Such ranelate species have been largely consumed in the past as a antiosteoporotic drug[14–17] in the form of a strontium complex. Its molecular structure[18] is rather curious (Scheme 1), encompassing a thiophene ring with two carboxylic groups, a cyanonitrile substituent, and a nitrile diacetate group. The molecule is a good chelating agent for metal ions because of the presence of four carboxylate groups. It has never been used as reducing agent for generating metal nanoparticles because of its very small reduction power in aqueous solution ($E° = 1.2$ V vs. SHE). Therefore, the surprising reactivity of the ranelate ion towards Au(III) ions instigated our curiosity, leading to the discovery of unusual carbon bond stabilized nanoparticles. Their characterization has been carried out based on transmission electron microscopy, SERS, electronic spectroscopy, and kinetic studies in aqueous solution.

2 | EXPERIMENTAL

2.1 | Materials

Tetrachloroauric acid ($HAuCl_4$) and 4-mercaptopyridine were obtained from Sigma-Aldrich, and all other reagents were of analytical grade and used without further purification.
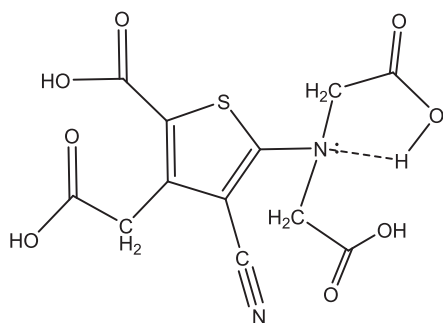
SCHEME 1 Structural representation of the ranelate ion

2.1.1 | Strontium ranelate (SrRan)

The reagent was prepared from strontium ranelate (SrRan) available as Protos® sachets containing nearly 2 g of the drug and other excipients such as aspartame, maltodextrin, and manitol. Purification of the barely soluble SrRan (800 mg L^{-1}, 25°C) was carried out by suspending 10 g of Protos® in 100 ml of water and stirring for 2 hr, at 50°C. SrRan was separated after centrifugation at 5,000 rpm, and the washing/extraction process was repeated twice. Finally, the solid was treated with 50 ml of ethanol, centrifuged, and dried at 100°C. Anal. Calcd (found) for $Sr_2(ran)·9(H_2O)$, $C_{12}H_{24}N_2O_{17}SSr_2$, MM 875.6; C, 21.46 (21.33); H, 3.38 (3.58); N, 4.09 (4.15).

2.1.2 | Lithium ranelate (LiRan) and sodium ranelate (NaRan)

SrRan (4.0 g, 4.5 mmol) suspended in 30 ml of water was treated with 0.67-g Li_2CO_3 (9.1 mmol) or 0.97-g Na_2CO_3 (9.1 mmol) and kept under stirring at 70°C for 3 hr. After separating the $SrCO_3$ precipitate by centrifugation at 4,500 rpm, the solution was evaporated to complete dryness. The solid was collected on a filter and washed with dry ethanol. Anal. Calcd (found) for LiRan·4H$_2$O, $C_{12}H_{14}Li_4N_2O_{12}S$, MM 438.07; C, 33.32 (32.90); H, 3.04 (3.22); N, 6.44 (6.39). Calcd (found) for NaRan·8H$_2$O, $C_{12}H_{22}Na_4N_2O_{16}S$, MM 574.33, C, 25.98 (25.10); H, 3.30 (3.86), N, 4.69 (4.88).

2.1.3 | HRanelate (H5Ran)

LiRan (1 g) was suspended into 5 ml of water and transferred to an open Petri dish, in the fume hood. Then 5 ml of 12-M HCl was added, and the solution was kept overnight under complete darkness. In the next day, well-formed transparent crystals were observed. Slow evaporation for 2 days in the dark yielded a large crop of crystals, which were collected on a glass sintered filter and washed with diethyl ether. Analytical calculation (found) for $C_{11}H_{10}N_2O_6S$, MM 299.03; C, 44.30 (43,95); H, 3.38 (3.48); N, 9.39 (9.22).

2.1.4 | Gold nanoparticles synthesis

They were directly obtained by pouring $HAuCl_4$ (concentrations ranging from 0.8 to 0.0125 mmol L^{-1}) onto the 0.1 mmol L^{-1} ranelate solutions and kept under magnetic stirring and room temperature (23 ± 2°C) for 1 hr.

2.2 | Instrumentation

The electronic spectra were recorded on a Hewllet Packard 8453A diode-array spectrophotometer. For the kinetics study, the spectra were recorded every 0.5 s for the first 200 s of reaction. Raman and SERS spectra were recorded on an InPhotonics portable instrument, equipped with a diode laser emitting at 785 nm, covering the range of 350–2,060 cm^{-1}. With this excitation laser, the spectrum was acquired using 100 mW of power and 120 s of integration time, applying 60 s of delay time between each measurement. Confocal Raman microscopy measurements were performed with a WITEC alpha 300R equipment using a 633-nm laser. Scanning electron microscopy images were obtained using a JEOL model 7200 field emission electron microscope. Dynamic light scattering and zeta potential measurements were carried out using a Zetasizer Nano S equipment (Malvern, UK) at 25°C. Electrospray ionization (ESI) mass spectrometry was obtained using an Esquire 3000 Plus Bruker Daltonics instrument.

2.3 | Theoretical calculations

DFT theoretical calculations (Figure S1) were carried out using Gaussian 09D, at M06-2X functional level, and cc-PVTZ base, incorporating the solvation model (SMD) encompassing water molecules. The corresponding HOMO and LUMO levels can be seen in Figure S2. Semi-empirical ZINDO/S calculations[19] were carried out using the Hyperchem 8.05 computational package, combining interactive MM$^+$ geometry and CI calculations, by performing optimization cycles up to convergence limit of about 10^{-5} kcal Å^{-1} mol^{-1}. The electronic distribution was generated from single CI excitations in an active space involving 20 frontier molecular orbitals (10 highest occupied and 10 lowest unoccupied MOs),[19] and the calculated HOMO and LUMO levels are shown in Figure S3.

3 | RESULTS AND DISCUSSION

Contrasting with the majority of species, such as ascorbate and citrate ions, usually employed in gold nanoparticle synthesis at high temperatures, the ranelate ions react rapidly with HAuCl$_4$ in aqueous solution at room temperature, yielding deep red colloidal solutions. The solutions are rather stable, and their zeta potentials (Figure 1) correspond to -31 ± 2 mV above pH 7, indicating the presence of a negatively charged coating presumably derived from the ranelate ions. The inflection point
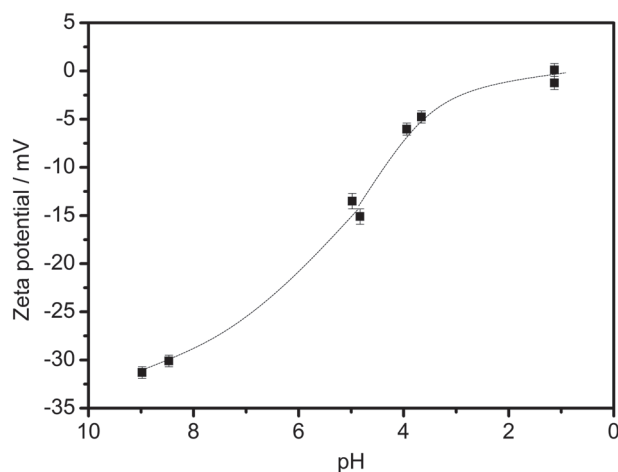

FIGURE 1 Zeta potentials of Au–ranelate nanoparticles in aqueous solution, at several pHs

at pH 5 reflects the apparent pKa of the adsorbed species, reaching the isoelectric point at pH 1. Such acid–base behavior is compatible with the presence of the carboxylic groups of the ranelate species, at the gold nanoparticles surface.

The nanoparticles formation proceeds very fast, particularly at HAuCl$_4$ concentrations above 1 mM. For monitoring the process spectrophotometrically, the reactant concentrations were kept as lowest as possible, for example, 0.10 mM, in order to slow down the reaction rates. For a fixed ranelate ion concentration, for example, 0.10 mM, the Au(III) concentrations were varied from 0.80 to 0.05 mM, leading to [Au(III)]/[Ran] ratios in the 8:1 to 1:2 range.

For [Au(III)] in 0.80 to 0.40 mM range, two peaks have been observed at 537 nm and around 820–990 nm for the ranelate salts of Li$^+$, Na$^+$, and Sr^{2+}, as illustrated in Figures 2 and S4.

The initial decay (indicated by I in Figure 2) of the ranelate band at 311 nm proceeds within 10 s, reflecting the ranelate reaction with the Au(III) ions generating the precursor or intermediate species that will promote nucleation of the gold nanoparticles in the next step (II), as observed by the sharp increase of extinction at 535 and 820–990 nm. In agreement with LaMer's theory,[20] the rapid nucleation of seeds is followed by their slow conversion into smaller nanoparticles (III) and their maturation to the final sizes (IV). The two peak extinction profiles impart characteristic colors of anisotropic nanoparticles in solution, as confirmed by the scanning electron microscopy images in Figure 2b,e,h. The final nanoparticles size distribution was centered around 25 nm for all the samples, with a similar, narrower profile for Li$^+$ and Na$^+$ ions, and a broader profile for Sr^{2+} ions, spanning the 5–65 nm range.
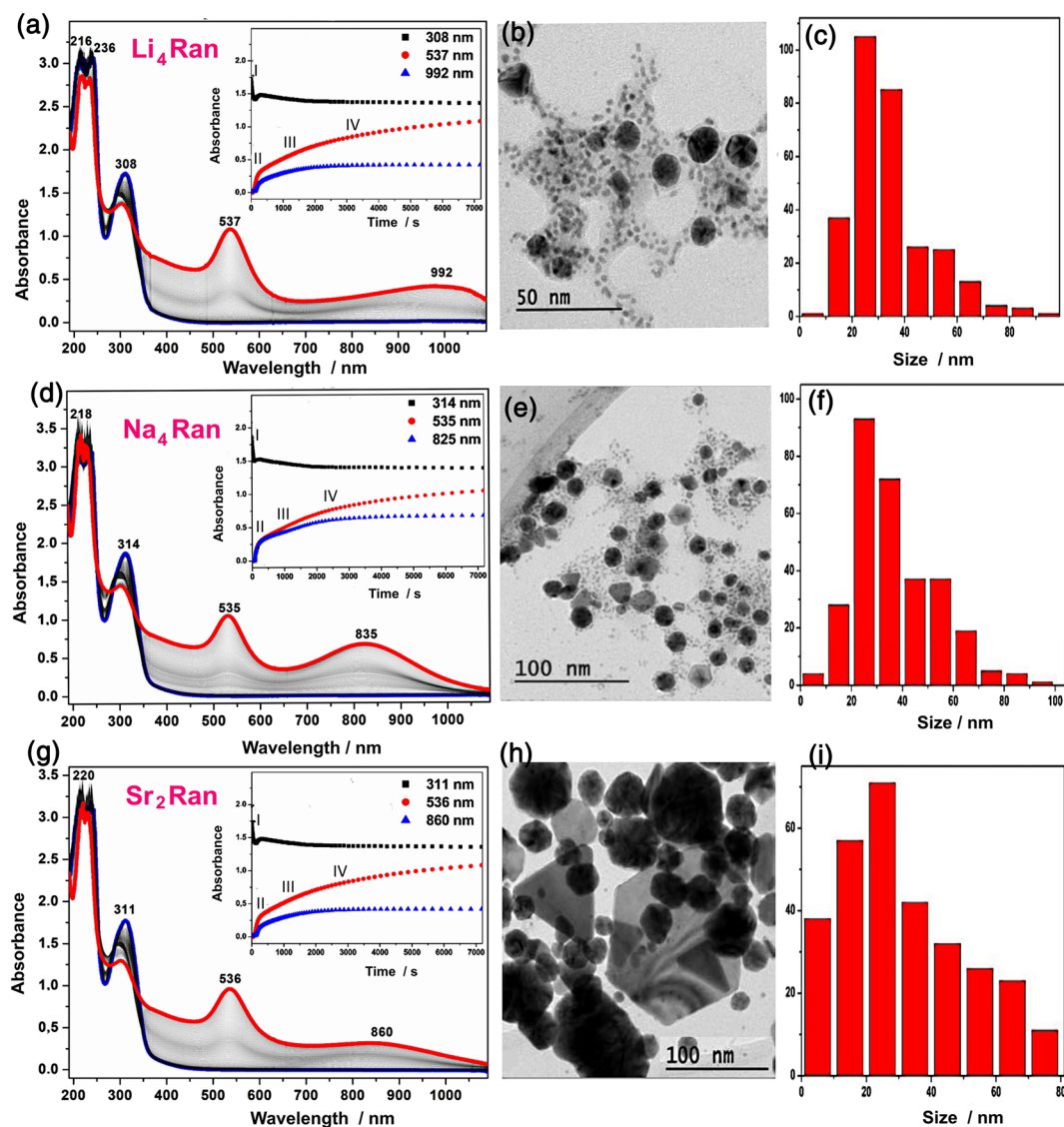
FIGURE 2 Spectrophotometric monitoring of the reactions of 0.10-mM lithium (a–c), sodium (d–f), and strontium (g–i) ranelate with HAuCl$_4$ (0.80 mM) at room temperature, including their respective scanning electron microscopy images and size distribution profiles

The great diversity of geometries in the case of strontium ranelate reactions (Figure 2h) is really intriguing and was probed by hyperspectral dark field CytoViva microscopy, as illustrated in Figure S5. The hyperspectral images in this figure correspond to the distinct shapes previously shown in Figure 2h, encompassing discs, cubes, triangles, spheres, and rods, as identified by their characteristic extinction spectra.[21]

As illustrated in Figure 3, at [Au(III)]/[Ran] ratios of 2:1 (and below, see Figure S6), only a single plasmonic peak has been observed around 535 nm, increasing with the decay of the [AuCl$_4$]$^-$, in addition to the ranelate bands at 218 and 322 nm, respectively. The red solutions are similar to those containing spherical nanoparticles, but the microscopy images reveal a bimodal distribution of nanoparticles, with sizes around 3 and 13 nm, for the

Li$^+$ and Na$^+$ ranelate species, and 3 and 17 nm, for the Sr^{2+} ranelate species.

Accordingly, the formation of the precursor species and nucleation seem to occur in parallel (Step I) generating the smaller nanoparticles contributing to the extinction profiles at 400 nm. This fact is apparent in the microscopy images and size distribution profiles in Figure 4b,e,g showing the predominance of nanoparticles around 3–7 nm. The growing step proceeds more slowly (Step II) leading to particles of about 17 nm in Figure 3.

A more detailed observation of the nucleation process was carried out by using a 1:1 [Au(III)]/[Ran] proportion, as illustrated in Figure 4. In this case, it was possible to follow the formation of the precursor species or clusters absorbing at 420 nm (Step I, 0–6 s) generating the nanoparticles seeds (Step II, 6–12 s) absorbing around
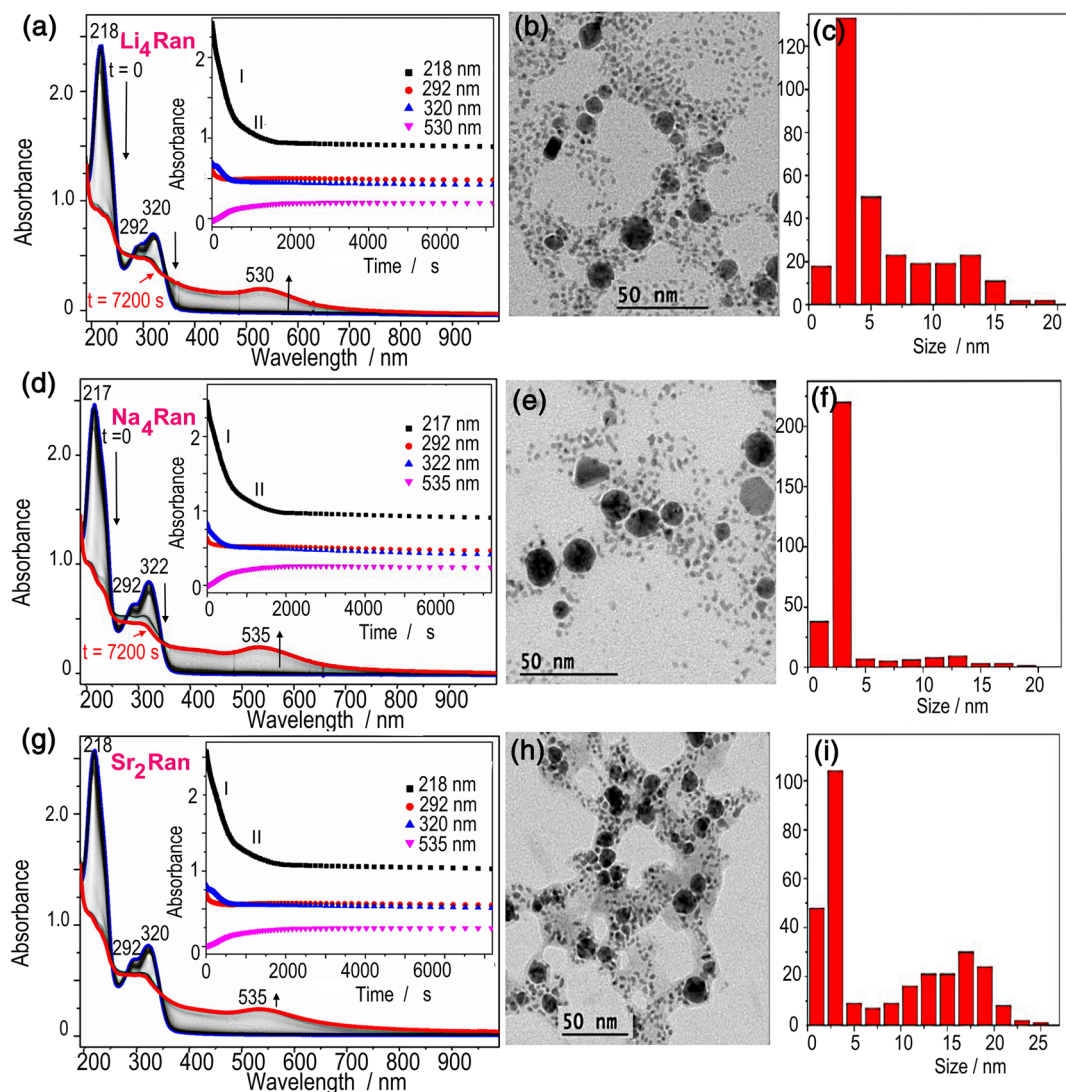
FIGURE 3 Spectrophotometric monitoring of the reactions of 0.1-mM lithium (a–c), sodium (d–f), and strontium (g–i) ranelate with HAuCl₄ (0.20 mM) at room temperature, including their respective scanning electron microscopy images and size distribution profiles

520 nm (Step III, 12–60 s). The remaining clusters absorbing at 420 nm are responsible for the bimodal distribution shown in previous Figure 4. Their slow decay seems to be accompanied by formation of large nanoparticles, similar to the Ostwald ripening process[22] (Step IV, 60–700 s). This process is not apparent in the kinetic plots at 520 nm in Figure 5 because of the spectral overlap between the growing plasmonic band and the decaying band at 420 nm.

In the high-resolution transmission electron microscopy image shown in Figure S7, it is possible to discriminate the crystallographic plane 111 ($d = 2.348$ Å) of the gold nanoparticles, confirming their crystalline structure. A close inspection also revealed the existence of a thin protecting coating encompassing the bound ranelate species.

3.1 | Mechanism of formation

The intriguing point not yet answered up to this stage concerns the role of the ranelate species in the formation of the gold nanoparticles. As a matter of fact, the stability of the gold–ranelate nanoparticles is consistent with the presence of a protecting coating, as observed in the Turkevich citrate stabilized nanoparticles, where the adsorbed anionic species prevent agglomeration by means of repulsive electrostatic forces.

In order to obtain some clues about the reaction involved, the 8:1 [Au(III)]/[ranelate] suspension was centrifuged at 5,000 rpm for 30 min in order to separate the gold nanoparticles from the solution. After this process, the deposited nanoparticles are no longer stable and cannot be resuspended, indicating that some of the
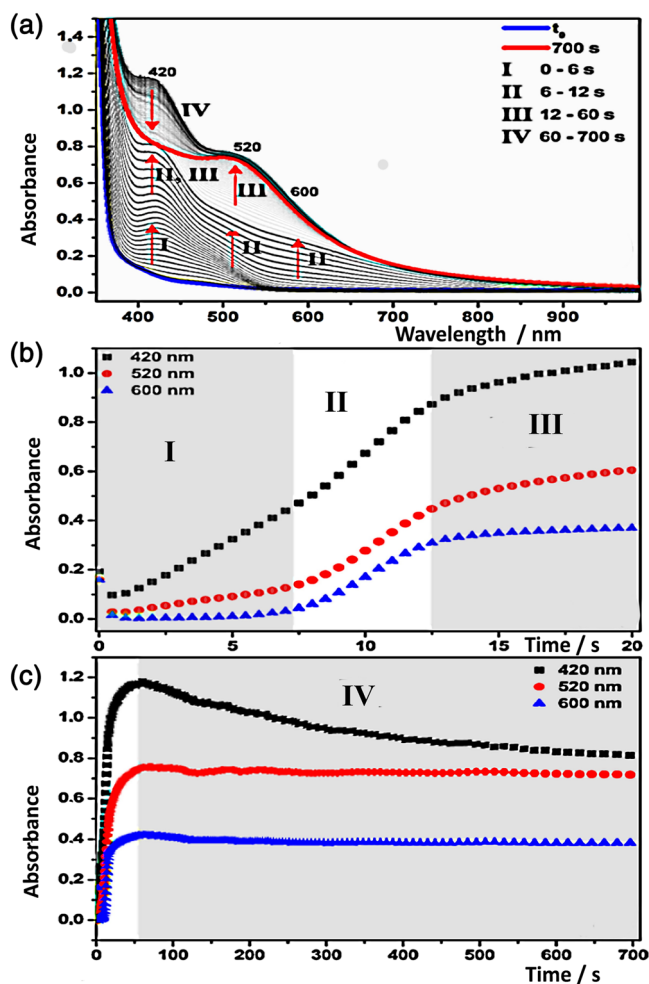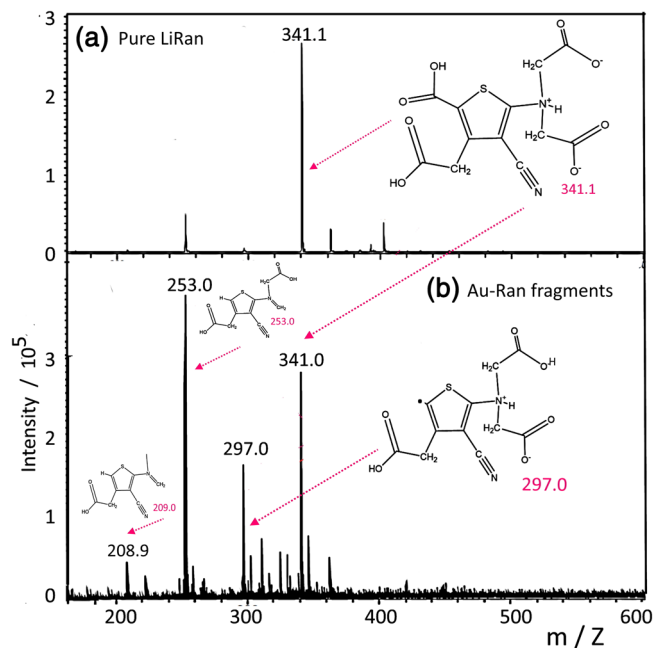
FIGURE 4 Spectrophotometric monitoring of the reactions of 0.1-mM lithium ranelate with $HAuCl_4$ (0.10 mM) at room temperature, showing the nucleation Steps I, II, and the grow of the nanoparticles, in the processes III and IV

FIGURE 5 Electrospray ionization mass spectrometry data, in the negative mode, for the pure ranelate ions (a) and for the species generated from the treatment with $HAuCl_4$ (8:1) after centrifugation at 5,000 rpm for 30 min, with their proposed structures

protecting coating has been removed by the strong rotational forces applied. The ESI spectrum of the corresponding solution exhibited peaks only in the negative mode, corresponding to the ranelate anions and their related products as illustrated in Figure 5. The ESI results indicated that the initial ranelate ion undergoes a decarboxylation reaction yielding a species of m/Z = 297 Daltons. Further decarboxylation reactions yield successive fragments exhibiting m/Z = 253 and 209 Daltons.
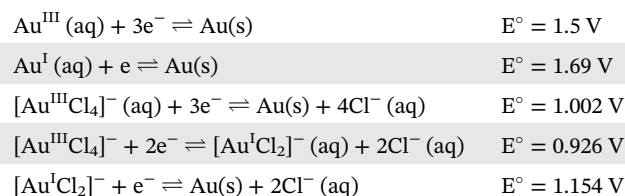
In agreement with this observation, we have recently discovered that in strongly acid solutions, for example, HCl 6 M, ranelic acid undergoes a slow decarboxylation reaction at the C5 position, leading to the so-called H5Ran species. This species has been isolated in crystalline form and its molecular structure determined by X-ray diffraction.[23] According to the theoretical calculations for the ranelate ion, there is a large electronic

concentration on the C5 position (Figures S2 and S3) attached to the carboxylate group, contributing to the HOMO (4%) and LUMO levels (12%). The high electron density distribution on the C5 atom turns it susceptible to the attack of protons explaining the previously observed decarboxylation reaction in the presence of acids. This observation is also in agreement with the pattern observed for aminothiophenes and their derivatives in the literature.[24]

It should be noted that the Au(III) complexes are strong oxidizing agents, displaying typical reduction potentials in the range of 0.9 to 1.7 V:

Au^{III} (aq) $+ 3e^- \rightleftharpoons Au(s)$	$E° = 1.5$ V
Au^{I} (aq) $+ e \rightleftharpoons Au(s)$	$E° = 1.69$ V
$[Au^{III}Cl_4]^-$ (aq) $+ 3e^- \rightleftharpoons Au(s) + 4Cl^-$ (aq)	$E° = 1.002$ V
$[Au^{III}Cl_4]^- + 2e^- \rightleftharpoons [Au^{I}Cl_2]^-$ (aq) $+ 2Cl^-$ (aq)	$E° = 0.926$ V
$[Au^{I}Cl_2]^- + e^- \rightleftharpoons Au(s) + 2Cl^-$ (aq)	$E° = 1.154$ V

But surprisingly, as shown in Figure 6, the ranelate ion undergoes oxidation above 1.039 V versus Ag/AgCl (1.26 V vs. SHE). Although it matches the redox potentials of the Au(III) ions, the driving force is not particularly large in comparison with typical reducing species, such as ascorbate ions ($E° = 0.35$ V). Therefore, one
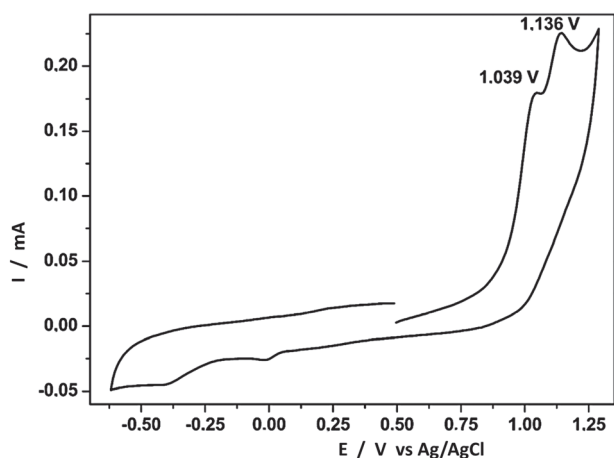
FIGURE 6 Cyclic voltammogram of LiRan (1 mM), in aqueous solution, onto glassy carbon electrodes, 75 mV s^{-1}, 0.5 mol L^{-1} KCl, 25°C

cannot explain the enhanced reactivity of the ranelate species solely based on their redox potentials.

This argument also applies to the synthesis of the Turkevich nanoparticles, because the oxidation potentials of the citrate ions are also located above 1.0 V.[25] In this case, a high temperature is required to accelerate the reaction, but the formation of a gold–carbon bond has been demonstrated in the process, stabilizing the Au(I)–C and Au(0)–C species derived from the keto intermediate produced in the synthesis. We presume that the formation of such strong gold–carbon bonds can be the driving force required for the formation of the gold nanoparticles. It should be noticed that whereas the Turkevich citrate–AuNPs, involving gold–carboxylate (Au–O) bonds, are labile, the corresponding gold–carbon bound keto forms

are relatively more inert. Such differences in the kinetics reflect the presence of stronger Au–C bonds in the Au-keto form, in agreement with simple hard–soft base principles.

In this way, it is plausible that the electron-transfer reaction between Au(III) and ranelate ions leads to the decarboxylation at the C5 position in the thiophene ring, generating the radical species (m/Z = 297) detected in the ESI spectra. Such species can form strong bonds with Au(I) and Au(0) entities, as illustrated in Figure 7. The formation of stable Au–C bonds has precedence in the Turkevich system[12] and can explain the great stability observed for the gold–ranelate system.

In order to test such hypothesis, we investigated the kinetics of ligand exchange in the gold–ranelate nanoparticles generated according to the scheme shown in Figure 7 and compared with the ligand exchange behavior of previously formed Turkevich nanoparticles in the presence of LiRan or H5Ran species, using the strongly binding mercaptopyridine ligand, MPy. This ligand has a great affinity for gold nanoparticles[26] and has been used to displace most conventional ligands from their coordination sphere. From the chemical point of view, the exchanging rates express the binding properties of the molecules at the gold nanoparticle surface. For instance, whereas the ligand exchange kinetics with MPy in O-bond Turkevich gold nanoparticles is accomplished in less than 5 s, the reaction of the carbon bond keto-gold nanoparticles proceeds at least three times slower.

In this work, we have observed that the presence of LiRan or H5Ran species has no influence on the kinetics of the O-bond Turkevich gold nanoparticles with MPy. This means that the chemical affinity of the gold nanoparticles to the aromatic thiophene group should be
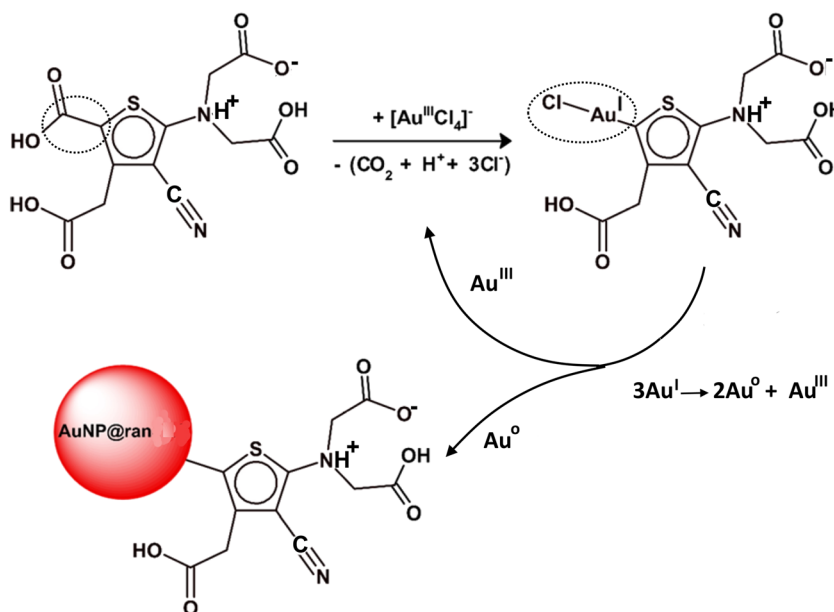
FIGURE 7 Reaction mechanism of ranelate ions with HAuCl$_4$ in aqueous solution, showing the decarboxylation process at C5, and formation of an Au(I)–C5(Ran) intermediate that undergoes disproportionation into Au(0) and Au(III) species, during the gold nanoparticles nucleation step
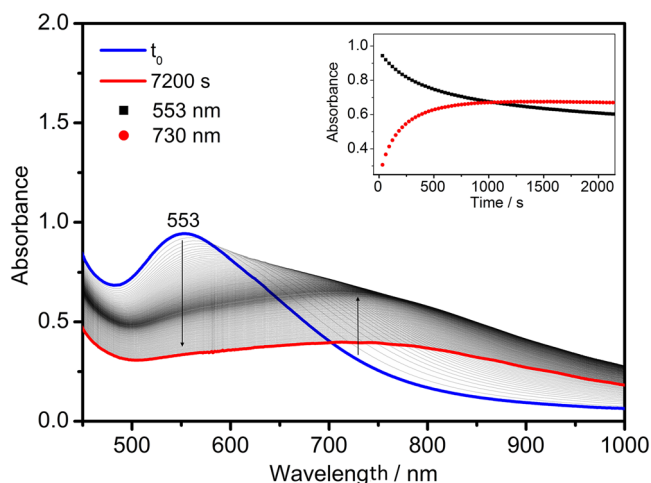
rather small, not excluding a possible steric hindrance influence from the neighboring carboxylic groups.

On the other hand, the ligand exchange kinetics of the previously generated Au–Ran nanoparticles with MPy (Figure 8) is surprisingly slow, requiring more than 500 s to accomplish even in the presence of a large excess of MPy. Such kinetics behavior indicates the existence of strong bonds between the gold atoms and the ranelate species, corroborating the hypothesis of formation of Au–C bonds.
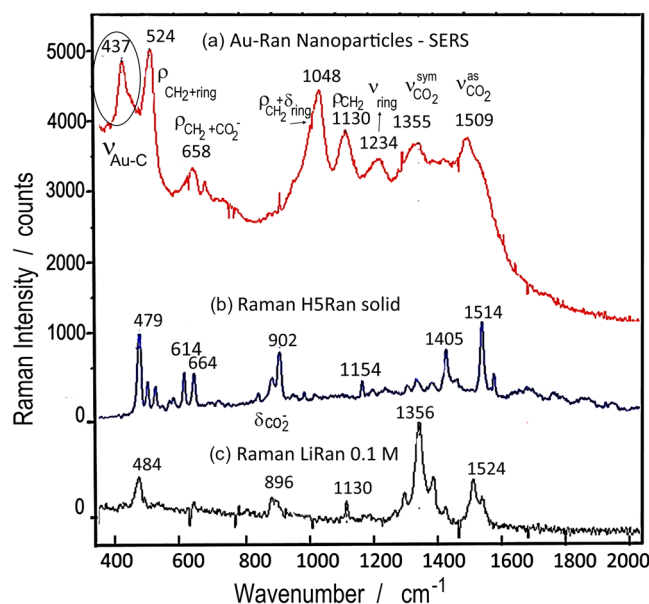
A similar case has been reported by Crudden et al.[27] in the formation of ultrastable self-assembly monolayers of N-heterocyclic carbenes onto gold and ascribed to the presence of strong Au–C bonds.

The first spectroscopic evidence for the formation of Au–C bonds has been reported by Laurentius et al.[28] in the reaction of gold nanoparticles and diazobenzene molecules. In this case, a weak signal at 412 cm^{-1} has been ascribed to the Au–C vibration in the Raman spectra, but such tenuous evidence has been consolidated by exhaustive spectral comparisons involving all the reactants in the system. Recently, Berisha et al.[29] ascribed the Raman wavenumber at 387 cm^{-1} to the Au–C (alkyl) bond in Au–CH$_2$(CH$_2$)$_3$COOH nanoparticles, in excellent agreement with theoretical calculations. It should be noticed that such vibrational peak is also apparent in the SERS spectra of the Au–C keto form of the Turkevich nanoparticles at 380 cm^{-1}, although it has been tentatively assigned to a composite ρCH$_2$ vibration,[12] by the lack of suitable examples from the literature at that time.

In order to investigate this possibility, we recorded the Raman spectra of the Au–ranelate nanoparticles generated according to the scheme in Figure 7, by focusing

FIGURE 9 Surface-enhanced Raman scattering (SERS) profile for the AuNP@ran species, at λ_{exc} 785 nm, in comparison with the normal Raman spectra of H5Ran and LiRan, 0.1 M, showing a differential peak at 437 cm^{-1} tentatively ascribed to ν(Au–C) by comparison with the literature[28, 29]

at λ_{exc} = 785 nm, far from the fluorescence excitation of the ranelate species.

The observed results indicated the occurrence of the SERS effect, by the large intensification of the Raman peaks in relation to the normal Raman spectra of the H5Ran and LiRan species. For comparison purposes, the ranelate ion vibrations (FTIR and Raman) for the lithium, sodium, and strontium salts can be seen in Figure S8. Their assignment was based on the theoretical DFT calculations shown in Table S1.

It should be noticed that the addition of LiRan or H5Ran to the O-bond Turkevich gold nanoparticles does not lead to detectable SERS signals, corroborating the weak interaction observed kinetically. In contrast, the Au–Ran nanoparticles exhibit characteristic SERS signals (Figure 9). The peak at 437 cm^{-1} seems differential and is compatible with the Au–C vibration reported in the literature.[28, 29] As previously observed for the carbon bond Turkevich nanoparticles,[12] the presence of strong covalent bonds should also enhance the SERS effect, corroborating our mechanistic proposal in Figure 7.

4 | CONCLUSION

Ranelate ions react with HAuCl$_4$ yielding spherical or anisotropic nanoparticles, at room temperature, depending upon the experimental conditions. The

FIGURE 8 Ligand exchange kinetics of the ranelate–Au nanoparticles in the presence of 4-mercaptopyridine (0.10 mol L^{-1})

reaction involves decarboxylation reactions at the C5 position in the thiophene ring, facilitating the binding of the Au(I) and Au(0) species along the nucleation process. The detailed kinetics provided a consistent view of the steps involved in the generation of the gold nanoparticles, based on LaMer's theory. The several nanoparticle shapes observed by electron microscopy were consistent with the CytoViva hyperspectral analysis focusing on the plasmonic bands involved. The gold nanoparticles seem to be stabilized by the ranelate products by means of strong Au–C bonds, as deduced from ESI mass spectra and ligand exchange kinetics, consistently with the presence of a peak at 437 cm^{-1} in the SERS spectrum.

ACKNOWLEDGEMENT

ORCID
Jorge S. Shinohara https://orcid.org/0000-0003-2192-4854

Mauricio P. Franco https://orcid.org/0000-0002-0193-8397

Ataualpa A.C. Braga https://orcid.org/0000-0001-7392-3701

Henrique E. Toma https://orcid.org/0000-0002-4044-391X

REFERENCES
[1] K. M. Mayer, J. H. Hafner, *Chem. Rev.* **2011**, *111*, 3828.

[2] N. J. Halas, S. Lal, W.-S. Chang, S. Link, P. Nordlander, *Chem. Rev.* **2011**, *111*, 3913.

[3] M. E. Stewart, C. R. Anderton, L. B. Thompson, J. Maria, S. K. Gray, J. A. Rogers, R. G. Nuzzo, *Chem. Rev.* **2008**, *108*, 494.

[4] D. Grasseschi, H. E. Toma, *Coord. Chem. Rev.* **2017**, *333*, 108.

[5] D. Grasseschi, M. L. d. O. Pereira, J. S. Shinohara, H. E. Toma, *J. Nanopart. Res.* **2018**, *20*, 35.

[6] R. F. Aroca, *Surface-enhanced vibrational spectroscopy*, John Wiley & Sons, Ltd., Chichester **2006**.

[7] R. F. Aroca, *Phys. Chem. Chem. Phys. PCCP* **2013**, *15*, 5355.

[8] J. R. Lombardi, R. L. Birke, *J. Chem. Phys.* **2012**, *136*, 144704.

[9] J. R. Lombardi, R. L. Birke, *Acc. Chem. Res.* **2009**, *42*, 734.

[10] J. Turkevich, P. Stevenson, J. Hillier, *J. Phys. Chem.* **1953**, *57*, 670.

[11] G. Frens, *Nat. Phys. Sci.* **1973**, *241*, 20.

[12] D. Grasseschi, R. A. Ando, H. E. Toma, V. M. Zamarion, *RSC Adv.* **2015**, *5*, 5716.

[13] S. S. Shankar, A. Rai, B. Ankamwar, A. Singh, A. Ahmad, M. Sastry, *Nat. Mater.* **2004**, *3*, 482.

[14] G. J. Atkins, K. J. Welldon, P. Halbout, D. M. Findlay, *Osteoporos. Int.* **2009**, *20*, 653.

[15] M. Pilmane, K. Salma-Ancane, D. Loca, J. Locs, L. Berzina-Cimdina, *Mater. Sci. Eng. C* **2017**, *78*, 1222.

[16] M. R. M. Ibrahim, S. Singh, A. M. Merican, H. R. B. Raghavendran, M. R. Murali, S. V. Naveen, T. Kamarul, *BMC Vet. Res.* **2016**, *12*, 1.

[17] J.-Y. Reginster, M.-L. Brandi, J. Cannata-Andia, C. Cooper, B. Cortet, J.-M. Feron, H. Genant, S. Palacios, J. D. Ringe, R. Rizzoli, *Osteoporos. Int.* **2015**, *26*, 1667.

[18] K. Stahl, C. G. Frankaer, A. C. Raffalt, S. R. Sorensen, J. E. T. Andersen, *Acta Crystal. Section E - Struct. Rep. On Line.* **2011**, *67*, M471.

[19] S. I. Gorelsky, A. B. P. Lever, *Organometal. Chem.* **2001**, *635*, 187.

[20] V. K. LaMer, R. H. Dinegar, *J. Am. Chem. Soc.* **1950**, *72*, 4847.

[21] Y. Xia, Y. Xiong, B. Lim, S. E. Skrabalak, *Angew. Chem. Int. Ed.* **2009**, *48*, 60.

[22] W. Ostwald, *Zeits. Phys. Chem.* **1897**, *22*, 289.

[23] J. C. Rocha, L. M. Sihn, M. K. Uchiyama, M. A. Ribeiro, M. P. Franco, A. A. C. Braga, A. T. Silveira, H. E. Toma, *Chem. Select* **2019**, *4*, 13926.

[24] R. K. Norris, *Chem. Heteroc. Compd.* **1986**, *44*, 631.

[25] O. Israel Gonzalez-Pena, T. W. Chapman, Y. Meas Vong, R. Antano-Lopez, *Electrochim. Acta* **2008**, *53*, 5549.

[26] F. S. Nunes, L. D. S. Bonifácio, K. Araki, H. E. Toma, *Inorg. Chem.* **2006**, *45*, 94.

[27] C. M. Crudden, J. H. Horton, I. I. Ebralidze, O. V. Zenkina, A. B. McLean, B. Drevniok, Z. She, H.-B. Kraatz, N. J. Mosey, T. Seki, E. C. Keske, J. D. Leake, A. Rousina-Webb, G. Wu, *Nat. Chem.* **2014**, *6*, 409.

[28] L. Laurentius, S. R. Stoyanov, S. Gusarov, A. Kovalenko, R. Du, G. P. Lopinski, M. T. McDermott, *ACS Nano* **2011**, *5*, 4219.

[29] A. Berisha, C. Combellas, F. Kanoufi, J. Medard, P. Decorse, C. Mangeney, I. Kherbouche, M. Seydou, F. Maurel, J. Pinson, *Langmuir* **2018**, *34*, 11264.

SUPPORTING INFORMATION
Additional supporting information may be found online in the Supporting Information section at the end of this article.

How to cite this article: da Rocha JC, Mattioni JV, Sihn LM, et al. Room temperature synthesis and Raman spectral evidence of carbon bond ranelate–gold nanoparticles. *J Raman Spectrosc.* 2020;1–9. https://doi.org/10.1002/jrs.5872

PÁGINA EM BRANCO

SUPPLEMENTARY MATERIAL

Hyperspectral Dark Field and Confocal Raman Microscopy Studies in Chemistry and Nanotechnology

This appendix serves as a guide to sample preparation and procedures for operating the CytoViva (Dark Field) and Witec Alpha300R (Raman Confocal) microscopes.

SUMMARY

CytoViva

Fundamentals

Sample preparation

Blade functionality (APTS/MPTS)

Operational script for image acquisition

Equipment

Software

Operational script for image acquisition

Data analysis and processing

Witec Alpha 300R

Operational roadmap for calibration and spectrum acquisition

Basic script for image treatment

CYTOVIVA MICROSCOPE

It creates darkfield images, with the light source having an annular (ring-shaped) condenser lens that forms a hollow cone of light so that the beam is not captured by the objective (Figure 1A)

It provides optical and spectral scattering imaging of the sample, with a resolution of $\lambda/5$, or approximately 80nm.

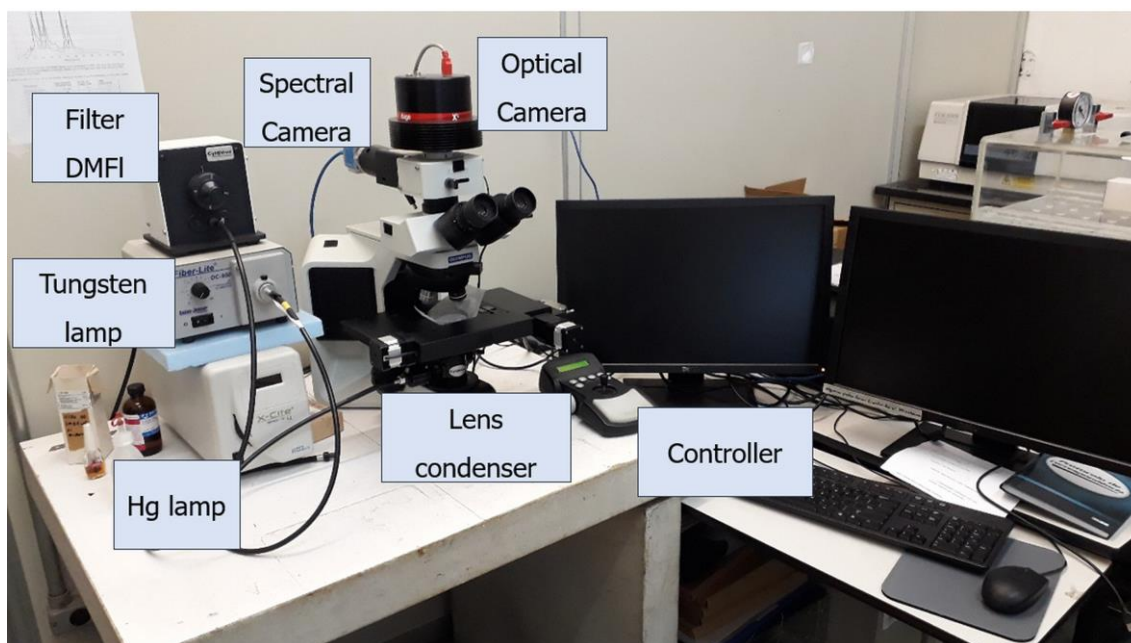In high definition mode it makes medium compositions every 4 pixels (binning)

Figure 1A. The CytoViva dark-field setup.

SAMPLE PREPARATION

Slide > swatch > Cover slip > masking tape > glaze

Special care must be taken with the blade to avoid scratches or dust.

Schott blade + Nexterion GlassB

Schott slides are used due to their purity, as they are made of crystal, have few bubbles and have metric (topological) regularity.

After covering the sample with a cover slip, they must be sealed with adhesive tape and nail polish, as the analyzes are carried out in oil immersion and the movement of the table can displace the cover.

For samples in solution (reaction solution, buffer in the case of proteins or cells or culture medium, 20μL of the solution should be used.

In the case of samples in solution, due to the depth, common glass slides can be used.

For cells, the slides can be left at the bottom of the culture medium container during the incubation step.

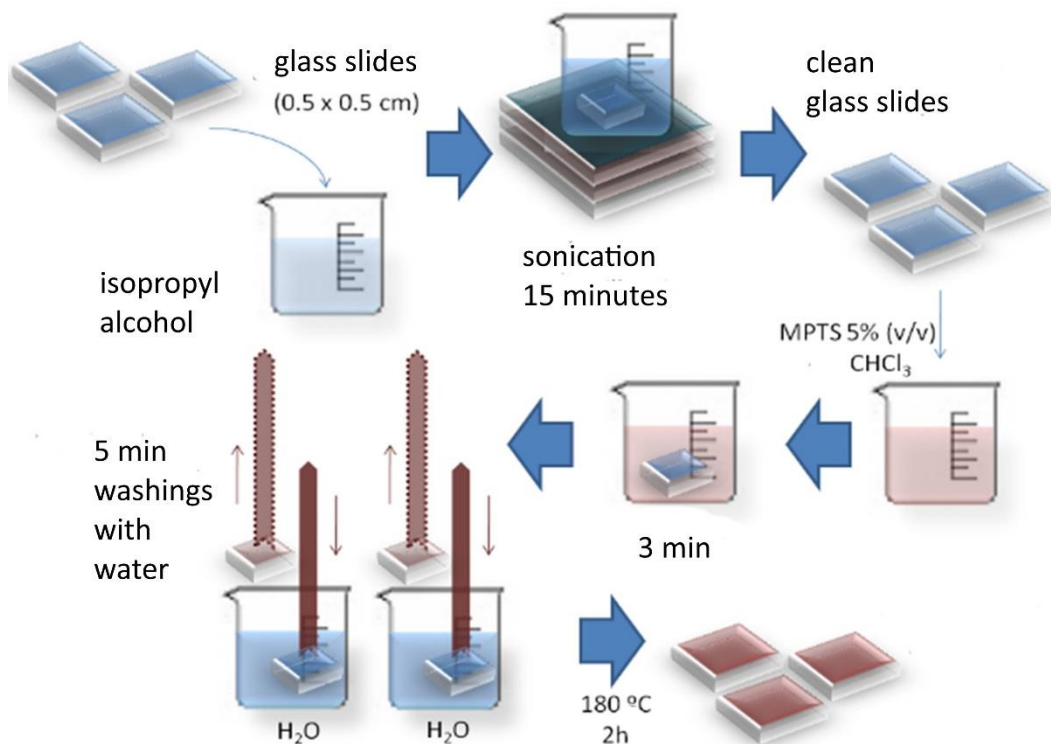Performing Blade functionalization (APTS/MPTS), Figure 2A.

Figure 2A. Blade functionalization scheme using   (APTS/MPTS)

Slides functionalized with APTS / MPTS were used for analysis of AuNP films.   The AuNP solution was applied on the slide, left for a while for film formation and then the solution was removed and covered with cover slip,   and sealing.

FUNCTIONALIZATION OF GLASS SLIDE WITH APTS / MPTS

The functionalization of Schott slides does not require a washing step with isopropyl alcohol. To remove APTS or MPTS from the vial, use the procedure for removing oxidizable compounds. Carry out the operation in the shortest time as possible.The dip flask can be a petri dish.
If necessary you can use the muffle, and clean with a N2 flow.   Store in the case, but always signaling the functionalized face.

OPERATIONAL SCRIPT FOR IMAGE ACQUISITION
Equipment table controller – normally always on.
Fiber-Lite DC950 lamp (Dolan-Jenner) = standard 400 – 1000 nm source - liquid guide,
X-Cite series 120Q (Lumen Dynamics) = mercury lamp + Cytoviva filter for dual fluorescence mode - liquid guide

Optical Camera (DageXL) – must plug in the DC power supply plug

Turn on the computer.

The lamps must be turned on at low power, and left on for 10 minutes before analysis, for stabilization.

SOFTWARES

The exponent [DageM TI XLM450] – Optical RGB Image serves for:

  Optical camera control

  Image/video capture

It has several camera control parameters (Color Saturation, Shutter, Gain, exposure time...). To start the image acquisition, the adjustments must be left in automatic. As soon as the image can be visualized on the screen, manual compensation adjustments can be made.

ENVI 4.8 - SPECTRAL CAMERA

➢ This version of the ENVI software is specially modified for use with Cytoviva. The original software is used for use with satellite imagery.

➢ ENVI is used to:

    ¬ Spectral image capture

    ¬ HDR lamp spectrum correction

    ¬ Changing spectral bands for image presentation

    ¬ Selection of spectra

OPERATIONAL SCRIPT FOR IMAGE ACQUISITION

Operation:

The microscope has two switches for directing the objective image (Figure 3A).

Use the first key to select between: Ocular,   Eyepiece + Camera, Camera.

For spectrum acquisition, leave the switch in the "camera" only position

The second key selects between Optical Camera and Spectral Camera

Initializing the spectral software:

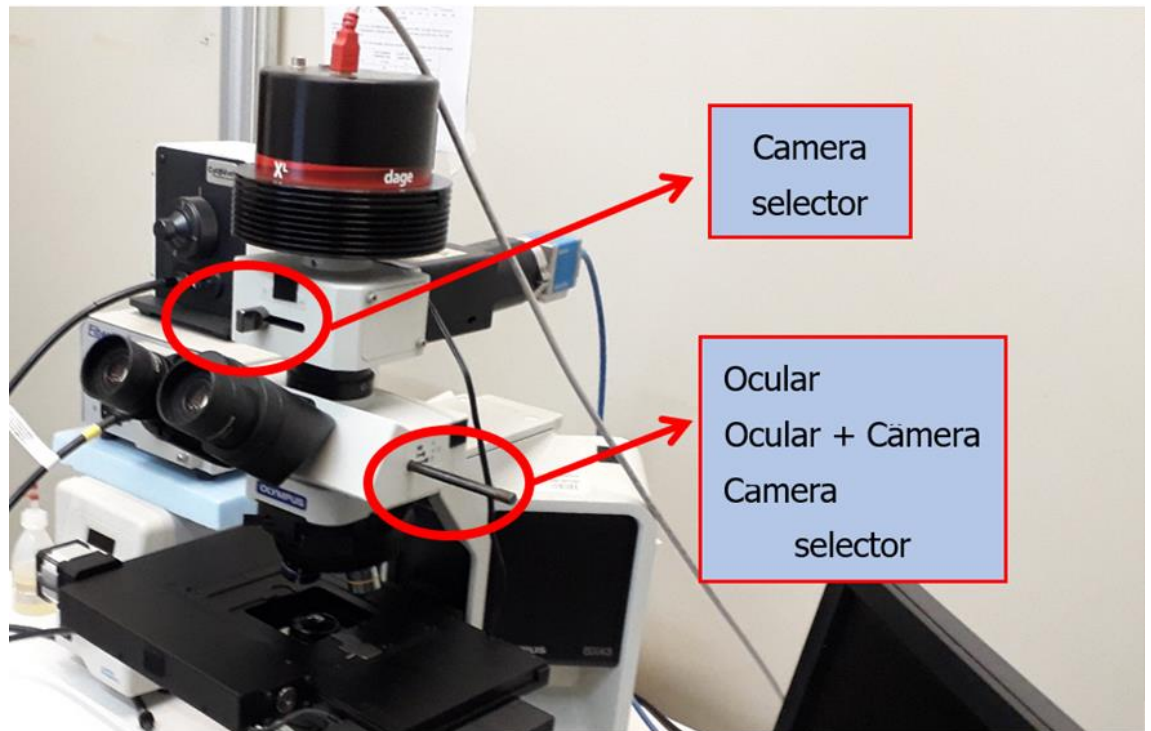ENVI > Cytoviva Menu > camera controls > COM3 port

Figure 3A. Keys for image acquisition.

FOCUS PROCEDURE AND OPTICAL IMAGE ACQUISITION

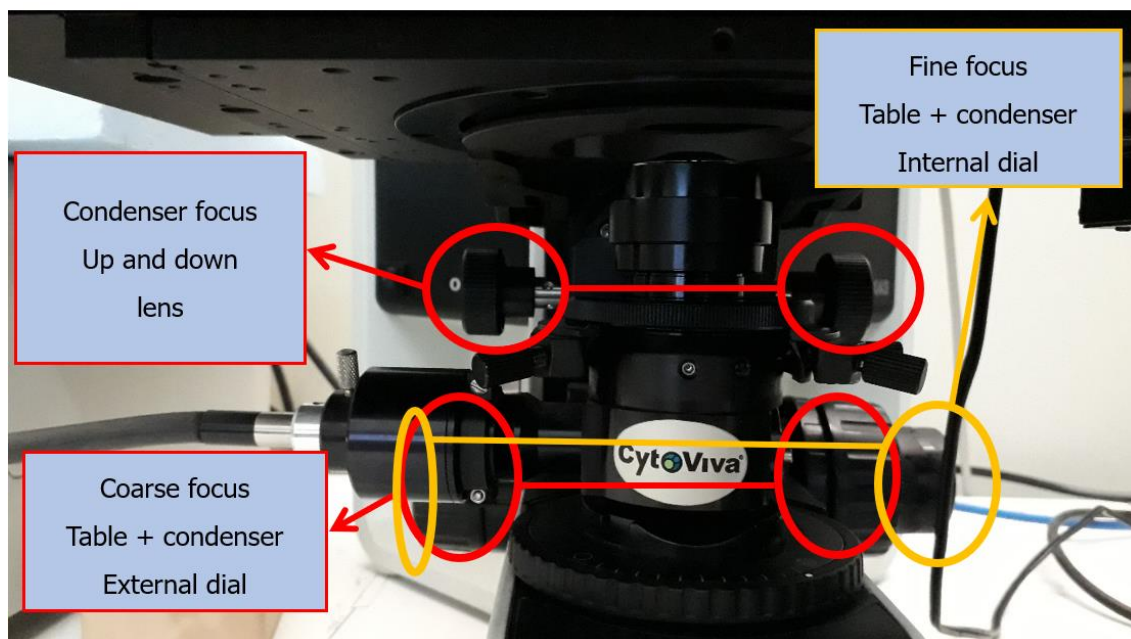In Figure 4A, it is shown three focus controllers:

Figure 4A. Three focus controllers: coarse, fine and condenser.

Procedure

1 - Lower the table + lens assembly (Coarse focus dial), lower the condenser lens ("Condenser focus dial) place 2 drops of microscopy oil on the condenser lens

2 - Place the slide in the sample holder

3 – With the "Condenser focus" dial, approach the condenser to the slide until it forms a spot (a small dot of light in the middle of the slide)

4 - Use the 10X AR objective lens to look for focus on the RGB camera, leaving the controls on automatic and raising the table assembly ("Coarse focus dial)

5 - Adjust the focus of the condenser lens to obtain the smallest circle of light on the camera (Fine Focus" dial)

6 - Repeat the steps to check the condenser adjustment using Fine Focus > Coarse Focus

7 - Place microscopy oil on top of the sample (1 drop)

8 – Place the objective lens selected for analysis by lifting the retractable tip of the lens before turning the microscope barrel. Drop the tip of the lens slowly over the sample. Analysis objective lenses: 100XOil or 60XOil

9 - Adjust Fine Focus:

Adjust focus for optical image through computer screen

Adjust the software parameters and acquire the image.

Focus procedure and spectral image acquisition

1 - Adjust focus for spectral image on the left eye eyepiece lens (it has a guide line drawn on the lens) [or on the oscilloscope after setting parameters]

2 - Adjust the parameters for spectra acquisition

>according to the used lens

> Set all parameters to "high"

> adjust the integration time of each spectrum (sample dependent)

> select "Flip X"

> Select number of lines Place odd number of lines

> Keep selected "Subtract dark" - "10 spectra"

> File name - it is important to always change the file name. The program corrupts the previous file and does not write the second one with the same name

> Click on "Collect hyperspectral..."

A new oscilloscope window will open, where you can check the focus and saturation of the signal.

The oscilloscope represents:

X axis - centerline coordinate

Y axis - wavelength

Z-axis - signal strength (indicated in white/black contrast) - is reflected on the y-axis as a graph in red

To adjust the focus, it is possible to visually make the intensity lines (Z axis) have the best definition

Optimum intensity is between 200 and 4000(CCD saturation) - can be increased by changing lamp power

Acquisition:

> click "Capture"

> Set the selection switch to "Ocular", click on OK

> Wait for the "dark current" measurement

> Put the selection key to "Camera" and click on No

> wait for spectra acquisition

Data analysis and processing

Subtract lamp spectrum:

ENVI > cytoviva analysis > lamp correction

select the current spectrum,

select the lamp spectrum "Lamp Spectrum correction.hdr" in the Lamp Spectrum folder on the desktop. The lamp spectrum must be recalibrated as per the procedure in the manual whenever the lamp is changed.

Assign a name to the new file. (usually "LC_name")

To view the scatter spectrum

Right-click on the image > Z profile

Opens the window with the spectrum of the selected pixel. You can browse the image. By changing the position of the spectral bands for the composition of the image on the screen (shifting the blue, green and red bars to the desired wavelengths) it is possible to change the composition of the RGB image with the first option "Load new RGB combination"

To export the spectra

Right click on the spectrum window > "Collect Spectra"

Click on the point on the image where you want the spectrum to be recorded. The pixel coordinate and the spectrum of the location are registered.

After selecting the points, in the spectrum window > File > Save Plot As > ASCII

In the new window select the desired spectrum or click on "Select All Items" and name the file

Data processing can be done in any software for tables
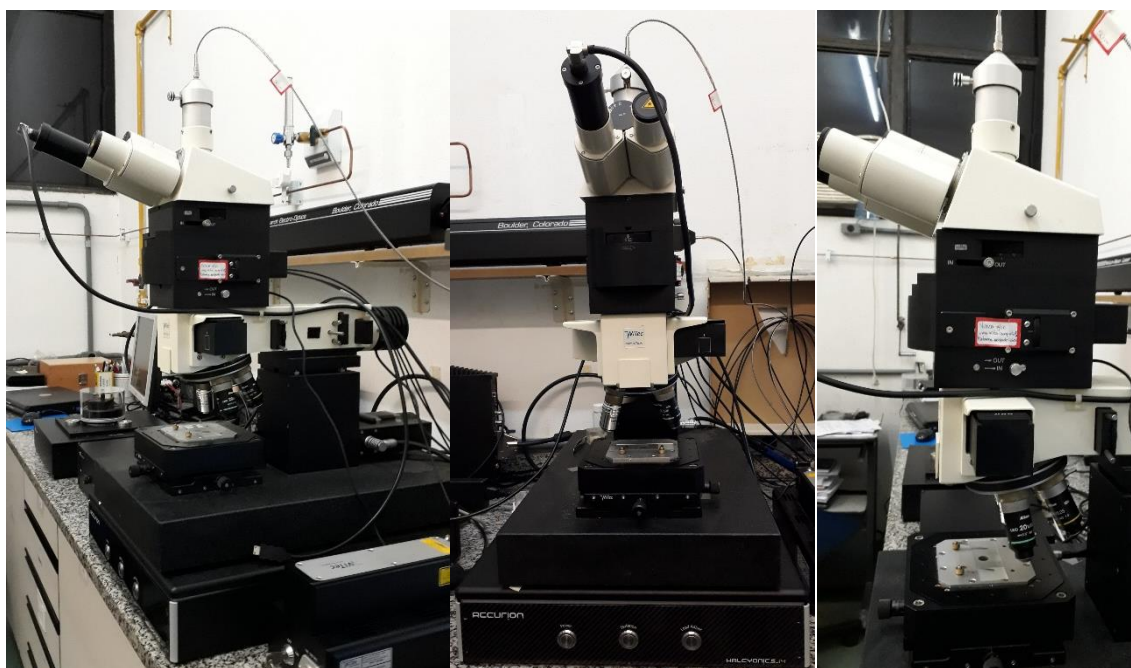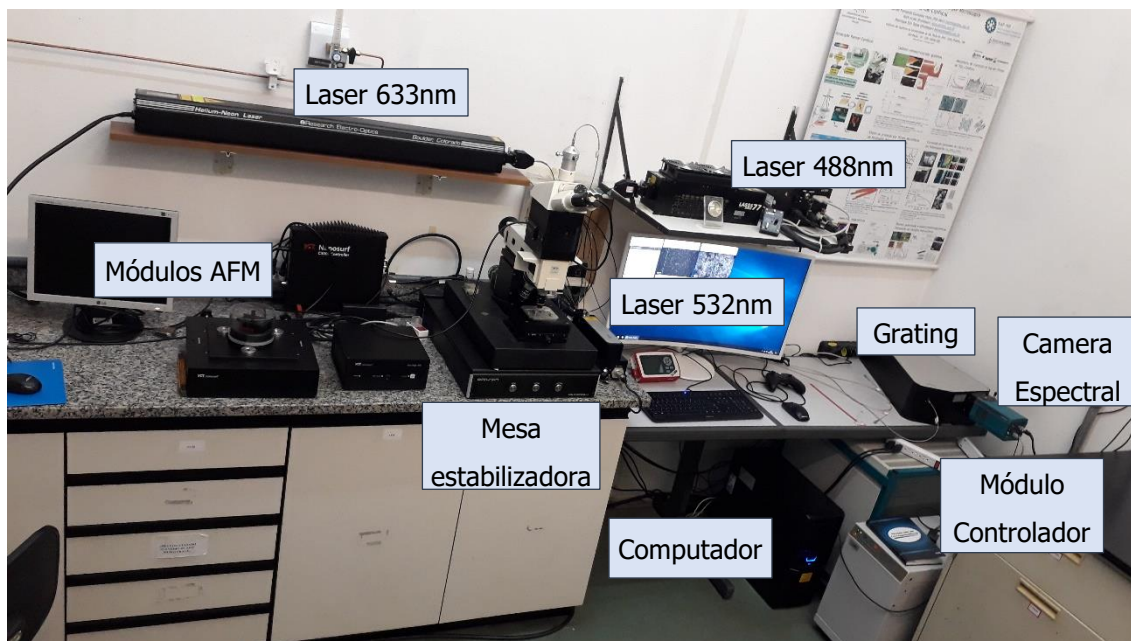
The instrument setup is shown in Figure 5A.

Figure 5A. The WITec alpha 300R Confocal Raman Microscope at different view angles.

Spectra Acquisition

Turn on the computer and monitors

Software: WiTec control.

When starting the software it regulates the sensor temperature to -60°C. From room temperature 25°C it takes around 20 min for stabilization.

Initial calibration

For every initialization or laser change:

Menu settings > laser / grating .

The choice of laser depends on the sample.

The 600 grid has less resolution but larger spectral window. The 1800 grid has a better spectral resolution but narrower spectral window.

Turn on lighting

Place the calibration sample, which can be Silicon, TiO_2, polymer or other.

Adjust focus. Adjust in Z, using the remote control (RC). After selecting Microscope Z, reset the actuation speed dial to 0. From there, increase the speed and then lower the microscope tower.

Adjust the spot diaphragm on the side. Close the spot and adjust the center with the 02 diagonal dials

Adjust the center of the spot with the laser and without a filter.

Check that the filter or window is the same as the wavelength of the laser being used.

Place a filter corresponding to the laser - hatched ball.

Adjust the 0 point on the Spectrograph tab. Use the Center Wavelength and Laser Wavelength parameters.

Adjust center of spectrographic window - Spectral Center.

Adjust the maximum intensity by aligning the collector fiber on top of the microscope.

Check the diameter of the fiber being used

Check the polarization dial

Placing the sample

Position the drum on the nozzle without lens

Place the sample.

Place on selected lens for analysis

Adjust lighting.

adjust focus

Adjust laser intensity

Use the real-time spectrum to check peak intensity, adjust acquisition time or laser power. If the bands decrease over time, the sample may be degrading / burning

Adjust the analysis parameters – integration time, number of acquisitions, image area, among any other.

Basic script for image treatment
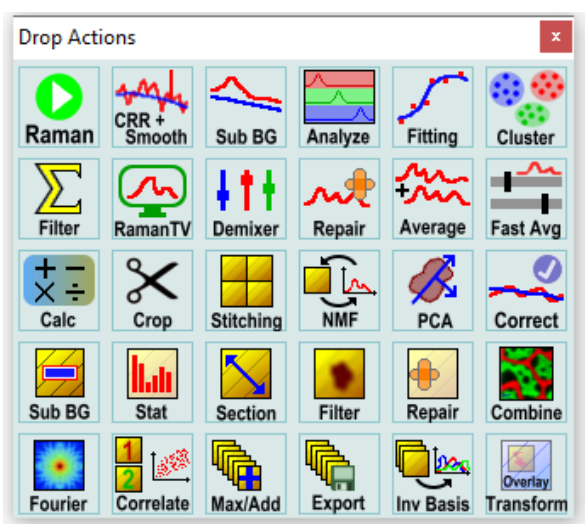Software: Project FIVE

Image treatment (Figure 6A)

Figure 6A   - Software: Project FIVE

1 - Menu Drop Actions
The functions for treating spectra are located in the "Drop Actions" area. To access the function, select the spectrum in the "Project Manager" window and drag it to the function button in the "Drop Actions" window. The buttons are enabled according to the information that exists in the file, that is, functions for 1 spectrum, for several spectrums, for image spectrums, for images and others.
According to the necessary information, the spectra must go through several processes in order to obtain the final information. Spectra can also be exported and processed in software such as Origin.
In all treatments, a preview window is displayed where the final spectrum or the final image can be visualized before being extracted.
After each spectrum treatment operation, click on "Extract" and a new file is generated at the end of the list, named with the applied treatment.

Basic functions for treating spectra
Remove CCR – removes fine peaks from Cosmic Rays. They appear more in long exposure spectra and with the EMCCD function activated.

Smooth – various algorithms and parameters for smoothing the local oscillation of the spectrum

Remove background – BG

It can be done through a constant spectrum (substrate) or programmed mask with the intervals between peaks selectable in "Advanced Mask Controls" or using the Shape filter in the Plus version. The "Shape Size" value of 150 proved to be ideal for several spectra.

Filter

It has mathematical operations that can be applied to simple spectra, giving a text file as answers, or to area spectra, resulting in a gradient image.

The gradient color pattern can be selected by clicking on the image with the right mouse button > Color Profile > Color Tables > select color grading. Grades with extreme color contrast are good for exploring differences in the image, but softer color grades are better for presentation.

The most used ones are:

Sum Filter – performs the integral of the selected area. For simple spectra they are important for quantitative measurements. For area spectra, they highlight where the peak has the greatest intensity.

For a spectrum exploration, just set a bandwidth around 30 and in the center of band box, use up or down arrow to vary by 10cm-1 and follow the variation in the preview window.

Filter: Maximum/Minimum > it is possible to obtain the value and position of the maximum and minimum values of the spectrum. With the maximum filter it is possible to perform the normalization operation in the calculator

Draw Field - Mask images

The "Draw Field" menu appears when clicking on images (area spectrum filters) and serves to draw a mask, used for processing data from a specific section.

After creating the mask, that is, selecting the desired area, just drag the mask with the spectrum set to the desired icon in dropactions and the treatment will only be for the mask area.

Combine - Used to combine images extracted from different filters (Figure 7A)

Add the filtered images in the "Combine" of DropActions

Increase the lower threshold to leave more low-intensity areas unstained.

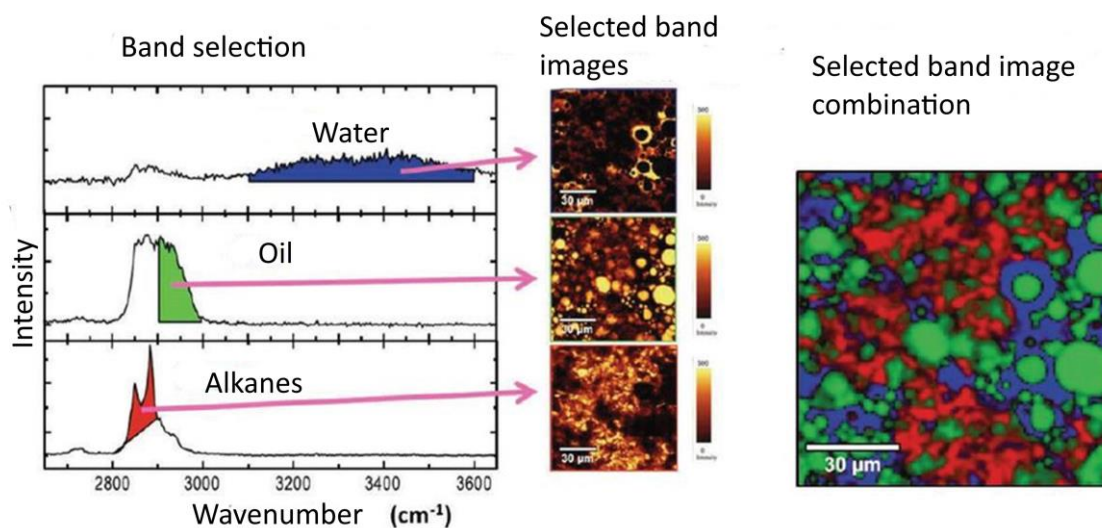Combine colors, explore transparency and smooth

Figure 7A. Band selection and the corresponding images or combination.

3 - Combination of images from filters by zone of interest

Advanced image functions such as "Analyze", "Cluster", "PCA" among others should be explored. These tools serve to detect different spectral patterns in an image. Further details of each function should be sought in the software's help menu.

(11) 94765-8974
E-mail jorge.shinohara@usp.br | jorgedasilvashinohara@gmail.com
Currículo Lattes: http://lattes.cnpq.br/8114304627430652
https://www.researchgate.net/profile/Jorge_Shinohara   CRQ-IV 04166363

FORMAÇÃO ACADÊMICA

- **Doutorado em Química (Doutorado Direto - Química Inorgânica, Espectroscopia, Nanotecnologia, SERS, Espectroeletroquímica, Analítica, Química de materiais**) - IQ-USP – instituto de Química, Universidade de São Paulo - início em 2016 - Orientador: Prof. Dr. Henrique Eisi Toma - término previsto 1° semestre/2023
- **Bacharel em Química Ambiental -** IQ-USP – instituto de Química, Universidade de São Paulo – 2007 - 2016
- **Ensino Médio** - Colégio Montessionense, sistema OBJETIVO -2001- 2003

EVENTOS / CONFERÊNCIAS / SIMPOSIOS

- Conferência USP de Nanotecnologia 2014-Workshop NAP-NN. 2014
- 38ª Reunião Anual da Sociedade Brasileira de Química. 2015
- 23º SIICUSP – Simpósio Internacional de Iniciação Científica USP. 2015
- 24º SIICUSP – Simpósio Internacional de Iniciação Científica USP. 2016 – Avaliador
- 4WHPC - USP / Rice – Workshop de Computação de Alta Performace – 2016
- Curso de Verão do Instituto de Física – IFUSP - 2017
- I Encontro Eletroquímica e Eletroanalítica IQ-USP – 2017
- 46th World Chemistry Congress, 40a Reunião Anual da Sociedade Brasileira de Química, e IUPAC 49th General Assembly – 2017
- 25º SIICUSP – Simpósio Internacional de Iniciação Científica USP. 2017 – Avaliador
- O porquê e como trabalhar uma publicação científica na atualidade, Henrique Eisi Toma, Out 2017 – 2h
- Simpósio em Homenagem ao Prof. Hans Stammreich, Jul 2019 – 8h
- Desenvolvimento de Métodos por LC-MS e Dicas para Validação – Webinar Shimadzu – abr/2021 - 1h30

CURSOS DE APERFEIÇOAMENTO

- Lean Six Sigma Yellow Belt – Academia de Belts– mai/2021 – 8h
- Lean Six Sigma White Belt – MF Treinamentos – abr/2021 – 4h
- Conceitos básicos de Logística e Supply Chain – Coursera / LALT-Unicamp – Jul/2020 – 40h
- Programa de aperfeiçoamento de ensino (PAE) – Estágio Supervisionado -2º sem 2016, 2017 – 360h
- Programa de aperfeiçoamento de ensino (PAE) – Preparação pedagógica -1º sem 2016 – 120h
- Treinamento nas bases Embase e Reaxys - Mar 2016 – 3h
- Theory and Practice of Raman Spectroscopy in Forensic Analysis - Dez 2016 – 6h
- VIBROS III - Curso de Espectroscopia Vibracional Prof. Oswaldo Sala - Jul 2015 – 32h
- IV Escola de Inverno de Radiofarmácia e Radioquímica - Jul 2014 – 40h
- Rappel Técnico - Jul 2011 – 8h

PUBLICAÇÕES: ARTIGOS E APRESENTAÇÃO DE TRABALHOS

Room temperature synthesis and Raman spectral evidence of carbon bond ranelate–gold nanoparticles, Júlio C. da Rocha; João V. Mattioni; Luca M. Sihn; Jorge S. Shinohara; Fernando M. Melo; Mauricio P. Franco; Ataualpa A.C. Braga; Henrique E. Toma
J Raman Spectrosc. 1– 9, 2020, https://doi.org/10.1002/jrs.5872

Raman studies of bis(phenylterpyrazine)iron(II) and supramolecular species with pentacyanidoferrate(II) ions, Ana Paula Mangoni, Bruno B. N. S. Brandão, Jorge da Silva Shinohara, Alceu Totti Silveira, Marcelo Nakamura, Henrique Eisi Toma,
Quím. Nova, (42), 9, 1020-1028, 2019 http://dx.doi.org/10.21577/0100-4042.20170415

Exploring the metallochromic behavior of pentacyanidoferrates in analytical spot tests, Jorge S Shinohara; Daniel Grasseschi; Sabrina N Almeida; Henrique E Toma
An. Acad. Bras. Ciênc., 2019, vol.91, no.2 DOI:10.1590/0001-3765201920180315 2019

Functionalized silica nanoparticles as adjuvant factor to increase the cytotoxicity of metallodrugs toward human tumor cells Eduardo Guimarães Vieira, Rodrigo Bernardi Miguel, Daniel Rodrigues da Silva, Rodrigo Boni Fazzi, Ricardo Alexandre Alves de Couto, Jayr Henrique Marin, Marcia Laudelina Arruda Temperini, Jorge da Silva Shinohara, Henrique Eisi Toma, Lilian Cristina Russo, Yuli Thamires Magalhães, Newton Luiz Dias Filho, Fábio Luiz Forti, Ana Maria da Costa Ferreira

New J. Chem., 2019,43, 386-398 DOI: 10.1039/C8NJ04654A 2019

Gold nanoparticle conjugation with microtubules for nanobiostructure formation. Daniel Oliveira, Jorge da Silva Shinohara, Henrique Eisi Toma
J. Bionanosci. 12, 271–277 (2018) DOI: 10.1166/jbns.2018.1521 2018

Thiosemicarbazone@Gold nanoparticle hybrid as selective SERS substrate for Hg2+ ions. Douglas Franciscato; Tiago Matias; Jorge Shinohara; Josué Gonçalves; Narcimario Coelho; Helena Nakatani; Koiti Araki; Henrique Toma; Vagner de Souza
Spectrochimica Acta Part A 204, 2018, 174-179– DOI: 10.1016/j.saa.2018.06.038 2018

Facile synthesis of labile gold nanodiscs by the Turkevich method. Daniel Grasseschi, Maria Luiza de Oliveira Pereira, Jorge da Silva Shinohara, Henrique Eisi Toma.
J Nanopart Res (2018) 20: 35. DOI: 10.1007/s11051-018-4149-y 2018

Caloric Restriction Promotes Structural and Metabolic Changes in the Skin; Maria Fernanda Forni; Julia Peloggia; Tárcio Teodoro Braga; Jesús Eduardo Ortega Chinchilla; Jorge Shinohara; Carlos Arturo Navas Iannini; Niels Olsen Saraiva Camara; Alicia J. Kowaltowski
Cell Reports 2017 Sep 12;20(11):2678-2692. DOI: 10.1016/j.celrep.2017.08.052. 2017

Confocal Raman microscopy and hyperspectral dark field microscopy imaging of chemical and biological systems, Henrique E. Toma; Jorge da Silva Shinohara and Daniel Grasseschi; *Proc. SPIE 9337, Nanoscale Imaging, Sensing, and Actuation for Biomedical Applications XII, 933702 (March 11, 2015);*
Conferência no SPIE BiOS, 2015, San Francisco, 07/fev/2015 2015 doi:10.1117/12.2087618

Posters

The colors of pentacyanidoiron pigments; Jorge da Silva Shinohara, Daniel Grasseschi, Sabrina Nobrega de Almeida, Henrique Eisi Toma
Pôster apresentado na 46th World Chemistry Congress, 40a Reunião Anual da Sociedade Brasileira de Química e IUPAC 49th General Assembly 2017

A new synthesis of gold nanoparticles by tetravalente anion ranelate under mild conditions; Julio Cesar da Rocha, Fernando Menegatti de Melo, Jorge da Silva Shinohara, Henrique Eisi Toma
Pôster apresentado Por Julio Cesar da Rocha na 46th World Chemistry Congress, 40a Reunião Anual da Sociedade Brasileira de Química eIUPAC 49th General Assembly 2017

Real time analyysis of anisotropic AuNps synthesis by Turkevich methods; Maria Luiza de Oliveira Pereira, Daniel Grasseschi, Jorge da Silva Shinohara, Henrique E. Toma
Pôster apresentado por Maria Luiza de Oliveira Pereira na XV Brazilian MRS Meeting, Campinas / SBPMat, 2016

Análise de Filmes de Nanopartículas de Ouro por Microscopia Hiperepectral de Campo Escuro; Jorge da Silva Shinohara(IC), Daniel Grasseschi(PG), Henrique E. Toma(PQ)
Pôster apresentado na 38ª Reunião Anual da Sociedade Brasileira de Química 2015

Revisando os Testes de Feigl para Detecção de Metais por Espectroscopia Raman Intensificada por Superfície (SERS); Jorge da Silva Shinohara(IC), Daniel Grasseschi(PG), Henrique E. Toma(PQ)
Pôster apresentado no 23º SIICUSP – Simpósio Internacional de Iniciação Científica da USP 2015